

Deployable Space Telescope

Redesign of the Secondary
Mirror Support Structure
I. Akkerhuis



Deployable Space Telescope

Redesign of the Secondary Mirror Support Structure

by

I. Akkerhuis

to obtain the degree of Master of Science in Aerospace Engineering
at the Delft University of Technology.

Student number: 4271750
Project duration: January 27th, 2020 - Wednesday 23rd September, 2020

Thesis committee:
Chair: Prof. dr. E.K.A. Gill
Thesis supervisor: Ir. J. Bouwmeester
Internal: Dr. ir. J.M. Kuiper
External: Dr. S.J. de Vet

Cover background photo credit: NASA JPL (https://www.jpl.nasa.gov/social/tw_earth.php#)

Summary

Satellite Earth observation has become more important than ever, and the need for high-resolution imagery with a high revisit time is ever increasing. Currently, large monolithic telescopes, like the WorldView-4, set the bar at a ground sampling distance of 31 cm. These are, however, very expensive, making it hard to provide both high-resolution images and high revisit time. One of the limiting factors in telescope design is the distance between the primary and secondary mirror, which defines the maximum achievable resolution. This distance needs to be large to achieve a high-resolution, meaning conventional monolithic telescopes are big and bulky. The Deployable Telescope Satellite (DST) project proposes to cut the mass, launch volume, and thereby the manufacturing and launch costs of high-resolution space telescopes by making the primary and secondary mirror of the telescope deployable. Decreasing the cost of such telescopes enables them to be used in satellite constellations, which ensures that high revisit times are achieved.

The DST is a project in progress at the department of space engineering of the Aerospace faculty of the Delft University of Technology. The design of the deployable part of the DST consists of four deployable primary mirror segments, a deployable baffle and a deployable secondary mirror, which were designed in previous work.[1–4] The Secondary Mirror Support Structure (SMSS) consists of four deployment legs, which are attached at their root to the instrument housing and connected at the top by the spider, on which the secondary mirror is mounted. However, using such a deployable structure poses significant technical issues. One of these issues is the variation in distance between the primary and secondary mirrors due to thermoelastic effects in the deployment booms. This translation is minimised because the baffle keeps the temperature of the SMSS relatively stable. However, the translation is still too high to produce high-quality images. This thesis is focussed on identifying the exact displacement of the secondary mirrors, within the bounds of the previous designs, and finding a solution to keep this displacement within the specified budgets.

The temperature variations of each component of the telescope were determined by simulations using an ESATAN TMS model. The temperature results of these simulations were used to determine the thermoelastic expansion of each component of the SMSS. These add up to a total in-orbit displacement of about $80 \mu\text{m}$. With a maximum in-orbit drift of $2 \mu\text{m}$, this translation needs to be decreased considerably.

Several different concepts to keep this translation within the specified budgets were considered, ranging from passive system athermalisation, active thermal control and finally mechanical actuation of the secondary mirror. The latter was selected and was designed in detail. This resulted in a three-part design. Firstly, the secondary mirror is mounted on the spider through bonding, because this provides the most simple and light-weight solution while keeping the stresses in the mirror at a minimum. Secondly, the translation of the secondary mirror is kept at a minimum utilising four linear piezo actuators, each placed in one of the deployment legs. These actuators were chosen because of their high accuracy, reliability, space heritage and low mass. Thirdly, the displacement of the secondary mirror is measured using four displacement measuring interferometers (DMIs). DMIs were chosen because they allow for a simple, low-mass system which provides a high accuracy. This combination of actuators and DMIs actively keeps the displacement of the secondary mirror as close to zero as possible.

This system reaches an accuracy of $0.58 \mu\text{m}$, high enough to keep the in-orbit drift of the secondary mirror below $2 \mu\text{m}$. The total SMSS mass is 9.53 kg, below the requirement of 14 kg. This means that the designed system achieves its main functionality while meeting the mass budget. There are, however, some doubts about the feasibility of using DMIs to measure the displacement in space. Such systems are proven to work on Earth and are planned for use on a larger scale on missions like the Laser Interferometer Space Antenna (LISA), but as of now, there are no DMI systems with the exact functionality as required for the SMSS. Additional research and design work is thus required to prove that DMIs can reliably be used in space applications such as the DST.

Preface

It is with great pleasure that I type these last sentences of my thesis. Even though the Deployable Space Telescope is a great project and I enjoyed the work that I did, I must say the past few months were rough. I had to work from my cosy unventilated attic room through the searing heat of some of the most intense heat waves this country has ever seen and got to know every square inch of my house better than I ever did.

However, it has paid off. I can wholeheartedly say that I am proud of the work that follows this page. I want to thank my supervisor Jasper Bouwmeester for the insightful support he has given me throughout this thesis, and my friends and family for their emotional support.

I hope you enjoy reading this thesis.

*I. Akkerhuis
Delft, Wednesday 23rd September, 2020*

Contents

Summary	iii
Preface	v
List of Figures	xi
List of Tables	xv
List of Symbols	xvii
Nomenclature	xix
1 Introduction	1
2 Deployable Space Telescope	3
2.1 The Earth observation market	3
2.1.1 Earth observation	3
2.1.2 Telescope resolution	4
2.2 The Deployable Space Telescope	5
2.2.1 The project	6
2.2.2 Mission requirements.	6
2.2.3 System budgets	7
2.3 Deployable Space Telescope concept.	7
2.4 Deployable Space Telescope architecture	9
2.4.1 Instrument housing	11
2.4.2 Primary mirror & support structure.	11
2.4.3 Secondary mirror & support structure	12
2.4.4 Deployable baffle	14
2.5 Thesis	15
2.5.1 The problem	15
2.5.2 The Research.	20
2.5.3 Methodology	20
3 Design Review	23
3.1 Functionality & Requirements	23
3.1.1 Functionality	23
3.1.2 Requirements.	24
3.2 System level design	24
3.2.1 Mass & Volume	24
3.2.2 Secondary mirror drift	25
3.3 Verifying the thermal model	26
3.3.1 Rationale check.	26
3.3.2 ESATAN model	27
4 Thermal model	29
4.1 Thermal background	29
4.1.1 Conduction	29
4.1.2 Doenecke method	30

4.2	Problem solving	31
4.2.1	Mirrors	31
4.2.2	Primary mirror support structure and spider	32
4.2.3	Conduction between parts	32
4.2.4	baffle	35
4.2.5	Primary mirror shape	36
4.2.6	Value errors	36
4.2.7	Earth Albedo and temperature	36
4.3	Verifying the model	36
4.3.1	Analytic relations	36
4.3.2	Sensitivity checks	39
4.4	Results	43
5	Concept generation	45
5.1	Identification and selection of design concepts	45
5.1.1	Athermalisation	46
5.1.2	Thermal control	47
5.1.3	Active mechanical control	49
5.1.4	Concept conclusion	49
5.2	Preliminary design and analysis of selected concepts	50
5.2.1	Athermalisation	50
5.2.2	Thermo-mechanical actuation of the rods	52
5.2.3	Heating of booms	55
5.2.4	Quasi-active thermal control of rods	57
5.2.5	Actuation of secondary mirror	58
5.2.6	Actuation of spider	59
5.2.7	Concept conclusion	60
5.3	Trade-off	60
5.3.1	Graphical trade-off	61
5.3.2	Numerical trade-off	63
6	Detailed design	65
6.1	Actuation	65
6.1.1	Actuator types	66
6.1.2	Actuator trade-off	70
6.2	Measuring the secondary mirror translation	72
6.2.1	Sensing concepts	72
6.2.2	Displacement measurement trade-off	81
6.3	Secondary mirror mount	82
6.3.1	Mounting concepts	83
6.3.2	Trade-off	90
7	Verification	91
7.1	Component verification	91
7.2	System verification and validation	93
7.2.1	Verification of the translation and rotation budgets	93
7.2.2	Structure mechanical verification	95
7.2.3	System validation	95
7.2.4	Sensitivity analysis	96
8	Results & Conclusion	97
8.1	Main design	97
8.1.1	Secondary mirror actuation	98
8.1.2	Displacement measurement	98
8.1.3	Secondary mirror mount	98

8.2	Rationale behind design	98
8.2.1	What requirements should the SMSS adhere to?	99
8.2.2	What concept should the design of the SMSS be based on?	99
8.2.3	Can the design of the SMSS feasibly be implemented within the DST ?	100
8.3	Main conclusions	100
9	Recommendations	103
A	DST mission & Secondary Mirror Support Structure requirements	105
B	ESATAN inputs	111
	Bibliography	115

List of Figures

2.1	Earth Observation market sales	4
2.2	Deployable Space Telescope project structure as of March 2020.	6
2.3	Optical layout of the Deployable Space Telescope	9
2.4	Schematic of the Deployable Space Telescope	10
2.5	Coordinate system of the Deployable Space Telescope.	10
2.6	Stored and deployed configuration of the primary mirror and its support structure	11
2.7	Primary mirror deployment mechanism in stowed position and deployed position	12
2.8	Primary mirror support frame	12
2.9	Design overview of the telescope	13
2.10	Working principle of tape spring	13
2.11	The CORE hinge	13
2.12	The spider	14
2.13	The secondary mirror interface	14
2.14	Baffle in deployed configuration	14
2.15	Baffle deployment system in deployed and stowed position	15
2.16	Translation and rotation of secondary mirror	16
2.17	Schematic overview of the relevant lengths of the secondary mirror deployment system.	17
2.18	Relevant lengths of the root and top CORE hinges	17
2.19	Schematic overview of the longitudinal translation of the secondary mirror due to extension of the interface rods and spider	18
2.20	Schematic overview of the expansion of the mirror and its radius of curvature.	19
2.21	V-model systems engineering approach as used for the thesis.	21
3.1	Schematic overview of two stowed configurations of the DST	26
4.1	Contact conductance across a mounting interface with and without RTV filler.	30
4.2	Lightweighted mirror segment.	31
4.3	Endcap of the deployable booms.	33
4.4	Top CORE hinge.	33
4.5	Attachment of root CORE hinge to instrument housing.	35
4.6	Visual inspection of the model as performed within ESATAN.	37
4.7	Analytic and simulation temperature results	38
4.8	Temperature profile of the rods modelled as thin walls versus solids.	39
4.9	Average temperature sensitivity to a change of Month	40
4.10	Average temperature range sensitivity to a change of Month	40
4.11	Temperature sensitivity to a change in conductance between the in- and outside of the baffle	41
4.12	Temperature sensitivity to a change in conductance between the in- and outside of the baffle	41
4.13	Temperature sensitivity to a change in conduction through the different CFRP components	42
4.14	Temperature sensitivity to a change in conduction through the CORE hinges	42
4.15	Temperature sensitivity to a change in conduction through the connection from the spider to the rod	43
4.16	Temperature sensitivity to a change in conduction through the connection from the rods to the secondary mirror	43
4.17	Different temperature profiles for the best to worst case scenarios	44
5.1	Design option tree of secondary mirror support structure.	46
5.2	Hexapod mount used on the Subaru telescope.	49

5.3	Eccentric drive.	49
5.4	Design option tree of secondary mirror support structure with three concepts eliminated.	50
5.5	Mismatch between the temperature profile of the booms and rods.	52
5.6	Temperature profile and net heat balance of the rods with and without applied heat	53
5.7	Temperature response of the rods to different levels of applied heat	54
5.8	Polynomial fit of temperature range of the rods versus applied heat	54
5.9	Polynomial fit of the temperature range of the booms and root and top CORE hinges.	54
5.10	Cabling mass versus current through the cable.	55
5.11	Added mass of the SMSS as a function of heating power.	56
5.12	Temperature profile and net heat balance of the booms with and without applied heat	56
5.13	Temperature response of the booms to different levels of applied heat.	57
5.14	Polynomial fit of the temperature range of the booms as a function of the applied heat.	57
5.15	Temperature profile, net heat balance and impingent Albedo radiation of the rods.	58
5.16	Temperature profile of the rods with and without adaptive coating.	58
5.17	Longitudinal translation of the secondary mirror.	58
5.18	Design option tree of secondary mirror support structure with remaining and infeasible options.	60
5.19	Graphical trade-off table for deciding the best concept to stabilise the secondary mirror.	62
6.1	Actuator Design Option Tree.	66
6.2	Linear stepper assembly with 25:1 gearing.	67
6.3	Piezo hexapod controller. Retrieved from Defendini et al. (2000).	69
6.4	Step response of a piezo actuator with and without optimised PID closed loop.	70
6.5	Example of a walking drive inchworm style piezoelectric actuator.	70
6.6	Actuator trade-off.	71
6.7	Design Option Tree for finding the best concept to measure the secondary mirror translation.	73
6.8	Thermal recycling hysteresis curve of carbon fibre reinforced composite.	74
6.9	Vertical temperature distribution of one of the nodes of the boom.	74
6.10	Temperature distribution around the circumference of a boom.	75
6.11	Temperature measurement error due to discrete amount of nodes.	75
6.12	Differential expansion of the booms.	76
6.13	Configurations for strain gauge distribution in the CORE hinges.	76
6.14	Overview of Fibre Bragg Gratings	78
6.15	Displacement measuring interferometer	80
6.16	Accuracy of the IDS	81
6.17	Graphical trade-off table for deciding the translation measurement concept.	82
6.18	Two different types of hard mounts.	83
6.19	Clip mount.	84
6.20	Elastomer mount.	84
6.21	Bonding surfaces for mounting mirrors.	85
6.22	Kinematic mount.	86
6.23	Three different flexure mounts.	87
6.24	Flexure material profiles	88
6.25	Schematic of a flexure blade.	89
6.26	Conceptual design of the secondary mirror flexure mount.	90
7.1	Temperature design margins	92
7.2	Simplified version of DST in stowed configuration	92
7.3	Hottest and coldest temperature profiles during LEOP of the piezo actuators and the IDS laser heads	93
7.4	Verified longitudinal translation of each deployment leg.	94
7.5	Verified thickness variation of secondary mirror.	95
7.6	Rotation of secondary mirror caused by differences in temperature between deployment legs.	95
8.1	Design render of the secondary mirror support structure.	97

8.2	The APA100M amplified piezo actuator	98
8.3	Design render of the spider.	99

List of Tables

2.1	Characterisation of EO satellites	4
2.2	DST objectives	7
2.3	DST requirements	8
2.4	Mechanical mirror alignment budgets	9
2.5	DST research question.	21
3.1	New DST mission requirements.	24
3.2	New SMSS requirements.	24
3.3	Preliminary mass budget of the Deployable Space Telescope.	25
3.4	Nominal temperature budget of the Deployable Space Telescope	26
4.1	Density and effective density of primary and secondary mirror.	32
4.2	Earth perceived Albedo and temperature by latitude.	37
4.3	Temperatures of the booms, rods and CORE hinges.	44
5.1	Parameters of three different actuators.	59
5.2	Parameters of four different actuators.	59
5.3	Trade-off weights for deciding the best concept to stabilise the secondary mirror.	61
5.4	Numerical trade-off of three concepts.	63
6.1	Data of the P-841.6 and APA100M linear piezoelectric actuators.	68
6.2	Actuator comparison.	71
6.3	Quantitative mass scoring scheme.	72
6.4	Quantitative power scoring scheme.	72
8.1	DST research questions.	99
A.1	DST requirements	106
A.2	SMSS requirements	107
A.3	Compliance to requirements.	109
B.1	Input for ESATAN-TMS.	112
B.2	Conduction between different components as used in the ESATAN TMS models.	113

List of Symbols

A_{min}	Minimum bonding area [m^2]
G	Adhesive shear shear/ tensile strength [N/m^2]
a_G	Worst-case acceleration factor [-]
f_S	Safety factor [-]
A	Area [m^2]
C_{ij}	Conductive coupling between i and j [W/K]
C	Capacitance [F]
F_d	focal length [m]
F	Force [N]
H	Altitude [km]
I	Current [A]
L	Length [m]
P	Power [W]
Q_{ij}	Heat flow from i to j [W]
R_C	Radius of curvature [m]
U	Voltage [V]
Δt_{drift}	Drift Time [s]
Δt_{stable}	Stability Time [s]
α	Coefficient of thermal expansion [$\mu m/mK$]
ϵ_{eff}	Effective emittance [-]
γ	rotation [rad]
λ	Wavelength [m]
ρ	Density [kg/m^3]
σ	Stephan-Boltzmann constant [$Wm^{-2}K^{-4}$]
θ	Angular resolution [rad]
a	Acceleration [m/s^2]
c_p	heat capacity [J/kgK]
d	Diameter [m]
h_c	Conductance [W/m^2K]
k	Conductivity [W/mK]
m	Mass [kg]
t_{SM}	Thickness of the secondary mirror [m]
F#	F-number [-]

Nomenclature

ACS Aberration Correction System
AFTMA Annular-Field Four Mirror Anastigmat
AHP Analytical Hierarchy Process
BOL Beginning-of-Life
CFRP Carbon Fibre Reinforced Polymer
CORE Compliant Rolling Element
COTS Commercial off-the-shelf
CR Consistency ratio
CTE Coefficient of Thermal Expansion
DC Direct Current
DM Deformable Mirror
DMI Displacement Measuring Interferometer
DOF Degree of Freedom
DOT Design Option Tree
DST Deployable Space Telescope
EO Earth Observation
ESCC European Space Components Coordination
FBG Fibre Bragg Grating
FM Fold Mirror
FOV Field of View
GSD Ground Sampling Distance
HDRM Hold-Down & Release Mechanism
HR High Resolution
IC Integrated Circuit
IDS Industrial Displacement Sensor
IR Infra-Red
LEOP Launch and Early Operations
LISA Laser Interferometer Space Antenna
LR Low Resolution
MLI Multi Layer Insulation

MR Medium Resolution

MTF Modulation Transfer Function

PM Primary Mirror

PMAO Primary Mirror Active Optics

PMD Primary Mirror Deployment

PMSS Primary Mirror Support Structure

RMSE Root-Mean-Square Error

RTV Room-Temperature-Vulcanized

SiC Silicon Carbide

SM Secondary Mirror

SMDM Secondary Mirror Deployment Mechanism

SMSS Secondary Mirror Support Structure

SNR Signal-to-Noise

TBD To Be Determined

TDI Time Delay and Integration

TIR Thermal Infra-Red

TM Tertiary Mirror

TRL Techonology Readiness Level

VHR Very High Resolution

1

Introduction

Satellite Earth observation has become more important than ever. Governments and companies require more and more high-resolution Earth images, for instance, to fight climate change, track forest fires and monitor crop fields, meaning that the need for imagery with a high revisit time is ever increasing. Currently, the best available images are produced by large spacecraft, such as the WorldView-4, with a Ground Sampling Distance (GSD) of 31 cm.[5] The revisit time is primarily determined by the altitude of the telescope, which is bound to physical limits. Therefore, to achieve high-resolution imagery with a high revisit time, a constellation of multiple telescopes is best used. With an approximate cost of \$835 million[6] for telescopes such as the WorldView-4, the cost associated with launching multiple of such telescopes is very high. Conventional telescopes make use of a monolithic primary mirror and a rigid Secondary Mirror Support Structure (SMSS). To decrease the mass and volume, and thereby the cost of high-resolution space telescopes, the DST proposes the design of a deployable telescope. By doing so, a large distance between the primary and secondary mirror, which enables high-resolution images, is maintained while keeping the stowed volume and mass low.

The DST is a project in progress at the department of space engineering of the aerospace faculty at the Delft University of Technology. The design of the deployable part of the telescope consists of four deployable primary mirror segments, a deployable baffle and a deployable SMSS. Using such deployable structures, however, poses significant technical issues. One of these issues is the variation in distance between the primary and secondary mirror. This distance changes due to thermoelastic expansion and contraction of the SMSS under the influence of temperature changes. This thesis is focussed on identifying the exact displacement of the secondary mirror due to thermoelastic effects and then finding a solution to keep this displacement within the specified budgets. It continues the work of A. Krikken, who designed the SMSS, and J. W. Arink, who designed the baffle to stabilise the temperature of the DST.

This thesis is logically structured according to the main design steps. Firstly, chapter 2 delves deeper into the project itself. It provides a more in-depth insight into why the DST is developed, followed by a discussion on what is required of the telescope. It discusses the working principles of the DST and presents the current (as of April 2020) design. Chapter 2 is concluded by a discussion on the thesis need, goal and research questions. The main goal of this thesis is to find the best design that ensures that all translational and rotational budgets of the secondary mirror are met.

In chapter 3, a review of the current DST design and the design choices made to come to this design are presented. Firstly, the main functionalities and requirements are reviewed and updated. This is followed by a discussion on the multiple design concepts proposed, and some flaws and design challenges are identified.

One of the issues identified in chapter 3 are flaws in the thermal ESATAN TMS model previously used. In chapter 4, these issues are resolved. The temperature results gained from the improved thermal model are presented.

With the newly acquired temperature information, the full range of translation of the secondary mirror is calculated. This range provides the primary input on which the different concepts to stabilise the secondary mirror are based. In chapter 5, the different concepts to stabilise the secondary mirror are expanded and evaluated. The concept that provides mechanical actuation for the entire spider is selected by means of a trade-off .

The selected concept is designed in detail in chapter 6. The three parts of the concept are individually designed, each part consisting of a procedure to identify and design the viable sub-concepts and finally a trade-off to select the best sub-concept.

The result of chapter 6 is a detailed design in which the displacement of the secondary mirror is measured using Displacement Measuring Interferometers (DMIs) and actuated to counter this displacement by means of linear piezo actuators. This design is verified and validated in chapter 7. The verification methodology, as presented in figure 2.21, is followed to ensure that all requirements are met.

The main research question, namely what the design should look like, is answered in chapter 8. The main system parameters are provided along with visualisations of the design. This is followed by a discussion on the performance of the design and conclusions regarding the design are drawn. Finally, recommendations regarding future work are presented in chapter 9.

2

Deployable Space Telescope

This chapter provides an insight into why the Deployable Space Telescope is developed. Firstly, in section 2.1 the Earth Observation (EO) market is discussed, along with what current EO satellites are and future EO satellites should be capable of. Next, the case for the DST is presented in section 2.2. The way by which the project is structured, and what is required from the telescope is presented.

2.1. The Earth observation market

In this section the satellite Earth Observation market is discussed. Firstly, what this market entails and why it is needed is explained. This is followed by an analysis of the market and its actors. Finally, a brief discussion on what EO telescopes should be capable of in the future is presented.

2.1.1. Earth observation

Earth observation is the act of gathering information about the Earth's surface. Remote sensing is part of this. It entails gaining information from a distance. In this report, Earth observation is considered to be the same as remote sensing from space, which is usually done by making use of telescopes placed in an orbit around Earth. This report considers EO in the visible spectrum, which is used to monitor and track changes of Earth's environments, be it natural or human-made.

So, why is EO necessary? In general, EO can be grouped in different categories, being the protection of Earth and humanity, resource management and governmental purposes.

The first incentive is arguably the most important one, although it does not provide short term profit. It can again be split up in two parts, namely immediate and long-term protection. By tracking for instant forest fires, volcano activity and seawater levels, governmental bodies can act accordingly and save human lives from impending disaster. Long-term protection is focused on environmental protection. By monitoring the environment and changes therein, the scope of climate change becomes more apparent and better predictions can be made. These predictions are vital to minimise climate change. Examples are the monitoring of pollution, ice caps and glaciers and deforestation.

Secondly, resource management is considered. Companies and governments alike can profit from knowledge about their assets. With this information, they can optimise their procedures to cut costs and thus increase their profit margin. Such practices are, among other things used in the agricultural and mining sectors.

Governments and their militaries have an interest in knowing what other countries are doing at all times. This desired knowledge mainly consists of following military activities and troop movements but also on monitoring suspicious activities, such as the development of nuclear facilities. Nowadays, governments are also interested in EO to enforce the law. Monitoring offences and criminal activities can be discerned, but for instance, also tracking the pollution of individual companies to make sure they abide by the law.

Concluding, there are many incentives to make use of Earth observation. These incentives provide a significant potential customer base for information gained from EO satellites. In the period between

2005 and 2014, the market showed significant growth. The projected market sales of the Earth observation market can be seen in figure 2.1. Even though this report is slightly outdated, the trend of market growth is evident. This projected growth is supported by other market prospect analyses which predict the market value to increase ranging from around 13% to 20% in the coming five years[7, 8]. Furthermore, Euroconsult (2018) estimates roughly 1500 new EO satellites are required in the coming five years. There is thus an obvious need for more EO satellites, and customers are willing to pay for it. This provides sufficient confidence to advance the design of the DST.

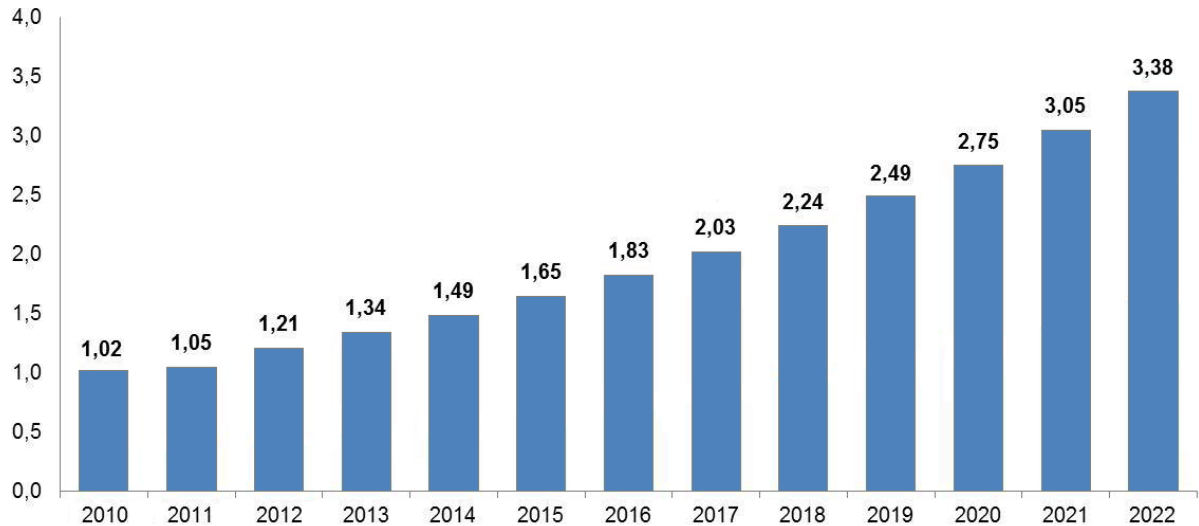


Figure 2.1: Earth Observation market sales in €Billion (2010-2022). Retrieved from SpaceTec Partners (2013).

2.1.2. Telescope resolution

Of course, no single satellite can serve all the purposes as previously described. Different telescopes are used to serve different purposes. Telescopes can roughly be characterised upon their spatial, temporal and spectral resolutions in the Very High Resolution (VHR), High Resolution (HR), Medium Resolution (MR) and Low Resolution (LR) groups[10]. As this study considers a telescope acting in the visible spectrum, the spatial and temporal resolutions are relevant for this analysis. They can be characterised as seen in table 2.1.

Table 2.1: Characterisation of EO satellites. Adapted from Pepper (2018).

	Spatial Resolution	Temporal Resolution
VHR	<1 m	<1 day
HR	1 - 4 m	1 - 3 days
MR	4 - 30 m	4 - 16 days
LR	>30 m	>16 days

Of these groups, the VHR market is the biggest, followed by the HR, MR and LR market[8]. This means that the potential revenue for very high-resolution telescopes is the biggest. For commercial missions, VHR is becoming a very short-term target and might even become the benchmark. Currently, the best available telescopes operate at a ground resolution of about 30 cm. To compete with these telescopes, a new telescope should have a ground resolution equal to or smaller than 30 cm. Besides the trend to VHR in the spatial regime, the need for a higher resolution in the temporal regime also becomes more apparent. For many applications, like agriculture, site monitoring and intelligence, data freshness and regular updates are highly desired.[12]

So, there is a need for high spatial and temporal resolution EO satellites. There is, however, an inverse relationship between these resolutions. Typically, the higher one of the resolutions is, the lower the other one is. This inverse relationship can be explained by the fact that the size of the aperture diameter limits the spatial resolution. Due to diffraction, the bending of light around obstacles, light spreads out through openings. This behaviour sets a lower limit as to how far point sources should be separated from each other for them to be discernible. The diffraction limit determines the achievable resolution according to the Rayleigh criterion, which describes the best possible resolution using a circular aperture as in equation (2.1):

$$\theta = 1.22 \frac{\lambda}{D} \quad (2.1)$$

Here, θ is the angular resolution, λ is the wavelength of the incoming radiation and d the aperture diameter. From this, it follows that the GSD is equal to the value seen in equation (2.2). Here, H is the altitude of the satellite.

$$GSD = 1.22 \frac{H\lambda}{D} \quad (2.2)$$

Thus, to achieve a high resolution within the visible spectrum, the aperture diameter has to be high as well. Furthermore, the focal length (F_d), or more specifically the F-number (F#), needs to be sufficiently high to decrease sensitivity to aberrations. The F-number is defined as the focal distance divided by the aperture diameter.[13] Now, having a large aperture diameter and focal length inherently means that the size and mass of the telescope, and thus the satellite, is large. To launch a satellite into space, this satellite has to be fitted into a launch vehicle. The price of a launch is tied to the volume and mass of the payload, meaning that the larger the satellite is, the costlier the launch is.

As previously stated, there is also a need for high temporal resolution telescopes. The temporal resolution is tied to the revisit time, or the time it takes for a satellite to image the same area on the ground. An EO satellite typically has a repeat cycle, which defines the number of orbits it takes to retrace the same path, and thus the time it takes to revisit the same location. Furthermore, in order to have a high GSD, the swath, which is the area covered by the telescope when passing over a region, has to be low. This low swath, in turn, means the revisit time is even higher. Therefore, in order to reach a high temporal resolution, multiple satellites combined within a constellation are required.

Concluding, to reach a high spatio-temporal resolution, a satellite constellation of high aperture diameter telescopes is required. However, as previously stated, the bigger the satellite, the more costly the launch. Combining multiple high aperture satellites can thus become very costly. Therefore, for satellite operators to successfully meet the future demand for high spatial and temporal resolution, the cost of individual launches needs to decrease significantly.

2.2. The Deployable Space Telescope

This section explains the different aspects of the DST. Firstly, how the project is set-up is discussed. This is followed by the objectives of and requirement put on the project. Finally, the mechanical budgets that flow from these requirements and are used as input for the design are presented.

The project was started in 2012 because the need for lower overall EO satellites and launch costs specifically became apparent. This led to the following market need statement, as first defined by van Marrewijk[14]:

Market Need Statement

There is a need for a dramatic decrease in launch cost of high-resolution Earth observation telescopes to provide data with a higher temporal resolution and at a lower price than is currently available.

The Deployable Space Telescope project proposes to fill this need by making a deployable telescope. The DST uses a synthetic aperture telescope which consists of multiple small and light mirror

segments. By deploying these mirror segments, the mass and stowed volume of the telescope can be decreased significantly. The mission goal of the DST is as follows[14]:

Mission Goal

To design and develop a Deployable Space Telescope (DST) that is capable of achieving the same GSD as state-of-the-art Earth Observation satellites for a fraction of the costs, by designing it to have a very low stowed volume and mass.

2.2.1. The project

The DST team consists of multiple master and PhD students under the supervision of Dr. Ir. J.M. Kuiper and Ir. J. Bouwmeester. It is split into different teams, as defined in figure 2.2. The focus within the project lies on the optical and thermo-mechanical design of the telescope. The design of the spacecraft bus is to be done at a later stage in the project. The consecutive master students working on the DST are limited in the scope of their thesis and only have a limited amount of time to work on their topic. For this reason, the project is very iterative, and attention to the systems engineering aspects needs to be given.

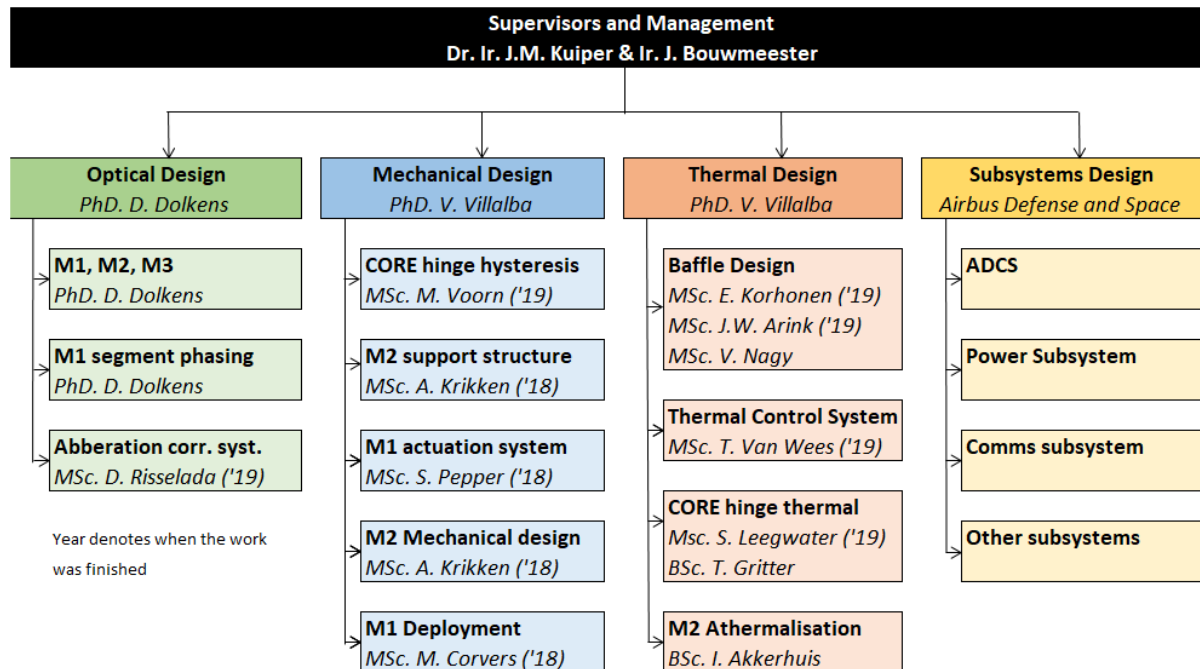


Figure 2.2: Deployable Space Telescope project structure as of March 2020.

2.2.2. Mission requirements

The main mission objectives are shown in table 2.2. From these objectives, the top-level mission requirements were set-up, as defined in Dolkens (2015). They are found in table 2.3. In setting up the requirements, the Geoeye-1 and Worldview 3/4 satellites were taken as reference. They are considered to be the state-of-the-art EO satellites and as such provide a good baseline for what the DST should be capable of. The requirements, however, exceed those set for the reference telescopes, as there are considerable challenges in designing a synthetic aperture telescope. A full list of mission, system and subsystem requirements is found in appendix A. [1]

Some of the requirements presented in table 2.3 contain a goal and a threshold requirement. The threshold requirements are hard requirements and must be met for the mission to be a success. In designing the DST, the aim is to meet all goals; however, if they are not met, the mission is not killed. They must, however, be kept in mind in the design philosophy of the DST. A short explanation follows the requirements presented in table 2.3. For a more in-depth explanation, the work of Dolkens[1, 15]

Table 2.2: DST objectives.

ID	Description
MIS-OBJ-01	The Ground Sample Distance of the DST shall be no larger than the state of the art in commercial visual spectrum Earth Observation imaging platforms. As of 2017 this is DigitalGlobe's WorldView-4 satellite with a Ground Sample Distance of 0.31 m in the panchromatic band.
MIS-OBJ-02	The lifetime cost of the DST shall be less than the state of the art in commercial visual spectrum Earth Observation imaging platforms. As of 2017 this is DigitalGlobe's WorldView-4 satellite with an estimated cost of USD \$850 million including ground network upgrades.

should be examined.

2.2.3. System budgets

Due to mirror misalignment and deformation between the first and secondary mirrors, an optical path difference may arise. The design of a deformable mirror to correct for optical aberrations in the wave-front is presented in van Marrewijk (2018). The Aberration Correction System (ACS), as outlined in section 2.3, corrects for changes within the optical path up to a certain threshold value. To make sure that these values are not exceeded, and thus that the aberrations can be corrected for, the alignment of the mirrors has to stay within a set of boundaries. This set of boundaries is defined as mechanical budgets, as presented in table 2.4.

The different budgets as seen in table 2.4 are, as adapted from Pepper (2018), defined as follows:

1. **Deployment budget** *The maximum allowable deviation of the position of the optical surface from the desired datum after deployment and prior to coarse (or fine) calibration. This only applies to the deployable elements: M1 and M2.*
2. **Coarse alignment** *The maximum allowable deviation of the position of the optical surface from the desired datum after coarse alignment. This only applies to the active optics elements: M1 and M3.*
3. **In-orbit drift budget** *The maximum allowable spatial deviation of an optical surface that can occur between completion of the last active calibration procedure and the end of the next image acquisition, provided that the deviation can be considered (pseudo-)static over the period of image acquisition.*
4. **Stability budget** *The maximum allowable spatial deviation of an optical surface during image acquisition. Note that this only applies during image acquisition.*

The in-orbit drift budget refers to the spatial variation of the mirror over a large period of time (Δt_{drift}), while the stability budget period (Δt_{stable}) is small. Δt_{drift} is chosen to be equal to the time that the satellite is in sunlight, while Δt_{stable} is equal to one image acquisition period. The coarse alignment budgets are valid during eclipse, and are used to ensure the mirror alignment control algorithms can converge to a steady solution after the eclipse.[4]

2.3. Deployable Space Telescope concept

The DST uses a Korsch Annular-Field Four Mirror Anastigmat (AFTMA), for which the optical layout can be seen in figure 2.3. This type of telescope is used because it has several beneficial properties for a segmented mirror system. Firstly, because it is fully reflective, no chromatic aberrations are introduced to the image. Secondly, the Korsch design is inherently corrected for spherical aberration, coma, astigmatism and field curvature.[16] Furthermore, to protect the secondary image of a Cassegrain type telescope, it conventionally requires e. However, because the tertiary mirror is placed within the instrument housing in a Korsch AFTMA, it is inherently baffled. Lastly, the instruments are easily accessible because they are placed immediately behind the exit pupil[16]. Dolkens and Kuiper (2017) introduced

Table 2.3: DST requirements. As adapted from Dolkens (2015).

ID	Description
REQ-1	<p>The GSD of the instrument shall be equal to 25 cm in the panchromatic band from an orbital altitude of 500 km.</p> <p><i>The Worldview 3 and 4 satellites respectively reach a GSD of 31 and 34 cm. The DST is set to operate from an altitude of 500 km, compared to an altitude of 617 km for the Worldview satellites. Applying linear magnification, a system offering a 25 cm GSD at 500 km is equivalent to the other state-of-the-art telescopes, so this is the requirements set on the GSD.</i></p>
REQ-2	<p>The swath width of the instrument shall be wider than 1 km (threshold) / 5 km (goal).</p> <p><i>Because it is very challenging to design a synthetic aperture telescope with a very small GSD but a high swath, the requirement is set significantly lower than the swath width of the WorldView satellites (at 13.1 km).</i></p>
REQ-3	<p>The system shall have one panchromatic channel (with a GSD of 25 cm) and four multi-spectral bands (blue, green yellow and red at a GSD of 100 cm).</p> <p><i>To achieve a good SNR ratio with the segmented aperture, not all spectral bands featured in the Worldview satellites are included. The bandwidth of the panchromatic band is limited at 200 nm to make the design of the calibration system easier. The multispectral bands have a GSD 4 times than that of the panchromatic channel to be able to capture sufficient data.</i></p>
REQ-4	<p>The SNR of the instrument shall be higher than 100 for a reflectance of 0.30 and a sun Zenith angle of 60°</p> <p><i>To allow for image processing algorithms to be used effectively, the SNR must be sufficiently high.</i></p>
REQ-5	<p>The nominal MTF at both the Nyquist frequency and half the Nyquist frequency shall be higher than 5% (threshold) / 15% (goal).</p> <p><i>The 5% threshold is used as this is deemed feasible with a synthetic aperture instrument. It is quite low compared to other instruments, but is deemed sufficient. The threshold is however set at 15%, as this relaxes the requirements set on the SNR.</i></p>
REQ-6	<p>After calibration, the residual Strehl ratio of the system shall be higher than 0.80.</p> <p><i>The required Strehl ratio is set to 0.80 as this is typically seen as the diffraction limit. A value higher than 0.80 should not lead to any noticeable deterioration in image quality.</i></p>
REQ-7	<p>The mass of the instrument shall be lower than 100 kg (threshold) / 50 kg (goal).</p> <p><i>To decrease launch cost, the mass should be as low as possible. The goal for the instrument mass is set at 50 kg, as at this mass the satellite would still be considered to be a microsatellite. The threshold is set at 100 kg. Although the satellite is not considered a microsatellite anymore, it is still much lighter than comparable systems.</i></p>
REQ-8	<p>In the stowed configuration, the volume of the instrument shall not exceed 1.5 m³ (threshold) / 0.75 m³ (goal).</p> <p><i>To decrease launch cost, the stowed volume should be as low as possible. The threshold is set at 1.5 m³, which means a decrease in volume of a factor 2 compared to similar systems. The goal is set at 0.75 m³, at 1/6th the volume of a similar system this is very challenging but might be possible.</i></p>

one modification on a typical Korsch AFTMA, by replacing the first fold mirror by a freeform mirror. This ensures a diffraction limited performance for the complete Field of View (FOV) of the panchromatic channel[15].

The optical layout can be seen in figure 2.3. The Primary Mirror (PM) and Secondary Mirror (SM) form the Cassegrainian part of the telescope. The Cassegrainian provides the biggest part of the mag-

Table 2.4: Mechanical mirror alignment budgets. Retrieved from Pepper (2018).

Element	Position			Orientation			Radius [%]	Shape Error [nm]
	X [μm]	Y [μm]	Z [μm]	X [μrad]	Y [μrad]	Z [μrad]		
<i>Deployment/ Coarse Alignment Budget</i>								
M1	2	2	2	2	4	50	1×10^{-3}	50
M2	15	15	10	100	100	100	1×10^{-2}	25
M3	4	4	4	10	10	50	1×10^{-3}	10
<i>In-Orbit Drift Budget</i>								
M1	2×10^{-2}	2×10^{-2}	2×10^{-2}	1×10^{-2}	2×10^{-2}	5	1×10^{-4}	5
M2	4	4	2	6	6	12	1×10^{-4}	5
M3	1×10^{-1}	1×10^{-1}	1×10^{-1}	1	1	5	1×10^{-4}	5
<i>Stability Budget</i>								
M1	5×10^{-3}	5×10^{-3}	5×10^{-3}	2.5×10^{-3}	1×10^{-2}	5×10^{-1}	n/a	n/a
M2	1	1	5×10^{-1}	1.5	1.5	3	n/a	n/a
M3	2.5×10^{-2}	2.5×10^{-2}	2.5×10^{-2}	2.5×10^{-1}	2.5×10^{-1}	1.25	n/a	n/a

nification of the telescope and forms a real image just behind SM. This secondary image is re-imaged on the Deformable Mirror (DM) by the Tertiary Mirror (TM) at approximately unit magnification.[16] The DM corrects the optical path differences in the exit pupil using the ACS[14]. Part of the image is then reflected to the two panchromatic detectors (Time Delay and Integration (TDI) sensors), TDI-1 and TDI-2. TDI-1 is the primary high resolution channel, while TDI-2 is slightly defocused to enable the sensing of aberration using phase diversity[15]. Lastly, the Fold Mirror (FM) reflects the light onto the multispectral sensors and wavefront (or sharpness) sensor.

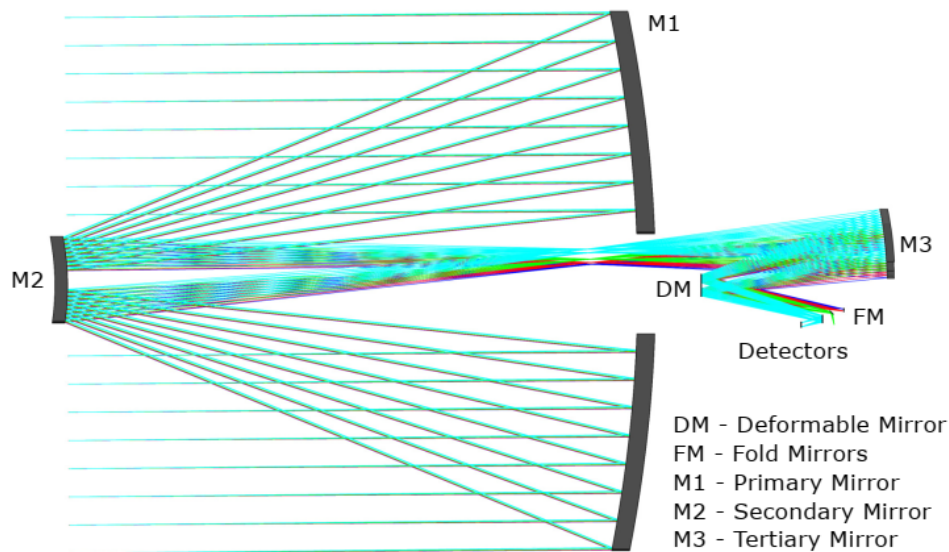


Figure 2.3: Optical layout of the Deployable Space Telescope. Retrieved from Pepper (2018).

2.4. Deployable Space Telescope architecture

In this section, the current design (April 2020) of all components of the telescope is presented. This entails the designs as proposed up to and including the work presented in Arink (2019). Some components are already finalised while some still need to be designed from scratch. Due to the iterative nature of the project, the design will be subject to change in the future. A schematic view of the DST can be seen in figure 2.4. Note that, even though the interface with the spacecraft bus is visualised, it is assumed to be designed at a later point and is therefore not further discussed. The discussion of the design is split into five parts. Firstly, the instrument housing and its components are handled.

This is followed by the primary mirror and its support structure and later the secondary mirror and its support structure. Next, the deployable baffle is reviewed. Lastly, a design review is presented. In the architecture of the DST, a distinction is made between the deployed and stowed positions. During the Launch and Early Operations (LEOP), the primary and secondary mirrors and the baffle are in stowed position. At the end of LEOP, the deployment sequence is started. Then, in the operational phase, all components are in the deployed position.

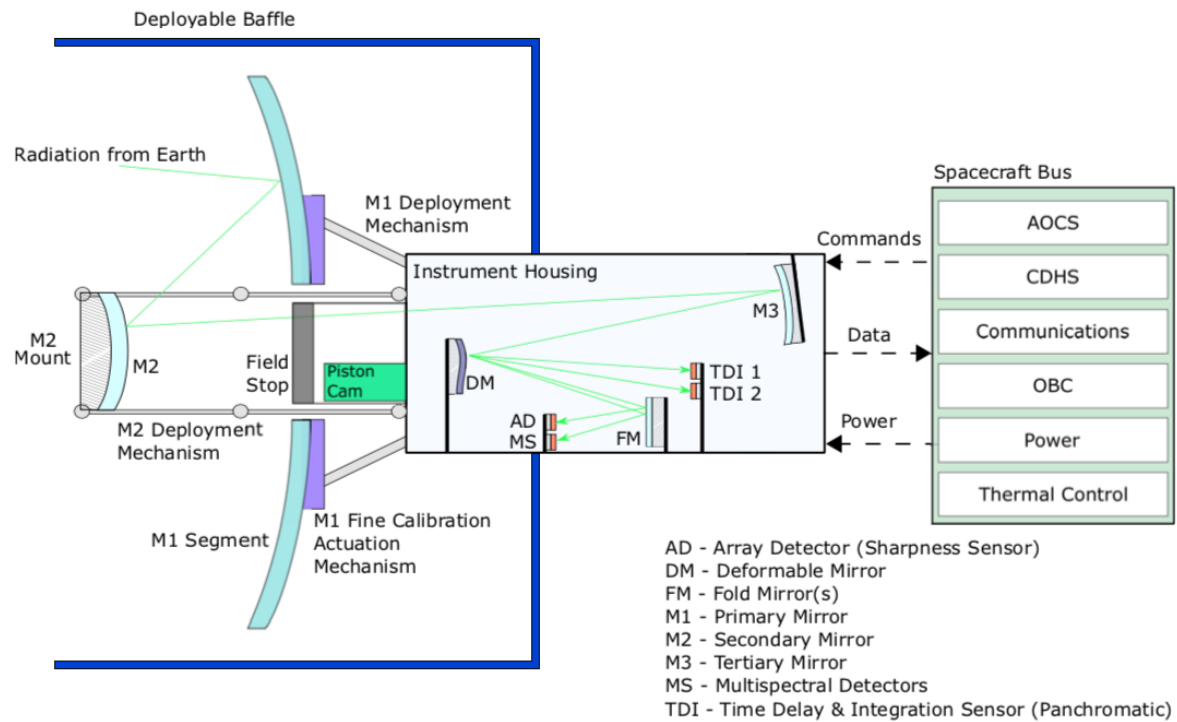


Figure 2.4: Schematic of the Deployable Space Telescope. Adapted from Pepper (2018).

In figure 2.5 the telescope is shown with the coordinate system used in this thesis. For clarity, the components obscuring the view of the coordinate system are hidden. The x-y plane of the coordinate system is placed on top of the instrument housing. The z-axis is positive in the direction going from the instrument housing towards the secondary mirror.

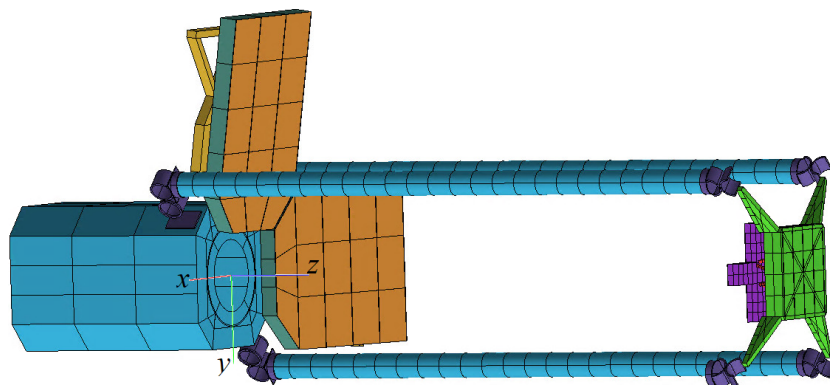


Figure 2.5: Coordinate system of the Deployable Space Telescope.

2.4.1. Instrument housing

The instrument housing, as seen in figure 2.4, first and foremost houses the different instruments of the telescope. It furthermore acts as the interface between the satellite and the primary and secondary mirrors are mounted against it. Within the instrument housing the tertiary, deformable and fold mirrors, all detectors and a piston cam are placed. The purpose of the different mirrors is presented in section 2.3 and is therefore not discussed here. The field stop is permanently attached to the instrument housing and acts to reduce the amount of stray light entering the instrument housing. The piston cam is used to detect misalignment of the primary mirror segments.

2.4.2. Primary mirror & support structure

The primary mirror consists of four mirror segments. They are tapered in the centre to create an interface for edge sensors[15], which are used to measure relative mirror gaps and heights. The PM segments consist of Silicon Carbide (SiC), because SiC provides for good thermal and mechanical properties at a low cost[1]. They are attached to the instrument housing by the Primary Mirror Support Structure (PMSS). An overview of the primary mirror and the PMSS can be seen in figure 2.6. On the left, the mirrors are in stowed position, while on the right they are in deployed position. The PMSS consists of two parts, the Primary Mirror Deployment (PMD) mechanism and the PM fine positioning system, or Primary Mirror Active Optics (PMAO) mechanism, which is mounted on the deployment mechanism. The mirror segments are supported by the PMAO mechanism.

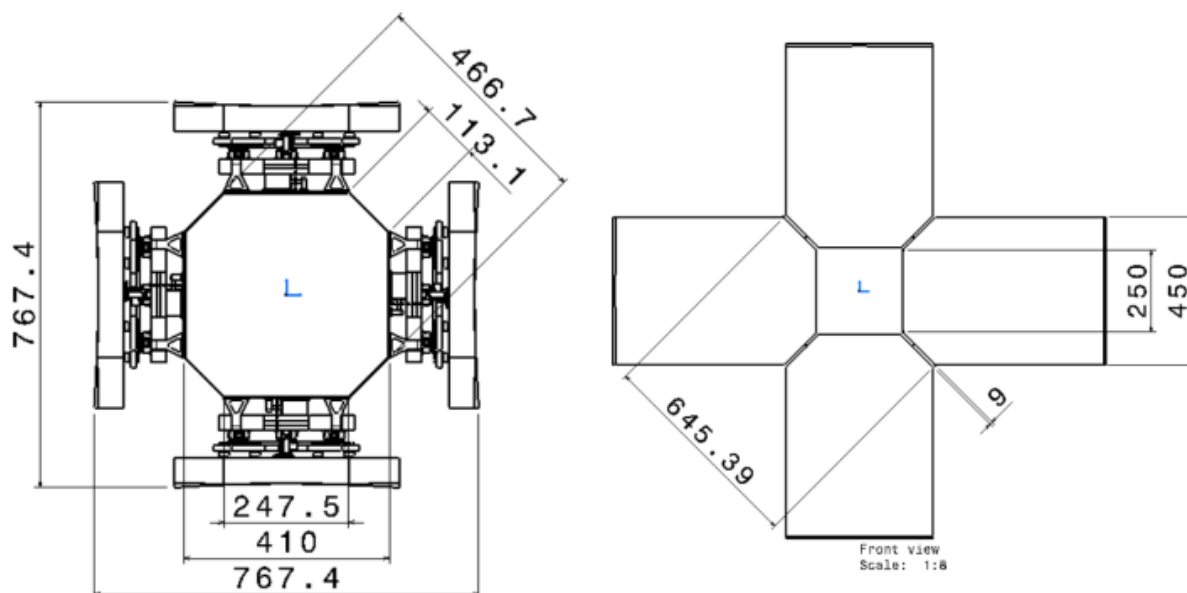


Figure 2.6: Stored (left) and deployed (right) configuration of the primary mirror and its support structure. Retrieved from Krikken (2018).

Primary mirror deployment mechanism

The PMD mechanism is the interface between the instrument housing and the PMAO mechanism. It is used to deploy the PM. The PM support frame, as seen in figure 2.8, directly supports the PMAO mechanism. Several concepts were proposed for the deployment mechanism, such as the kinematic interface shown in figure 2.7, and a ribbon system connecting the PMSS and the SMSS were proposed. However, both proposals were deemed unacceptable, meaning that currently (August 2020) there is no final design.

The first concept for the deployment mechanism consists of a Carbon Fibre Reinforced Polymer (CFRP) tube with three tape-strain energy deployment hinges, one at the top, middle and bottom. These hinges are similar to tape spring hinges as are used in measuring tape. They are flexible when rolled up, but "click" into place when straightened. The strain energy deployment hinges are made by cutting out material from a hollow CFRP tube. They work on the principle of elastic deformation of the hinge material. When released after storage, the elastic energy forces the hinge to straighten out.

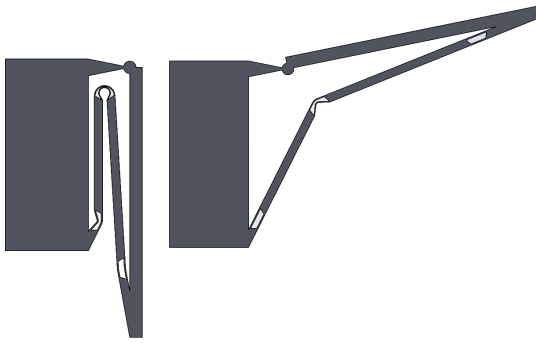


Figure 2.7: Primary mirror deployment mechanism in stowed position (left) and deployed position (right). Adapted from Corvers (2018).

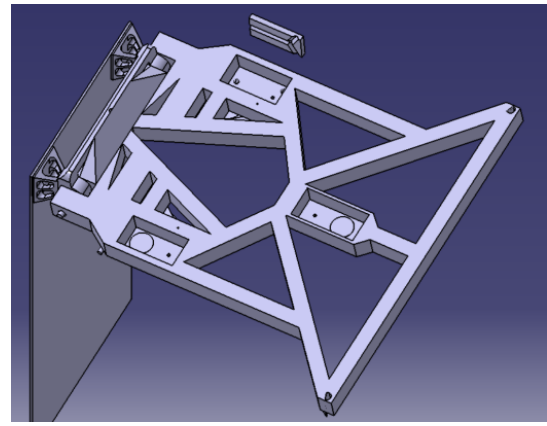


Figure 2.8: Primary mirror support frame. Retrieved from Corvers (2018).

Then, because of the circular shape of the cut-outs, the stiffness of the structure increases significantly as the hinges straighten out and lock into their deployed state.[3]

The second concept for the deployment mechanism consists of ribbons extending from the support frame to the SMSS. After deployment of the SM, a winch mechanism provides the necessary force to deploy the support frame. In deployed state, the ribbons provide preload to both the PMSS and the SMSS. This stiffens the system and thus reduces vibrations.[3] A discussion on the matter with Airbus, however, resulted in the advise to not attach the ribbons to the PM support frame. A different system without ribbons or where the ribbons are connected to the instrument housing itself is required (personal communication, V. Villalba, 14 October 2019). An additional design effort is thus required to finish the design of the primary mirror deployment mechanism.

The deployment mechanism supports the support frame. The exact composition of the support frame is not yet defined. Corvers (2018) proposes to use a design consisting in parts of aluminium and CFRP, which makes the design athermal. Athermalisation is a measure to make the design independent of temperature differences. In this case, it comprises of using materials with a different Coefficient of Thermal Expansion (CTE) to effectively cancel the relative spatial movement of different parts. The concept of athermalisation is further discussed in section 2.5 and chapter 4. The design is optimised for mass and volume by cutting away material, as seen in figure 2.8.

Primary mirror active optics mechanism

On top of the support frame lies the PMAO mechanism. It makes sure the primary mirror alignment is maintained throughout the satellite's orbit. It uses a three Degree of Freedom (DOF) piston/ tip/ tilt fine positioning mechanism to actively align the primary mirror segments. First, a fixed frame provides the foundation for the mechanism and the interface to the support frame. On top of this frame, compliant flexure elements are placed to provide the necessary constraint. Finally, four piezoelectric actuators are arranged in push/ pull pairs to drive the mechanism that positions the mirror.[2]

2.4.3. Secondary mirror & support structure

The secondary mirror consists of a single mirror segment. It is again made out of SiC, for the same reasons as mentioned in section 2.4.2. An overview of the whole telescope can be seen in figure 2.9. The instrument housing, PMSS and PM can be seen respectively at A, B and C. As of the design presented in Krikken (2018), the secondary mirror (I), is deployed by the Secondary Mirror Deployment Mechanism (SMDM), which consists of four deployment booms (E). Krikken proposes a SM interface consisting (H) of six rods, which forms the interface between the SM and the spider (G). The deployment booms, also called metering booms, are connected to the instrument housing and the spider by two Compliant Rolling Element (CORE) hinges (D & F).[3]

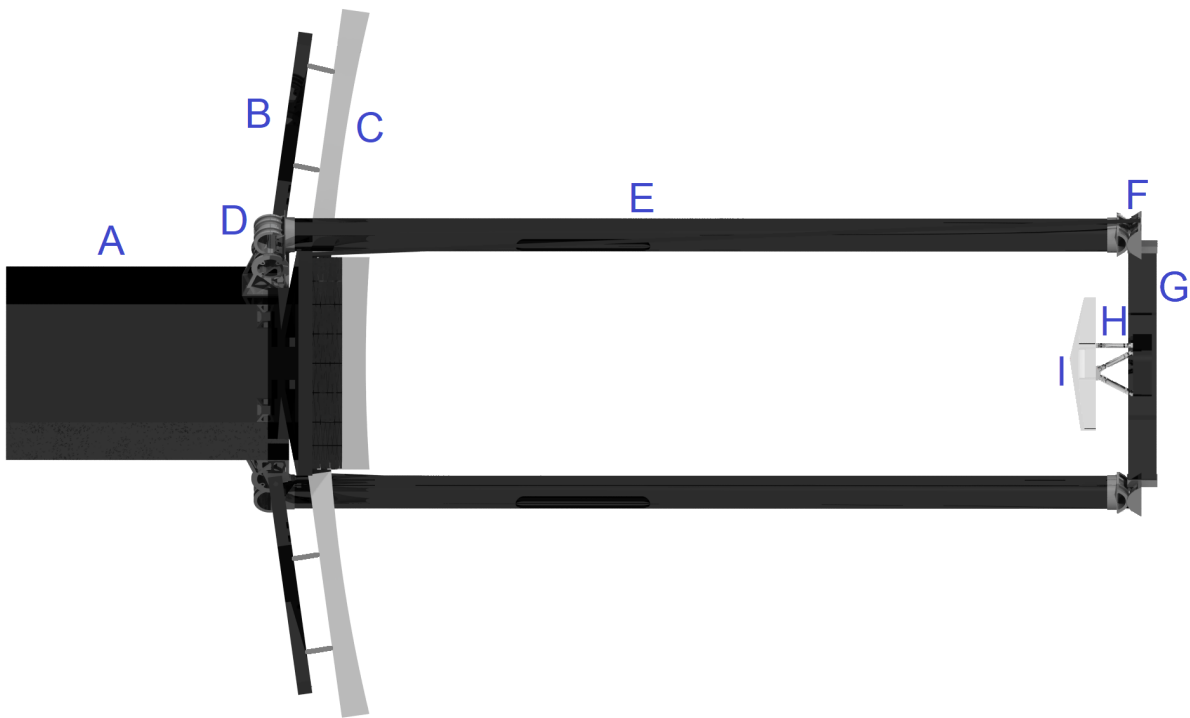


Figure 2.9: Design overview of the telescope. Adapted from Voorn (2019).

Secondary mirror deployment mechanism

The primary deployment mechanism of the SM is the deployment boom. It is a strain energy deployment hinge made out of CFRP. This deployment method is used because of its low mass and complexity, its high accuracy and repeatability and its excellent thermal properties. The working principle of the deployment booms can be seen in figure 2.10. After production, the boom is in its initial configuration (top-left). It is then consecutively flattened (top-middle) and folded (top-right) until it reaches its stowed configuration (bottom-left). At the end of the LEOP, the mechanism is deployed into its final position. The layup of the carbon fibre layers is not yet known, so the exact properties of the booms remain to be defined.[3]



Figure 2.10: Working principle of tape spring. Retrieved from Mallikarachchi and Pellegrino (2010).



Figure 2.11: The CORE hinge. Retrieved from Halverson (2007).

The booms are connected to the instrument housing and spider by the CORE hinges. An example of these hinges is shown in figure 2.11. The CORE hinges consist of two cylinders, the cams, rolling over each other. They are connected by a set of thin strips. The CORE hinges are used because of their low hysteresis and friction while forming a strong connection. The cams and the three strips are made of titanium alloy (Ti-6Al-4V). [3]

Spider & secondary mirror interface

The spider chiefly acts as the connection point of the deployable booms and the SM interface. It is a cross consisting of CFRP, as can be seen in figure 2.12. The spider's legs are connected to the deployable booms via the CORE hinges. In the middle, a circular structure is added on which the SM interface rods are mounted. Four cross beams are included to increase the stiffness of the spider. The legs are tapered, increasing in height going towards the centre.[3]

The SM interface rods can be seen in figure 2.13. It is a hexapod structure, where each rod constraints one DOF. The hexapod design allows for relative thermal expansion of the spider and the mirror while keeping the mirror exactly constraint. The interface rods are made of aluminium 7075-T6. The combination of materials and lengths for both the deployment booms and the interface rods is chosen such that the distance between the primary and secondary mirror is as stable as possible. Some problems, however, remain in this stabilisation procedure. An in-depth discussion on these problems is given in section 2.5.[3]

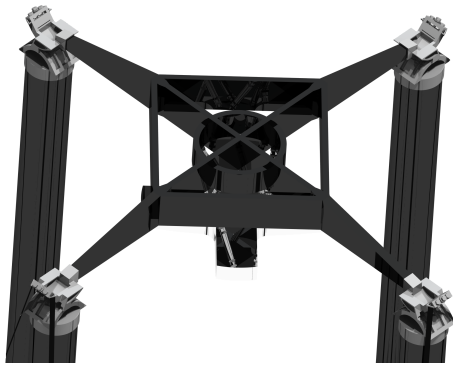


Figure 2.12: The spider. Adapted from Krikken (2018).



Figure 2.13: The secondary mirror interface. Adapted from Krikken (2018).

2.4.4. Deployable baffle

As described previously, the performance of the system can be affected by the translation of the secondary mirror due to thermoelastic expansion of materials. To guarantee proper performance of the system, these translations have to be cancelled out or avoided entirely. The variation in temperature of the different components arises due to differing external circumstances, mainly because the satellite is sometimes in direct sunlight and sometimes in eclipse. Now, instead of making the system completely athermal, it is also possible to decrease the change in temperature of the individual components. In the case of the DST, this is done using a deployable baffle. The final design of the baffle, as presented in Arink (2019), can be seen in figure 2.14. The purpose of the baffle is to guarantee a stable thermal environment. It furthermore acts to attenuate internal and reject external stray light and is also used to mitigate debris and micrometeoroid impacts.[4]

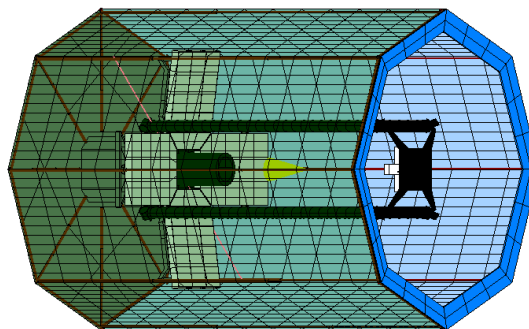


Figure 2.14: Baffle in deployed configuration. Note that the baffle is made transparent to make the overview more clear. Retrieved from Arink (2019).

The baffle consists of an octagonal telescopic structure around which different layers of Multi Layer Insulation (MLI) and coatings are placed. The deployment system, as seen in figure 2.15, consists of hollow square telescopic booms made of M55J CFRP. It has a deployment ratio of 3 both in axial and radial direction, meaning that in both directions three telescopic booms are used. The telescope is shielded from the sun by five layers of MLI. This amount of layers was determined to be the optimal combination of foldability and thermal shielding at a low mass. The baffle is coated on the outside by a SiOx/VDA/Kapton layer with an emissivity of $\epsilon = 0.14$ and a solar absorptivity of $\alpha_S = 0.17$. To reduce the amount of stray light, the baffle is coated on the inside with Magic Black with an emissivity of $\epsilon = 0.84$ and a solar absorptivity of $\alpha_S = 0.93$. [4]

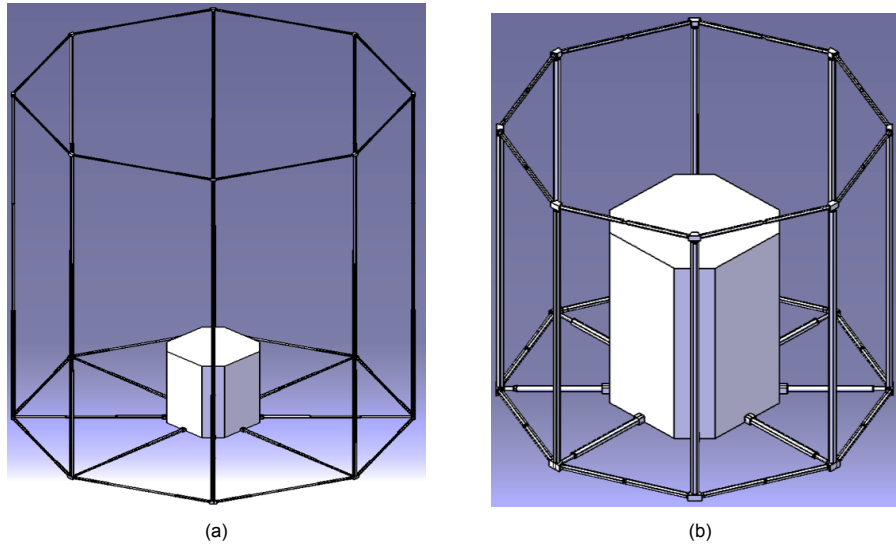


Figure 2.15: Baffle deployment system in a) deployed and b) stowed position. Retrieved from Arink (2019)

2.5. Thesis

The in-orbit drift budgets, as shown in table 2.4, are not yet met. This means that the stabilisation of the secondary mirror is not complete. Here, stabilisation means to keep the deviation of the position and orientation of the secondary mirror with respect to the primary mirror within the specified budgets. The work of Krikken (2018) and Arink (2019) have both contributed to stabilising the secondary mirror, but neither fulfilled all requirements. Naturally, other design tasks remain, but the focus of this thesis lies on the stabilisation of the SM. This section starts with a discussion on the principles behind and quantification of the translation and rotation of the secondary mirror. This is followed by the need and goal and the research questions of this thesis. Finally, the methodology by which the thesis is performed is presented.

2.5.1. The problem

For the correct performance of the telescope, the position and orientation of the primary and secondary mirror must deviate as little as possible. The amount of allowed deviation is summarised in the alignment budgets of the mirrors and can be found in table 2.4. In previous work, the in-orbit drift in longitudinal position and orientation around the X- and Y-axis were found to be critical for the alignment budgets. This is supported by the sanity check as presented in chapter 3. These budgets are, therefore, considered in this analysis to be the main problem. The allowed in-orbit misalignment in longitudinal direction is equal to $2\mu m$ and in rotation around the X- and Y-axis $6\mu rad$.

As the telescope orbits Earth, it is subject to radiation, mainly coming from the Sun and Earth. The amount of radiation depends on the location of the satellite in its orbit. The satellite experiences the highest amount of radiation when it is in direct sunlight and the lowest when it is in eclipse, where the Earth blocks the radiation coming from the Sun. These fluctuations in incoming radiation cause the temperature of the telescope and its components to swing throughout its orbit. The baffle dampens

this effect by blocking out most direct sunlight, which effectively decreases the change in temperature of the telescope over an orbit. However, the temperature does still vary, as is summarised in table 3.4. These variations can alter the position and orientation of the secondary mirror. This variation is caused by the thermoelastic expansion of materials. Here, the longitudinal (Z) position and the orientation around the X- and Y-axes are considered, because they are most affected by temperature variations. Thermoelastic expansion is governed by a simple equation, as seen in equation (2.3). Here, ΔL is the expansion of the component, α is the coefficient of thermal expansion, ΔT the change in temperature and L the initial length of the component. Note that the CTE is given in $\mu\text{m}/\text{m}\cdot\text{K}$.

$$\Delta L = \alpha \Delta T L \quad (2.3)$$

Every component has its own CTE, length and change of temperature. The translations and rotations of the secondary mirror are therefore governed by the individual expansion of all components placed between the primary and secondary mirror. In general, the secondary mirror translates and rotates as shown in figure 2.16.

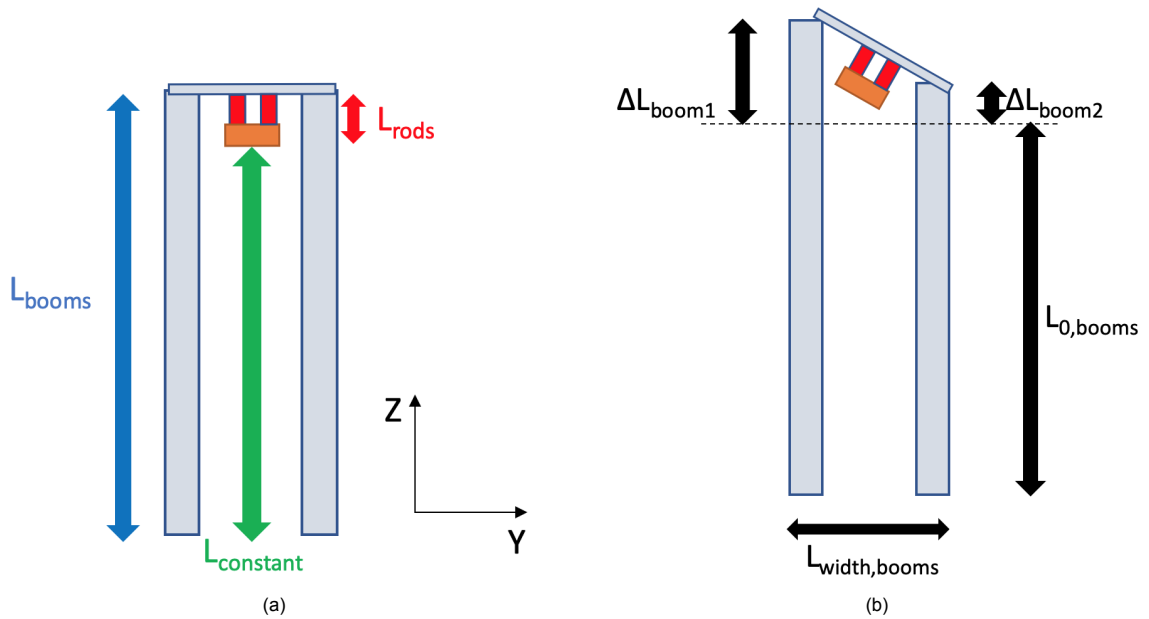


Figure 2.16: a) Translation and b) rotation of secondary mirror. Adapted from Arink (2019).

The different components that influence the position and rotation of the secondary mirror (and its focal point) with regards to the primary mirror are the deployment booms, the CORE hinges, the rods, the SM itself and possibly the spider. Note that the primary mirror is not included in this analysis, because it is actively controlled by the PMAO. A full overview of the relevant components and their lengths is found in Figure 2.17.

When the deployment booms experience an increase in temperature, they expand longitudinally away from the primary mirror. In principle, the proper combination of fibres with positive and negative coefficients can result in a composite material with zero thermal expansion.[21] However, because in the design of strain energy deployment hinges other material constants are at least as important, it is assumed that the composite is not optimised for zero thermal expansion. A low CTE of $0.8 \mu\text{m}/\text{m}\cdot\text{K}$ is however assumed to be achievable, and is used in Krikken (2018) and Arink (2019). As visualised in Figure 2.17, the total length of the deployment booms (L_B) is equal to the variable boom length (L_{BV}) plus the constant boom length (L_{BC}). L_{BC} is the part of the deployment boom in between the primary mirror and the root CORE hinges and is equal to 125.25 mm. Note that an expansion of the spider has a negligible effect on the longitudinal variation of the deployment boom length (tilting of the deployment booms due to a 10 K change has an effect in the order $O(10^{-12})$ m).

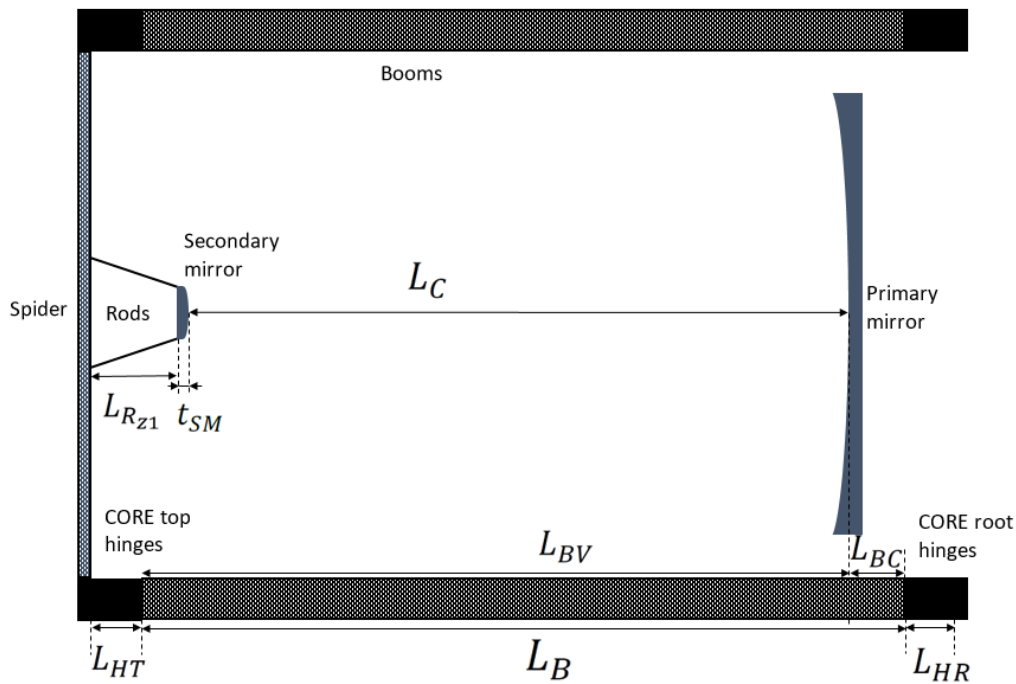


Figure 2.17: Schematic overview of the relevant lengths of the secondary mirror deployment system.

The CORE hinges are made of titanium (Ti-6Al-4V), which has a CTE of $8.6 \mu\text{m/m.K}$ [22]. It is assumed that the CORE hinges expand linearly. Even though this probably is not the case, this assumption should be sufficient for the purposes of this study. This is the case, because only the total expansion of the CORE hinges in longitudinal direction, which should be near linear expansion, is of importance. Local non-linear thermal expansion effects are not considered in this work, but are of importance in enabling proper performance of the hinges. The part of the hinges that increase the longitudinal distance between the mirrors can be seen in Figure 2.18. Here, the lengths of the root (L_{HR}) and top (L_{HT}) CORE hinges is taken as the distance between the deployment boom and the attachment point to the surrounding structures. L_{HR} is equal to 66.25 mm and L_{HT} is equal to 51.91 mm.

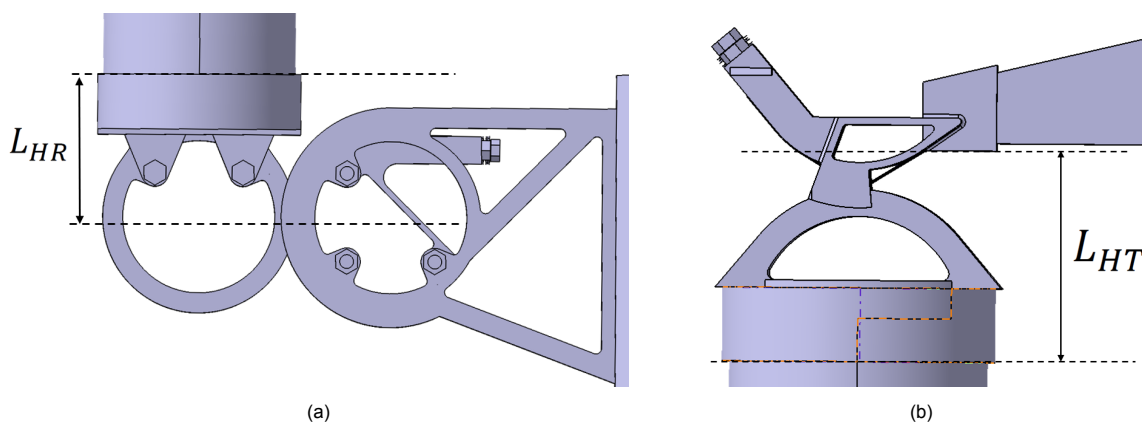


Figure 2.18: Lengths of a) the root and b) the top CORE hinges that increases the length between both mirrors due to thermal expansion.

The interface rods are made from aluminium 7075-T6. This was chosen because of its high stiffness and CTE values. With a CTE of $23.6 \mu\text{m/m.K}$ [22], they do not need to be excessively long to provide compensation for the expansion of the deployment booms. As the secondary mirror and the spider are

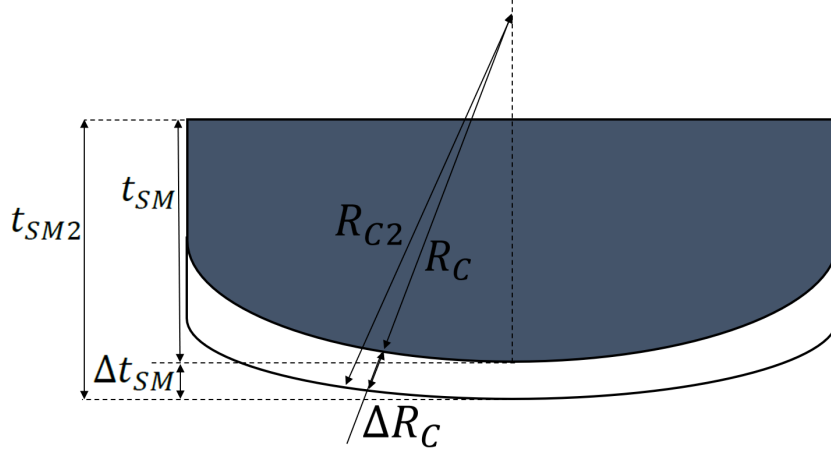


Figure 2.20: Schematic overview of the expansion of the mirror and its radius of curvature.

at nominal temperature. Equation (2.8) describes the longitudinal translation of the secondary mirror. Note that these equations are based on a SMSS using a hexapod structure. Of course, when another secondary mirror support is used, the part relating to the rods is either changed or removed.

$$\begin{aligned}
 L_C &= L_B + L_{HT} + L_{HR} - L_{RZ} - t_{SM} = L_B + L_{HT} + L_{HR} - L_{RZ} - t_{SM} \\
 1600 &= L_B + 51.91 + 66.25 - L_{RZ} - 40 \\
 L_B - L_{RZ} &= 1571.07 \text{ mm}
 \end{aligned} \tag{2.7}$$

$$\begin{aligned}
 \Delta Z &= \Delta L_B + \Delta L_{HT} + \Delta L_{HR} + \Delta z_{R2} + \Delta z_{R3} + \Delta t_{SM} + \Delta F_e \leq 2 \text{ } \mu\text{m} \\
 \Delta Z &= \alpha_B L_B \Delta T_B + \alpha_H (L_{HT} \Delta T_{HT} + L_{HR} \Delta T_{HR}) - L_{R_x} (\tan \psi_2 - \tan \psi_1) + \\
 &\quad L_R (\sin \psi_1 - \sin \psi_3) - \alpha_{SM} t_{SM} \Delta T_{SM} + \Delta F_e \leq 2 \text{ } \mu\text{m}
 \end{aligned} \tag{2.8}$$

Next to the translation of the secondary mirror, a change in temperature might also mean a rotation of the mirror around the X- and Y-axes. Obviously, in the nominal situation the mirror should be placed perpendicular to the longitudinal axis. The rotation of the mirror is calculated by finding the difference in expansion between the different opposing components. An example of such a difference in expansion can be seen in figure 2.16b. The angle of rotation (γ) of the secondary mirror is defined by the expansion of the booms, CORE hinges and rods and is defined in equation (2.9).

$$\begin{aligned}
 \Delta \gamma &= \tan^{-1} \left(\frac{\Delta L_{B_P} + \Delta L_{HT_P} + \Delta L_{HR_P} - \Delta L_{B_N} - \Delta L_{HT_N} - \Delta L_{HR_N}}{w_{Sp}} \right) - \tan^{-1} \left(\frac{\Delta L_{R_P} - \Delta L_{R_N}}{w_{M2,a}} \right) \leq 6 \text{ } \mu\text{rad} \\
 \Delta \gamma &= \tan^{-1} \left(\frac{\alpha_B L_B (\Delta T_{B_P} - \Delta T_{B_N}) + \alpha_H (L_{HT} (\Delta T_{HT_P} - \Delta T_{HT_N}) + L_{HR} (\Delta T_{HR_P} - \Delta T_{HR_N}))}{w_{Sp}} \right) - \\
 &\quad \tan^{-1} \left(\frac{\alpha_R L_R (\Delta T_{R_P} - \Delta T_{R_N})}{w_{M2,a}} \right) \leq 6 \text{ } \mu\text{rad}
 \end{aligned} \tag{2.9}$$

The position and orientation of the secondary mirror is thus dependant on the combination of length, temperature variation and CTE of the deployment booms, interface rods, CORE hinges and secondary mirror. Any design for the SMSS has to fulfil all three equations (2.7) to (2.9). This can be done using different methods, as discussed in chapter 5. The first method is by athermalising the system, which consists of varying the materials and lengths of the components. The second method lies in controlling the temperature of the components by applying thermal control. Lastly, the secondary mirror can be actively actuated by means of actuators. In this report, all three methods are explored.

In this work, it is initially assumed that the work of Krikken (2018) is conceptually correct. The concepts used in Krikken (2018), as discussed in section 2.4.3, are applied. The choice of materials and length of the different component, however, are examined. Only when no working solution using

those concepts can be found, a conceptual change is implemented. The thermal model, as outlined in Arink (2019), is used and improved. The results from the thermal model are used as input to calculate the thermoelastic expansion of the relevant components. This model is also used to find the unknown temperatures as seen in table 3.4. As new concepts are generated, it is also used to generate new results.

2.5.2. The Research

Considering the problems outlined previously, the thesis need and goal are presented here. Firstly, the thesis need is as follows:

Thesis Need

To ensure the optical performance requirements of the Deployable Space Telescope are met, the in-orbit drift budgets may not be exceeded. For this end, there is a need to make sure the relative distance between the primary and secondary mirror is stable over the satellite's orbit.

The thesis goal is as follows.

Thesis Goal

To improve the design of the secondary mirror support structure such that the translations and rotations of the secondary mirror are as low as possible and at least do not exceed the set drift budgets. The design should furthermore adhere to all requirements imposed on the telescope and be feasibly implemented within the scope of the Deployable Space Telescope.

The main research questions follows naturally from the thesis goal and is as follows:

What is the best feasible design of the secondary mirror support structure that adheres to all requirements?

Because the research consists of a design procedure, it is hard to make unambiguous and measurable parameters which determine the quality of the design. The best design is rather the end-product of the design procedure, so the result of a series of different design choices, than something that is currently measurable. Further sub-questions are presented in table 2.5. These sub-questions aim to help in finding the best feasible design. Firstly, by determining what requirements are posed on the SMSS. By defining the required functionality of the design, and finding what defines the feasibility of the design, the full list of requirements can be set-up. When the requirements are known, the concepts that can potentially meet those requirements are identified. This is done by first determining what trade-off method should be used, then setting-up the trade-off criteria and weights and finally performing the trade-off. The next step in the design procedure is to perform a detailed design procedure. This procedure is then followed by answering the last sub-question, namely whether the design can feasibly be implemented within the DST. This question is answered by first verifying the design and then validating the functionality of the SMSS. The questions above, and their respective sub-questions, are summarised in table 2.5. The answers to these questions follow in chronological order in this thesis, and are summarised in chapter 8.

2.5.3. Methodology

The methodology followed in the design procedure is that of the V-model, as visualised in figure 2.21. The V-model life-cycle development model is widely used in systems engineering and development. It can be recursively and iteratively applied at each level of the system's hierarchy, which makes it ideal for the upcoming design procedure.[25]

In the V-model, the mission functional needs are defined at the start of the project. Because these are already partly defined for the DST, the first task of this thesis is to check these defined needs and the

Table 2.5: DST research question.

ID	Research question
SUB-1	What requirements should the SMSS adhere to?
SUB-1.1	What functionality should the SMSS have?
SUB-1.2	What defines the feasibility of the design?
SUB-1.3	What requirements follow from the functionality and feasibility?
SUB-2	What concept should the design of the SMSS be based on?
SUB-2.1	What are the main input parameters on which the design is based?
SUB-2.2	What concepts can potentially meet the requirements?
SUB-2.3	What do these concepts look like?
SUB-2.4	Which concept has the best performance?
SUB-3	Can the design of the SMSS feasibly be implemented within the DST?
SUB-3.1	What are the main system parameters?
SUB-3.2	Does the design meet all requirements?
SUB-3.3	Does the design have the desired functionality?

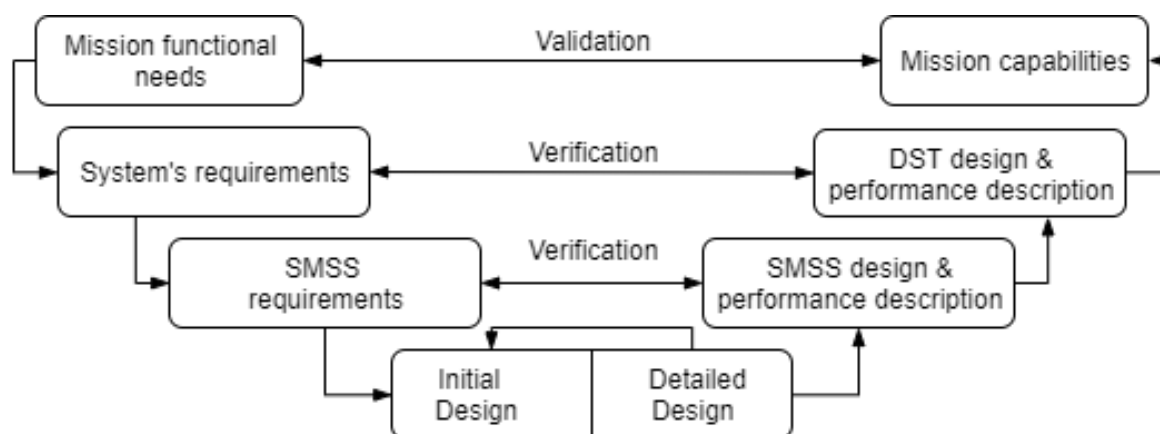


Figure 2.21: V-model systems engineering approach as used for the thesis. Adapted from Akkerhuis (2019).

resulting design choices. This check is followed by a full review of the DST system's requirements which are turned into requirements specifically for the SMSS. This part, as presented in section 3.1, thus aims to answer SUB-1 and represents the first three steps on the left-hand side of figure 2.21. Then, the actual design procedure is initiated. This initiation consists of the conceptual, or initial, design phase. Because initial designs of the DST and the SMSS were already defined in Krikken (2018), they are first reviewed in section 3.2 and only then refined in chapter 5. The result of this part is the answer to question SUB-2 and represents the left-most part of the bottom block in the V-model. The design phase is then concluded by the detailed design, as presented in chapter 6. Finally, the full system verification and validation procedure, representing the right-hand side of the V-model, is presented in chapter 7. Following the steps in the right-hand side of the V-model is an iterative process, in which the design is iterated if any of the requirements set in the verification and validation phases is not met. This process is recursively applied until a verified and validated design is found. The end result of following the V-model approach is the answer to the main research question and is presented in section 8.1.

3

Design Review

To ensure the end quality of this thesis design process is sufficient, the quality of the current design must be checked. The first step in the actual design process is, therefore, to verify whether the design choices and methods used so far are sound. If any faults are found, these can either be fixed immediately or noted down for future work. Firstly, in section 3.1, the mission and SMSS functionality and requirements are checked. Section 3.2 treats the design itself, ranging from the system-level design to the thermal and SMSS design. The design of the other subsystems, such as the optical systems, is not treated here, because this is out of the scope of this thesis work.

3.1. Functionality & Requirements

One of the first steps in a design process is to decide what the required functionality of the design and the corresponding requirements are. The requirements should ensure that the desired functionality of the telescope is met. Because these were already defined in previous work, the focus of this section lies on checking the required functionality and requirements.

3.1.1. Functionality

The main functionality of the DST is defined in MIS-OBJ-O1 and MIS-OBJ-O2 in table 2.2. The DST should have a GSD of at most 0.31 m. Furthermore, it should function for at least five years. The latter is, as of April 2020, not yet included within the list of mission requirements, so a new mission requirement regarding the lifetime of the telescope is added. In previous design iterations, up to and including Arink (2019), it was assumed that the telescope would operate in the visible spectrum. As of 2020, this might, however, change to an imager operating in the thermal infrared spectrum. It seems that there is an increasing interest from the Dutch military in low-cost Thermal Infra-Red (TIR) telescopes. To play into this market, it might be a good idea to change the scope of the project from a telescope operating in the visible spectrum to one operating in the TIR spectrum. As of January 2020, the decision is made that the design effort is still focussed on a telescope operating within the visible light. However, the design should be easily modifiable to one operating in the TIR spectrum. (Internal DST team meeting, 16 January 2020) This modifiability does have some implications on the design of the DST. Changing to a TIR telescope primarily affects the optical systems, but some system-wide effects are present. As TIR telescopes operate in the infrared spectrum, it is imperative that no random extra Infra-Red (IR) sources are present. This requirement is most stringent within the instrument housing but also holds outside of this environment. This means that high temperature variations within the baffle should be avoided, which in turn, for instance, means that no electrical heaters should be used. This functional requirement is further detailed in section 3.1.2.

The function of the SMSS is to deploy the secondary mirror to its desired position and keep it there within the specified budgets. Besides the need to not use heaters in the design, there are no immediate changes in functionality because of a change to a TIR telescope. The budgets regarding translation and rotation of the secondary mirror might be relaxed because of the change of telescope, but as the design effort is still focussed on a visible telescope, the budgets are, as of April 2020, not changed.

3.1.2. Requirements

Here, the newly defined and updated requirements are discussed. The full list of mission and SMSS requirements can be found in appendix A. The requirements should ensure that the required functionality of the SMSS is met. This means that requirements regarding the lifetime and modifiability of the system should be included. These requirements, as defined on 10 April 2020, with identifiers MIS-REQ-13 and MIS-REQ-14, can be seen in table 3.1. Furthermore, MIS-OBJ-02 specifies that the lifetime cost of the DST should not exceed USD \$850 million. This objective, however, not only quantifies an exact number that should be met, it even more so constitutes a design philosophy that should be followed in the design process. To make the DST competitive, a constellation of DST satellites with at least the same, but preferred better, functionality as the WorldView-4 satellite should cost less than the WorldView-4 satellite. To keep the cost of making multiple telescopes low, as required for a satellite constellation, simple, reproducible parts are preferably used. This is however seen as a design philosophy and is not added as a requirement.

Table 3.1: New DST mission requirements.

Identifier	Requirement
MIS-REQ-13	The DST shall have a lifetime of at least 5 years.
MIS-REQ-14	All technology used in the DST shall be usable both when a visible as well as a thermal infra-red telescope concept is chosen.

The requirements posed on the SMSS, as found in table A.2, should ensure that all mission requirements are met. This means that the newly defined mission requirements should also be included in the SMSS requirements. As of April 2020, the requirement with identifier M2-SYS-08, as seen in table 3.2, is added. Besides this new requirement, some earlier defined requirements are updated. Requirements M2-SYS-03 and M2-SYS-04, as defined in Krikken (2018), wrongly stipulated the volumetric requirements of the SMSS. As of April 2020, these requirements are changed. Firstly, M2-SYS-03 is changed such that the M2 mechanism in stowed configuration shall stay within the boundary box of the stowed baffle instead of the boundary box of the stowed primary mirror segments. M2-SYS-04 is changed such that there is no actual maximum stowed height of the M2 mechanism. MIS-REQ-08 stipulates that the volume of the telescope shall not, in any case, exceed 1.5 m^3 . This requirement was wrongly translated into a height requirement for the SMSS, whereas the combination of the baffle and SMSS should not exceed the maximum volume. The updated versions of M2-SYS-03 and M2-SYS-04 can be seen in table 3.2.

Table 3.2: New SMSS requirements.

Identifier	Requirement
M2-SYS-03	The SMSS in stowed configuration shall stay within the boundary box of the stowed baffle.
M2-SYS-04	The stowed SMSS and baffle shall combined not have a volume higher than 0.75 m^3 (goal)/ 1.5 m^3 (threshold).
M2-SYS-08	The lifetime of the SMSS shall be at least 5 years.

3.2. System level design

The system-level design of the SMSS is discussed here. Firstly, the mass and volume are discussed, followed by the drift of the secondary mirror.

3.2.1. Mass & Volume

The mass budget of the DST can be seen in table 3.3. The total mass of the telescope is, as of April 2020, 126.91 kg. The mass requirement of 100 kg (MIS-REQ-08) is therefore not yet met. This mass, however, does contain contingencies to allow for mass increases in the detailed design phase, which is

common practice in systems engineering. As the detailed design phase progresses, the contingencies will go down, and the final mass will become more accurate. This does, however, not necessarily mean that the mass will go down. However, for the purpose of this thesis, only the mass of the SMSS is relevant. The mass of the SMSS is estimated to be 11.88 kg. This mass is well below the current requirement of 14 kg (M2-SYS-01), so the requirement is met.

Table 3.3: Preliminary mass budget of the Deployable Space Telescope.

Component	Mass (kg)
Primary mirror	23.62
PM support structure	31.54
Secondary mirror	1.6
SM support structure	11.88
Tertiary & fold mirrors	2.4
Aberration correction system	9.48
Focal plane detectors	26.20
Instrument housing	6
Baffle	12.19
Harness	2
Total	126.91

The total stowed volume of the telescope is determined by the area of the baffle and the length by which the spider extends longitudinally from the base of the instrument housing. With the design as specified in Arink (2019) and Krikken (2018), the stowed area of the baffle bottom is 0.775 m^2 while the stowed spider extends 0.99 m above the bottom of the instrument housing. This gives the DST a stowed volume of 0.77 m^3 . The stowed volume requirement of 1.5 m^3 (MIS-REQ-08) threshold is therefore met. There is however another problem that has, as of April 2020, not yet been properly addressed. The baffle and the SMSS were designed separately without a clear understanding of how the other component would work and what the exact geometry of both structures was. This misunderstanding led to the design of two parts which would, if the other one was not present, work fine. However, as both are present, they do not. There is simply no space for both parts, as is illustrated in figure 3.1. To limit the total length of the stowed telescope, both parts of the booms should be as much parallel to the instrument housing sides as possible, as indicated as mode A in the figure. However, in this mode the booms extend beneath the bottom of the instrument housing, thus physically intersecting with the baffle. Mode B shows the geometry of the SMSS that is necessary for the booms to not extend beyond the bottom of the instrument housing. In this mode, however, the SMSS intersects with the side of the baffle. This issue will be addressed in the thesis work of Nagy, who is working on a redesign of the baffle.

3.2.2. Secondary mirror drift

The baffle provides the telescope with a relatively stable thermal environment; however, some temperature fluctuations are still present. The temperatures variations of the components over the telescope's orbit, as found in Arink (2019), can be seen in table 3.4. The temperature values for the root CORE hinge and the SM interface rods could not be retrieved, as they were not reported and are thus still To Be Determined (TBD). Although not all temperature variations could be retrieved, the order of magnitude of the in-orbit translation of the secondary mirror can already be calculated and directly follows from the temperature variation of the booms and rods by applying linear expansion to the different components. The maximum translation in longitudinal (Z) direction is equal to $2.6 \mu\text{m}$ while the maximum rotation around the X- and Y-axis is equal to $2.6 \mu\text{rad}$ [4]. Referring back to table 2.4, the maximum in-orbit drift in longitudinal direction is $2 \mu\text{m}$ and the maximum in orbit drift in rotation around the Xi and Y-axis is $6 \mu\text{rad}$. This means that the in-orbit drift budget in longitudinal direction is not yet met.

The temperatures as reported in Arink (2019) do leave some doubt though. While some components, such as the top CORE hinges, do have significant temperature swings, others barely vary at all.

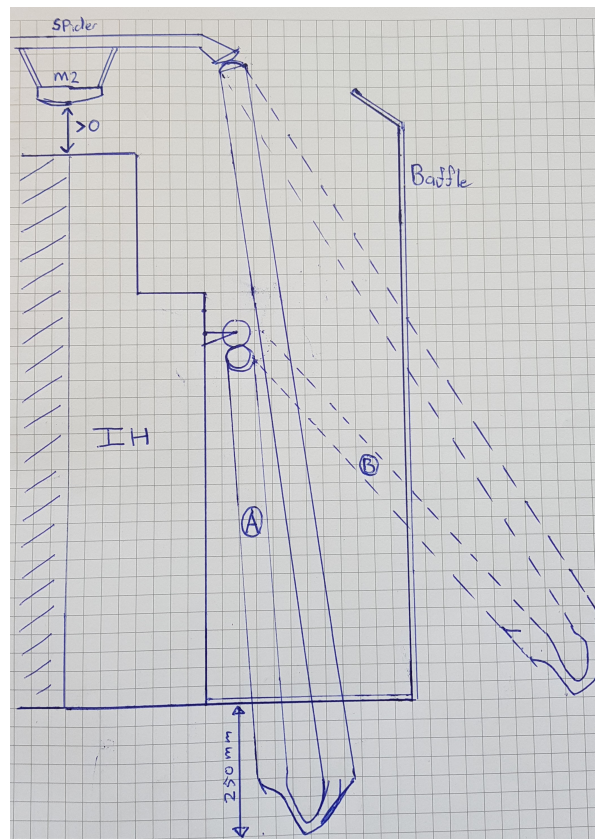


Figure 3.1: Schematic overview of two stowed configurations of the DST. On the left the instrument housing (IH) is shown, on which two possible configurations of the booms (A and B) are attached. The baffle is shown attached to the bottom of the IH.

Table 3.4: Nominal temperature budget of the Deployable Space Telescope. Adapted from Arink (2019).

Component	Maximum temperature (K)	Minimum temperature (K)
Secondary mirror	14.2	14
Spider	2.8	0.2
Primary mirror support structure	8.7	6.1
Top CORE hinge	12.8	0.0
Root CORE hinge	TBD	TBD
Deployable booms	6.8	4.5
SM interface rods	TBD	TBD

To verify the temperature profile of the different components and to find the missing temperature values, an in-depth analysis of the thermal model as used previously is in place. This is done in section 3.3.

3.3. Verifying the thermal model

A thermal model of the DST was first created by van Hees[27] and later refined by Arink[4], who also designed a baffle to shield the telescope from solar radiation. The model was made using ESATAN TMS. The process of verifying the model consisted of first checking whether the theories and methods used in Arink (2019) were sound and then by systematically checking the geometry and parameters of all components in the thermal model with reference values.

3.3.1. Rationale check

Some of the main relevant results from Arink (2019) are that the baffle consists of five layers of MLI, that the inside of the baffle and all parts of the SMSS are coated by MagicBlack coating and that the outside

of the baffle is coated by a SiOx/VDA/Kapton layer. The use of MagicBlack coating is easily justifiable, as stray light within the baffle needs to be minimised. For this reason, the absorptivity and emissivity need to be as high as possible, which is exactly what MagicBlack offers. To block out radiation from the Sun, the outer coating should preferably have low values for absorptivity and emissivity. Furthermore, the ratio $\frac{\alpha}{\epsilon}$ should be between 1 and 3 and as close as possible to 2 to keep the temperature of the telescope higher than -20 K and lower than 50 K. A SiOx/VDA/Kapton coating with $\frac{\alpha}{\epsilon} = \frac{0.19}{0.14}$ does indeed provide these characteristics and is therefore a good choice.

Because the in-orbit drift budget was not met using only the baffle, Arink proposes the use of heaters within the baffle sides to create a very stable thermal environment throughout the telescope's orbit. However, these proposed heaters can easily be discarded. A first-order analysis shows that the added mass alone would already be unacceptable. Because the heaters would mainly be used in eclipse, batteries would also have to provide the energy. During its orbit, the telescope is in eclipse for around 2100 seconds[4], meaning the amount of energy required would be $8 * 287W * 2100/3600hr \approx 1,400Whr$. Because the eclipse is just shorter than the time not in sunlight, and taking in account charging losses, the solar array power requirement is about as high. Pidgeon and Tsao (1991) gives relations for the power required and the solar array and battery masses. Looking at the end of life requirements, an optimistic value for both masses would be about 40 kg, thus adding about 80 kg to the satellite. Even if the added complexity of such a system is not taken into account, adding this amount of mass would be too much of a strain on the system. It can therefore safely be said that using heaters within the baffle to provide a stable thermal environment for the telescope is not a viable option.

The baffle consists of five layers of MLI. Of course, adding more layers of MLI reduces the amount of heat that passes through the baffle and thus increases the thermal stability within the baffle, which would make more layers desirable. However, in stowed configuration, the baffle needs to be folded. This means that there is a maximum amount of layers that can be used. Arink (2019) reports that the ratio between the amount of layers (N) squared and the radius of curvature (ρ_c) shall not exceed $\frac{N^2}{\rho_c} = 1.58$. The relationships reported are well understood, and the argumentation used by Arink is sound. It can, therefore, be assumed that the reported maximum of five layers is correct. Arink calculates the heat flow through the baffle using the Doenecke method[29]. This method is well understood and widely used and is, therefore, a suitable way of calculating the heat flow.

3.3.2. ESATAN model

The systematic check of the ESATAN model unearthed the following mistakes:

1. The mirrors were modelled as solid parts consisting entirely of Silicon Carbide. In reality, however, the mirrors are optimised to get a mass as low as possible. This is done by creating cut-outs at the backside of the mirror. By modelling the mirrors as solids, their mass is too high, which in turn means the thermal inertia of the mirrors is too high. This has the effect that more energy is required to heat the mirrors, which thus removes heat from other parts of the system and effectively dampens the temperature variation of the entire DST. Furthermore, because they were modelled as solids, their thermal conductivity is too high.
2. Both the primary mirror support structure and the spider were modelled as solid CFRP beams. In reality, they are thin-walled beams. As for the mirrors, this means that the mass, thermal inertia and conductivity values are too high.

Furthermore, the geometry of the PMSS and spider were incorrect. The PMSS, for instance, which consists of several interconnected beams, was modelled such that these beams did not correctly connect. Because of this, ESATAN did not recognise which geometric parts are in contact and with what area. Without this information, the amount of conductivity between these parts is not correctly calculated.

3. In places, the real geometry is too complex to be accurately modelled within ESATAN. An excel-

lent example of this is the geometry of the CORE hinges. They consist of multiple round cylinders which are connected by means of thin strips. In cases like this, a simplification of the geometry with roughly the right shape is in order. With such simplifications, however, it is not always possible to interconnect the different parts, and thus ESATAN does not calculate the heat flow by conduction between these parts. In these cases, separate hand calculated conductivity values should be specified between the different parts.

4. The baffle consists of five layers of MLI. In ESATAN, this can be modelled by creating a hollow shell with an effective heat flow between the in- and outside of the baffle. This effective heat flow can be estimated by specifying either an effective conductance or an effective emissivity. In the model, both values were erroneously used in cohesion, whereas only one of them should be specified. Using both gives too high values for the heat flow.
5. For most parts, making a rough estimate of the shape is sufficient; however, this is not the case for the primary mirror. In reality, the primary mirror is curved such that almost all incoming radiation from Earth is focussed on the secondary mirror. From there on, it is reflected towards the field stop and into the instrument housing. However, in ESATAN the mirrors are modelled as rectangles. This means that the radiation is not reflected correctly and thus impinges surfaces which it should not, thereby heating these surfaces.
6. The deployable booms were modelled as thin-walled cylinders with a thickness of 5 mm. In reality, they are 0.5 mm thick. This wrong thickness greatly increases their thermal inertia and thus decreases the amount by which their temperature varies. Furthermore, the material properties of CFRP were wrong. Mainly the thermal conductivity was wrongly specified to be 180 J/m.K. Arink (2019) uses Ting et al. (1998) as his source. This article, however, discusses a carbon fibre reinforced aluminium matrix and not a carbon fibre reinforced polymer. As stated in Krikken (2018), the CFRP matrix required for the boom hinges is specifically created to allow for the required range of motion. It can therefore safely be stated that the composite used for the booms is a CFRP.
7. The Earth's albedo and temperature were assumed to be constant. In reality, they vary over the surface of the Earth and over the time of year.

The process of fixing the aforementioned problems is treated in chapter 4

4

Thermal model

This chapter discusses how the problems in the thermal model, as reported in section 3.3, are solved. Firstly, a general background on the calculations to be performed is presented in section 4.1. This is followed by the actual solutions to the problem in section 4.2. In section 4.4, the new temperature results as found by running ESATAN are presented. The inputs used in the thermal model can be found in table B.1.

4.1. Thermal background

ESATAN is a potent program that allows the calculation of the temperature profile of the different components within satellites. It does so by calculating the heat balance of every node at every time-step and uses this to calculate the temperature at the next time-step. However, for it to do so, the radiative and conductive couplings between components need to be known. ESATAN itself calculates the radiative couplings with a Monte-Carlo ray-tracing method. The conductive couplings, however, are a different story. When components intersect with one another in the geometric model, a conductive interface is created which uses a conductance to calculate the conduction. When components are too complex to accurately model in ESATAN, and as such do not touch one another, a user-defined conductor can be specified. The way to calculate such conductor values is explained in section 4.1.1. ESATAN allows geometries to be modelled as thin shells with an in- and outside wall. The conduction between these walls can be entered as effective conductance or emittance values, which can be calculated using the Doenecke method, as shown in section 4.1.2.

4.1.1. Conduction

Conduction between components is one of the main ways of heat flow in a satellite. In the case of the DST, complex conductive paths run for instance through the CORE hinges and from the spider to the secondary mirror. The way to calculate the heat flow (Q_{ij}) from component i to j is shown in equation (4.1).

$$Q_{ij} = C_{ij}(T_i - T_j) \quad (4.1)$$

Here, C_{ij} is the conductive coupling between the two components. The conductive coupling through a part can be calculated as in equation (4.2a), where k is the conductivity of a material, A the cross sectional area and L the length of the conductive path. The conductive coupling between two parts is calculated as shown in equation (4.2b), where h_c is the conductance between both surfaces.

$$C_{ij} = kA/L \quad (4.2a)$$

$$C_{ij} = h_c A \quad (4.2b)$$

The conductivity of different materials is widely known and can easily be found. However, the conductance between different surfaces depends on a lot of factors, such as surface roughness, applied pressure and the presence of intermittent material. The conductance between materials can thus be

varied according to different needs. Empirical relationships are for instance found in Gilmore (2002) and Karam (1998). Widely used methods of increasing the conductance values include the use of greases, gaskets and silicon compounds. Of these three, Room-Temperature-Vulcanized (RTV) compounds are the most widely used within space applications because greases and gaskets have some shortcomings. Greases are inherently volatile. This means that in the vacuum of space, they have outgassing problems, which makes it hard to keep them in place. Gaskets are solid materials which are compressed between the two parts. Because of this compression, they fill up the voids in the materials. The pressure required is, however high, which creates structural loads and can cause bending of the mounting plates. This bending, in turn, reduces the thermal conductance between the plates. RTV interfaces are solidly cured-in-place, meaning that they do not outgas as much as greases and provide near-continuous contact without the need for high applied pressures. They are furthermore simple to implement and provide good thermal conductance.[31] Figure 4.1 provides an overview of the contact conductance over the number of bolts per area, which is analogous to the applied pressure between the plates, when an RTV interface is used and when there is no interstitial material. The graph shows that the conductance goes up to a maximum of around 480 W/m².K with a higher number of bolts per area and down to a conductance of around 150 W/m².K. The values reported are valid for a plate thickness of around 2.5 mm. For thin plates, the values scale approximately linearly with the relative thickness.[31]

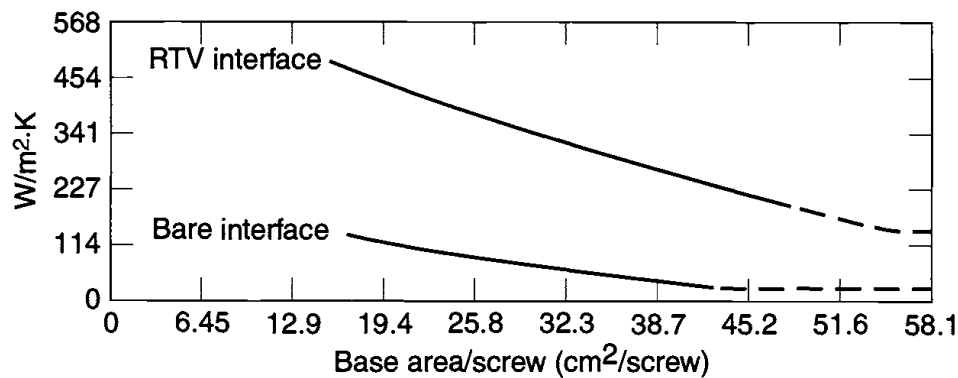


Figure 4.1: Contact conductance across a mounting interface with and without RTV filler. Adapted from Gilmore (2002).

Complex geometries often have multiple conductive paths in series and parallel. When these paths are placed in parallel, the different conductive couplings can be summed up using equation (4.3a). When the couplings are placed in series, equation (4.3b) is used. Complex thermal couplings between parts can consist of any number of series and parallel connections in which the equations (4.3a) and (4.3b) can simply be repeated.

$$C_{p,12} = \sum C_i \quad (4.3a)$$

$$C_{s,12} = \frac{1}{\sum \frac{1}{C_i}} \quad (4.3b)$$

4.1.2. Doenecke method

The heat flow through the baffle is calculated by using the empirical relations as presented in Doenecke (1993). By analysing measured blanket performance from many sources, the equations as presented in equation (4.4) were developed. They are widely used and accepted as a good initial estimation of the heat flow through MLI layers.[29, 31, 32] The calculated values do however have a big uncertainty, typically of around 25%[33], which has to be taken into account in the design procedure. It is therefore critical that the values are verified experimentally. The heat flow through the baffle can be represented by either an effective emittance (ϵ_{eff}) or an effective conductance h_{eff} interchangeably, according to the engineers preference[29]. The effective emittance is calculated as

seen in equation (4.4). Here, the coefficients f_N , f_P and f_A respectively represent the number of layers (N), the fraction of perforations through the layers (P) and the exposed blanket area (A).

$$\epsilon_{eff} = \left(1.36 \cdot 10^{-4} \frac{1}{4\sigma T_m^2} + 1.21 \cdot 10^{-4} T_m^{2/3} \right) f_N f_A f_P \quad (4.4a)$$

$$f_N = 4.5465N^{-0.501} \quad (4.4b)$$

$$f_P = 0.2685P + 0.73 \quad (4.4c)$$

$$f_A = 0.1^{0.373 \log_{10} A} \text{ for } 0.04m^2 \leq A \leq 3m^2 \quad (4.4d)$$

Here, T_m is the mean temperature of all MLI layers and is calculated as seen in equation (4.5).

$$4T_m^3 = \frac{T_h^4 - T_c^4}{T_h - T_c} = (T_h^2 + T_c^2)(T_h + T_c) \quad (4.5)$$

The effective emittance can be related to the effective conductance through equation (4.6), where σ is the Stefan-Boltzmann constant.

$$h_{eff} = 4\epsilon_{eff}\sigma T_m^3 \quad (4.6)$$

The effective conductance is thus highly dependant on the mean temperature of the MLI layers. However, to calculate the mean temperature of the MLI, the in- and outside temperature have to be known. These are again dependant on the effective conductance. Finding the correct effective conductance is, therefore, an iterative process. This process starts with a guess of the mean temperature, by which the effective conductance is calculated. This effective conductance is then used to calculate the actual temperatures by which an updated effective conductance can be calculated. This process is repeated until the required accuracy is achieved.

4.2. Problem solving

In this section, the problems as identified in section 3.3 are resolved, in the same order as they were presented.

4.2.1. Mirrors

The mirrors are no solid slabs, as can be seen in figure 4.2, but rather hollow structures. The many cut-outs are, however, hard and time-consuming to model within ESATAN. A useful approximation of the mirrors is made by modelling them as two separate parts. The first being the top layer with the real density and conductivity and the second being the rest of the mirror with an effective density and thermal conductivity. Combined, the mass of these layers should equal the total mass of the mirror. Using an effective thermal conductivity is, of course, not a perfect representation of reality because the heat flow through the cut-outs does not flow perfectly linear. However, as a first-order approximation, it should be sufficient.

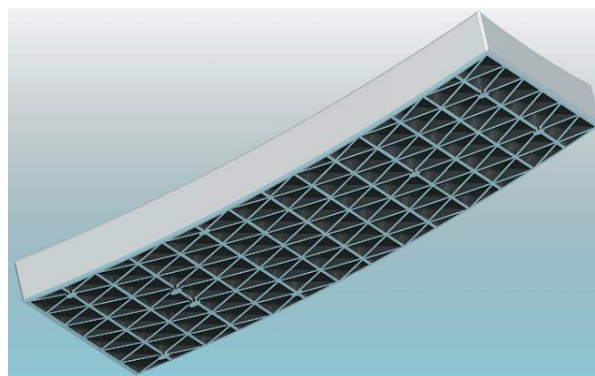


Figure 4.2: Lightweighted mirror segment. As retrieved from Dolkens (2015).

The masses of the primary and secondary mirror respectively are 5.906 and 1.01 kg. The density (ρ) of the used Silicon Carbide is 3150 kg/m^3 and the thermal conductivity is 142 W/m.K . Both mirrors are assumed to have a thin top layer of 1 mm. The resulting effective density and thermal conductivity of both mirrors is given in table 4.1.

Table 4.1: Density and effective density of primary and secondary mirror.

	Effective density [kg/m^3]	Effective thermal conductivity [J/m.K]
Primary mirror	397.0	17.9
Secondary mirror	871.9	191.0

4.2.2. Primary mirror support structure and spider

ESATAN allows for the creation of shell structures, meaning it allows for the creation of hollow beams. There is, however, an issue in creating complex geometries with shell structures in ESATAN. Because ESATAN cannot calculate the contact area between shell structures, the conductance between the different touching elements can also not be calculated. For this reason, it is preferable to create these geometries using solid beams, because ESATAN can calculate the contact surface area between different solid parts. Creating the PMSS and spider using solid parts is similar to the process followed for the primary and secondary mirror. Effective values for the density and thermal conductivity of the parts should be calculated such that they represent the real structure. Again, of course, the effective conductivity does not perfectly represent the real world. However, modelling it this way is preferable over using shell structures, as inter-part conduction is essential in calculating the heat flow through the structure.

4.2.3. Conduction between parts

The conductive couplings between parts are calculated using the equations and relations described in section 4.1.1. Because the conductivity of parts and conductance between parts highly varies per interface, they are treated separately per part. Furthermore, for most parts, the final design is not yet specified (as of the design iteration by Arink (2019)), and thus the way in which these parts are connected is not detailed. For these parts, assumptions are made based on what type of connection (highly versus lowly conductive) they require. The values found here are prone to change in future design iterations, because the actual connection and production methods are not known yet. Furthermore, a sensitivity analysis, as performed in section 4.3, shows to what extent any variations in the conductive values influences the thermal profile of the DST and thus whether a more detailed design of the conductive paths is necessary. A list of the calculated conductive values is presented in table B.2.

Conduction between deployable booms and CORE hinges

The CORE hinges are connected to the booms via the boom endcap. An overview of the endcap and part of the boom can be seen in figure 4.3. The conduction from the booms to the top and root CORE hinges happens via two pathways. The first path runs to the inside of the cylindrical part (ring) of the cap and the second path to the bottom side of the top plate of the cap. Mirmira et al. (2001) provides experimental data on the conductance of CFRP to other materials. Because the exact lay-up and composition of the material are not known, average values are used. The average conductance ranges from 300 to $600 \text{ W/m}^2.\text{K}$ over the range from 200 to 2000 kPa interface pressure. The boom is assumed to be clamped in place meaning the applied pressure between the ring and boom is high, whereas that between the plate and boom is low because there is no force holding the plate down. The conductance between the ring and the boom is therefore assumed to be $600 \text{ W/m}^2.\text{K}$, whereas the conductance between the plate and boom is assumed to be $300 \text{ W/m}^2.\text{K}$. The interface area of the inside of the cylindrical part is 43.9 cm^2 and that of the top plate 4.3 cm^2 . The total conductive coupling between the booms and caps is then equal to $600 \cdot 43.9 + 300 \cdot 4.3 = 2.77 \text{ W/K}$.

Conduction through CORE hinges

The conduction between both CORE hinge halves, as seen in figure 4.4, happens through several paths. Firstly, the CORE halves physically touch on four points, as indicated by the blue lines, where

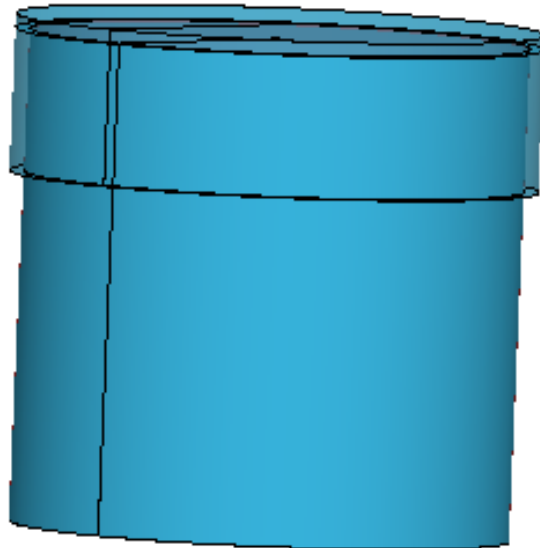


Figure 4.3: Endcap of the deployable booms.

they rotate around each other. Secondly, conduction happens through the three strips, indicated by the red arrows in figure 4.4. These strips are attached to both halves on the areas shown in green.

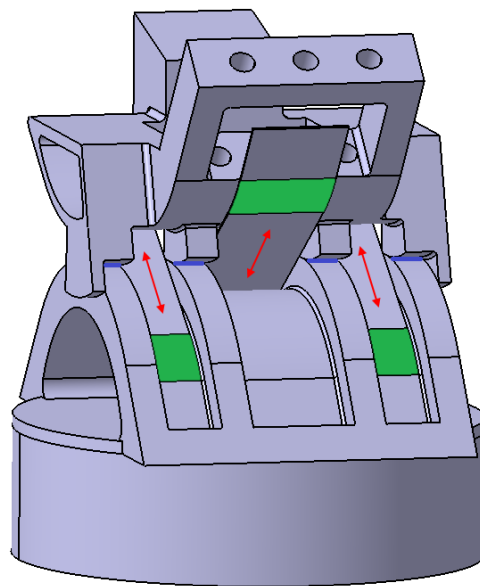


Figure 4.4: Top CORE hinge.

The strips and CORE halves are made of a titanium alloy, namely Ti-6Al-4V with a conductivity of 7.2 W/m.K [31]. Because the strips are pre-tensioned, the interfaces between the strips and CORE halves are under high pressure ($\approx 100 \text{ MPa}$ [3]). From Lambert et al. (2006) a contact conductance of at least 10^4 is found to be realistic for such high pressures. The conductive coupling between the touching halves ($C_{touching,halves}$) is easily found by applying equation (4.2b). The coupling through the strips is more complicated. It consists of three couplings placed in series, namely through the interfaces between the strip and the two halves and through the strip itself. To find the coupling through the strips, equation (4.2a) is used twice where the strips attach to the bottom and top CORE halves and equation (4.2b) is used once. They are then combined using equation (4.3b). Finally, all seven couplings are summed to calculate the total conductive coupling (C_{CORE}), as seen in equation (4.7).

The second term contains all three strips, but because the middle strip is twice the size of the outer strips, the second term is increased to four times the coupling through the outer strips. The root and top CORE hinges both have conductive couplings of 0.20 W/K.

$$C_{CORE} = 4 \cdot C_{touching,halves} + \frac{4}{2/C_{CORE,strip} + 1/C_{strip}} \quad (4.7)$$

Conduction from CORE hinge to spider

The CORE hinges are connected to the spider via endcaps placed on the spider tips. The endcaps are clamped and held in place by bolts, thus providing a high pressure. The contact conductance is found to be 600 W/m².K[34]. The total interface area between the endcap and the spider is 14.76 cm², making the conductive coupling 0.89 W/K.

Conduction from spider to rods

The temperature variation in the rods is crucial to counter the elongation of the booms. As the rods are placed mainly in the shadow of other parts, it is crucial that the rods closely follow the temperature of the spider. The conductive coupling, therefore, needs to be as high as possible. Gilmore (2002) reports conductance values up to 15,000 W/m².K can be reached by using RTV compounds on small stiff surfaces. Such high conductances are, however, found with very high applied pressures which are hard to achieve with lightweight structures. Still, a moderately high conductance of 5,000 W/m².K is assumed. With a total interface area of 2.36 cm², the conductive coupling is equal to 2.36 W/K.

Conduction from rods to secondary mirror

Contrary to the conductive coupling between the spider and rods, the coupling between the rods and secondary mirror ought to be as low as possible. This allows for decreasing the heat flow from the rods to the mirror. Gilmore (2002) reports conductance values down to about 10 W/m².K can easily be reached by implementing interstitial materials with very low conductivity. With the same total interface area of 2.36 cm², the conductive coupling is equal to 2.36 mW/K.

Conduction from CORE hinge to instrument housing

The coupling between the root CORE hinges and the instrument housing exists of two couplings in series. First, the hinge is connected to a plate, shown in blue in figure 4.5, through six titanium connection beams, shown in green. This plate is attached to the instrument housing, indicated by the red line, by means of four bolts. The beams are fused with the hinge and the plate, so no interface conductance between the beams and plate is present. The coupling through the beams is easily found by using the conductivity of titanium and the length and area of the beams. The plate has an area of 60 cm², meaning the base area per screw is around 15 cm²/screw. Then, from figure 4.1, a conductance of 114 W/m².K is found for a bare interface. However, the plate is 5 mm thick, meaning that the conductance is scaled by 5/2.5, which then equals 228 W/m².K. The total conductive coupling is found to be 0.016 W/K.

Conduction instrument housing to PMSS

The PMSS is supported by a cylindrical bar over which it rotates during deployment. The heat flows from the PMSS to these bars, then through four connection pieces to a baseplate and finally into the instrument housing. These couplings are calculated separately and then added in a series connection. Even though lubrication is required during deployment, this is not required during normal operation. It can therefore be assumed that, even when lubrication is applied, no special precautions are taken to prevent the evaporation of this lubrication over time. Kannel and Dufrane (1986) reports evaporation rates down to 0.0002 mg/cm².hr. This means that, without precautions, a lubrication layer of 1 mm thick would evaporate within 800 hours. It can therefore be said that after a certain period, all lubrication will have evaporated and thus that during normal operation no lubricant is present. Therefore, the conductance values of bare material, as seen in figure 4.1, are used. For a bare interface with a high surface and low number of bolts, the conductance goes down to about 23 W/m².K. The support is made of CFRP with a conductivity of 7 W/m.K. The total conductive coupling is found to be 0.014 W/K.

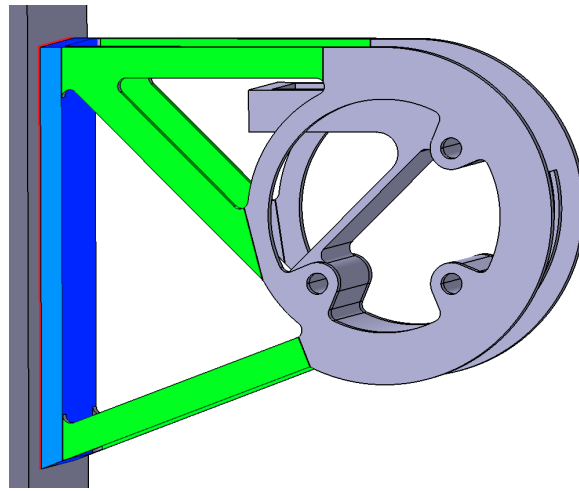


Figure 4.5: Attachment of root CORE hinge to instrument housing.

Conduction from PMSS to primary mirror

The primary mirror is supported by three main struts, which are made of titanium with a conductivity of $7.2 \text{ W/m}\cdot\text{K}$. To prevent heat flow into the primary mirror, a low conductance material ($10 \text{ W/m}^2\cdot\text{K}$) is used as interface between the struts and the primary mirror. The interface between the PMSS and the struts is taken to be that of a bare stiff interface, for which Mirmira et al. (2001) states a conductance of $600 \text{ W/m}^2\cdot\text{K}$. The total conductive coupling is found by placing the three couplings in series and equals 4.8 mw/K .

4.2.4. baffle

As explained in section 4.1.2, the heat flow through the baffle can be approximated by calculating an effective conductivity, as calculated by equation (4.6). To calculate the effective conductivity, firstly the constants f_N , f_P and f_A need to be found. f_N is found by inserting the number of layers (5) in equation (4.4b), and is equal to 2.03. f_A is calculated using equation (4.4d) and differs over the different baffle segments. The baffle consists of eight square segments with an area of 2.08 m^2 on all sides and eight triangular segments with an area of 0.35 m^2 on the bottom. Both areas lie between 0.04 and 3 m^2 , so equation (4.4d) is used. The f_A values found for the side bottom segments are respectively 0.76 and 1.48. The amount of penetration is typically around 1%, for which Gilmore (2002) reports a P value of 1, making f_P 0.9985 for all segments.

With all constants known, an initial estimate of the effective conductivity is required to calculate the first iteration of the mean temperatures throughout the orbit. For this, a value for h_{eff} of $0.1097 \text{ W/m}\cdot\text{K}$ as reported by Arink (2019) is used. Even though this value not very accurate, it is sufficient to find the first iteration of mean temperatures. These temperatures are found by implementing the initial estimate of h_{eff} in ESATAN and running the thermal analysis. The analysis results in out- and inside temperatures for each baffle segment over 20 different positions in the telescope's orbit. It is found that the temperatures of the eight bottom baffle segments are nearly identical, with a variation of about 0.5 K , while the temperatures of the eight side baffle segments vary greatly. This makes sense, since all bottom segments have the same orientation while the side segments all have different orientations. It is therefore assumed that the bottom segments have the same temperatures and thus the same h_{eff} , while all side segments have different temperatures and thus different h_{eff} . The temperatures are exported and used to calculate the h_{eff} per segment per time step. These h_{eff} values are then again imported into ESATAN to find the new temperature values and so on. After three iterations the values of h_{eff} only changed by less than 0.1% , sufficiently low to use these values in further calculations. The full list of conductance values is found in appendix B.

4.2.5. Primary mirror shape

The primary and secondary mirrors have a coating with an emissivity and absorptance of 0.035. This means only 3.5 % of the incoming radiation directly impinging on the primary mirror is turned into heat in the primary mirror. Assuming all radiation reflected by the primary mirror reaches the secondary mirror, 3.4 % ($0.035 * 0.965$) of the total incoming radiation is absorbed by the secondary mirror. This means that 93 % ($0.965 * 0.965$) of the total incoming radiation is reflected off of the secondary mirror towards the field stop. Here, about half of the incoming radiation is blocked by the field stop, where it is turned into heat, and the other half enters the instrument housing where the sensors capture it and eventually turned into heat. This means that 46.5 % of the total incoming radiation is turned into heat in the field stop and about 46.5 inside of the instrument housing.

This system can be represented by applying heaters and coolers on the different parts. Firstly, by giving the primary mirror an emissivity and absorptivity of 1, it is ensured that all incoming radiation is absorbed by the primary mirror segments. The power values of the incoming radiation throughout the telescope's orbit can be retrieved from ESATAN. By then again removing 96.5 % of said power from the primary mirror, it effectively absorbs 3.5% of the incoming radiation. The secondary mirror, field stop and sensors can then be heated by their respective power inputs. By using this representation of reality, it is ensured that heat is applied on the right surfaces and not randomly distributed within the baffle.

4.2.6. Value errors

The boom wall thickness was changed to 0.5 mm. The conductivity of CFRP is found to range from around 2 to 20 with the median around 7 in-plane[37, 38] and from around 0.2 to 1.0 with the median around 0.8 out-of-plane[37–40]. Because the exact lay-up and composition of the different CFRP components within the DST is, as of the design presented in Krikken (2018), not yet known, the median values of 0.8 and 7 are used.

4.2.7. Earth Albedo and temperature

Data on Earth's Albedo and surface temperature is freely available on NASA's Clouds and Earth Radiant Energy System (CERES) website up to a resolution of 1 degree. For the purpose of this study, such a high resolution is neither necessary nor easy to implement. A simple solution lies in either representing the data by averaged values over the Earth's latitude or longitude. Using a latitudinally organised dataset is then the most logical because the highest variation in both Albedo and surface temperature is found going from the equator to both poles. Furthermore, the data is not as much obscured by the day-night cycle as the longitudinal dataset is. Peyrou-Lauga (2017) organises effective (where effective means the real perceived, or measured data) Albedo and temperature data found on the CERES website[42] into monthly averages and a 5-year average. The averages are based on measurements taken from 2007 up to and including 2011. The data used in the ESATAN model can be found in table 4.2. Note that the average, as indicated on the bottom of the table, is the weighted average of the above values. Because the area of the slabs near the equator form up a bigger part of the Earth's surface than the slabs near the poles they have a bigger impact on the weighted average. A sensitivity analysis, as performed in section 4.3, shows the effect of only using the yearly average versus making separate thermal cases for every month.

4.3. Verifying the model

Before the results can be used in the design procedure, they need to be verified. Firstly, in section 4.3.1, the temperature profiles are checked by comparing them to analytically calculated temperatures. Then, in section 4.3.2 the sensitivity of the temperatures to the different assumptions made is checked, and conclusions are drawn.

4.3.1. Analytic relations

The calculations within ESATAN are mainly twofold. Firstly, the radiative case calculates the radiative exchange factors between the different nodes of the model. Secondly, the thermal case calculates the temperature of all nodes by finding the heat exchange between the different nodes and using the material properties. The radiative case calculations depend solely on the shape of the components, the

Table 4.2: Earth perceived Albedo and temperature by latitude. Retrieved from Peyrou-Lauga (2017).

Latitude [°]	Albedo [-]	Temperature [K]
85	0.59	242
75	0.55	243
65	0.49	245
55	0.42	248
45	0.36	252
35	0.30	256
25	0.25	262
15	0.22	262
5	0.24	256
-5	0.22	258
-15	0.22	262
-25	0.23	261
-35	0.28	257
-45	0.36	251
-55	0.44	246
-65	0.57	241
-75	0.68	233
-85	0.69	228
Average	0.31	255

applied coatings and the relative orientation of all components. The implementation within the model can be verified visually by checking the shape and applied coating of the different components, as is shown in figure 4.6. Analytic relations for the radiative exchange factors do exist, but implementing these relations for complex geometries is hard and time-consuming. However, showing that the exchange factors are accurate for simple geometries provides confidence for the accuracy of ESATAN for more complex shapes. Such a comparison was done in Arink (2019), where the radiative factors were analytically calculated for a simple baffle geometry. An ESATAN model showed good resemblance, thus providing the required confidence to use the radiative calculations of ESATAN.

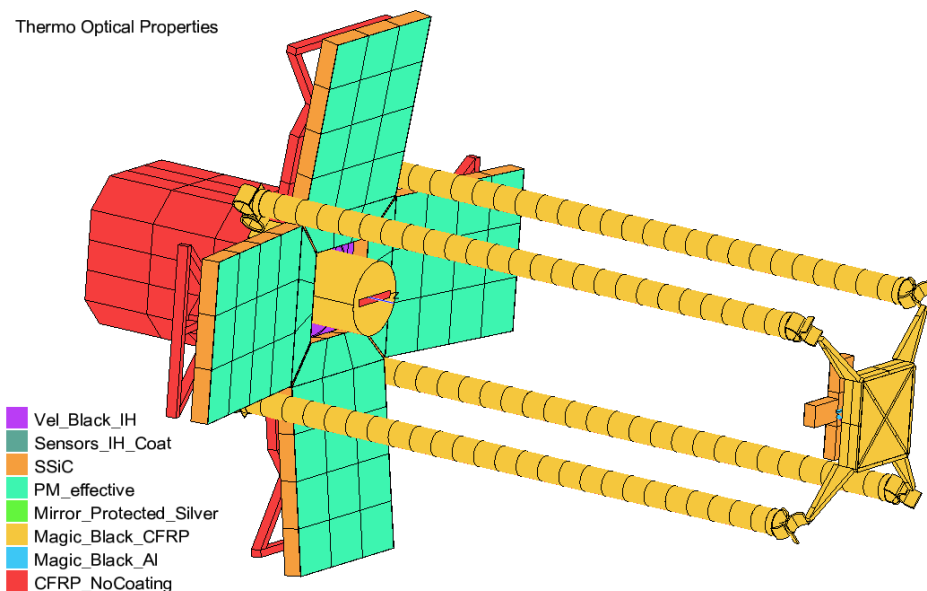


Figure 4.6: Visual inspection of the model as performed within ESATAN.

The thermal case calculates the heat exchange between different nodes at every time step. This

heat exchange is based on the radiative exchange factors, the conductive heat exchange and the current node temperatures. The conductive heat exchange between different components is determined as described in section 4.2.3. There is a significant amount of uncertainty in the determined values, for which a sensitivity analysis is performed in section 4.3.2. The temperature for the next timestep (T_{i+1}) is, roughly, calculated by equation (4.8). Here, ΔQ is the heat input, m the mass and c_p the heat capacity of the material. Together, the mass and heat capacity is called the thermal mass and defines for a large part the rate of temperature change of a component. The thermal mass of all components is known, so the temperature profile of a component can be calculated when the heat input is known. Now, ESATAN implements an iterative solver in which the temperature results and the heat input are iterated over several cycles to arrive at an accurate prediction of the temperature. If the final temperature profile can be shown to be accurate, the results of the thermal solver are deemed verified.

$$T_{i+1} = T_i + \left(\frac{\Delta Q}{mc_p} \right) \Delta t \quad (4.8)$$

To calculate the temperature profile of a node, the initial temperature and the heat input over the orbit are needed. These can both be exported from ESATAN. Then, using equation (4.8), the temperature profiles of the booms and rods can be seen in figures 4.7a and 4.7b. The analytically and numerically calculated temperature profiles of the booms show good convergence, whereas the temperature profiles of the rods are far apart. The shape is the same, but the calculated temperature range is much higher. This difference can point towards two things, namely that ESATAN wrongly calculates the heat input or the thermal mass.

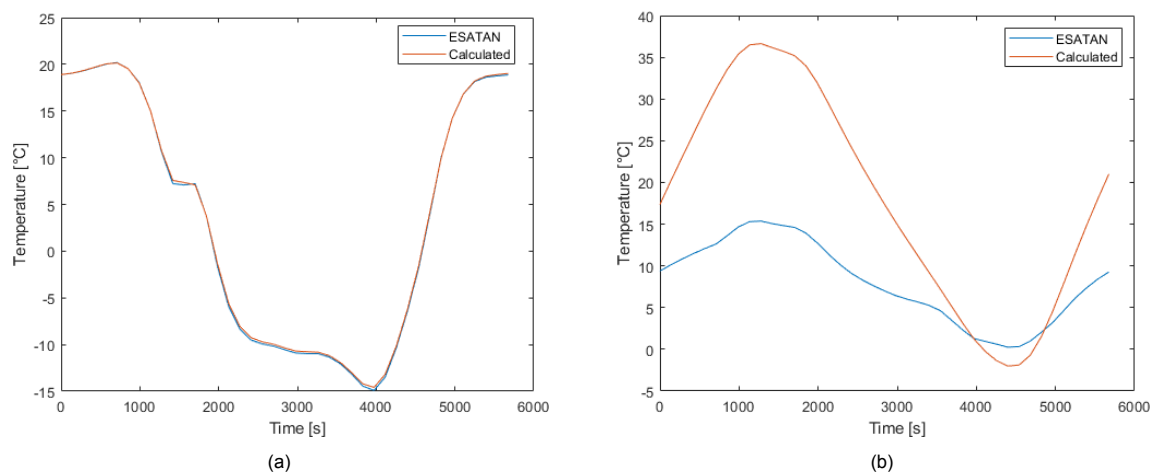


Figure 4.7: Analytic and simulation temperature results of a) the booms and b) the rods.

The mismatch between the analytically and numerically calculated temperature profile is shown in figure 4.8 by the purple and yellow lines. It was found that the erroneous calculations by ESATAN were caused by the fact that the rods were modelled as solids. The problem arises because ESATAN was initially only intended to be used with thin-walled structures. The feature allowing solid parts to be modelled was only added in recent years and mostly intended for small scale solid parts with very fine meshes (personal communication, N. van der Pas, 13 May 2020). Too coarse meshes cause the heat exchange between the rods and other parts to be calculated erroneously. Increasing the mesh solves the problem, but this requires such fine meshes that the calculation time increases unreasonably. The rods were therefore changed from being modelled as solid parts to thin-walled parts. However, ESATAN calculates the volume of a thin-walled cylinder by $2\pi R t$, whereas the volume of a solid cylinder is πR^2 . With a wall thickness of $t = R$, this would mean an overestimation of the volume by a factor 2. Thus, by taking the thickness to be $R/2$, the software can be tricked to calculate a solid rod. With the rods modelled as thin-walled structures with $t = R/2$, the volume and the heat exchange with other parts are calculated correctly. The resulting temperature profiles are shown by the red and light-blue lines in figure 4.8. The lines overlap each other; in fact, the two lines can barely be distinguished at the bottom of the graph at $t \approx 4200$ s.

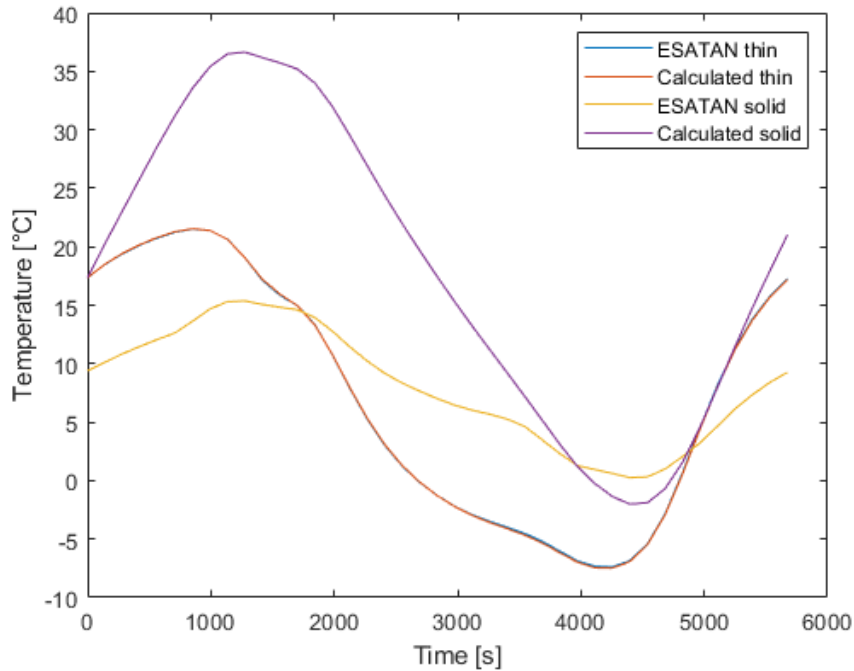


Figure 4.8: Temperature profile of the rods modelled as thin walls versus solids.

4.3.2. Sensitivity checks

Here, the sensitivity of the component temperature profiles to used assumptions is checked. In these comparisons, the temperature profiles of the booms and rods are checked, because they are most critical for the athermalisation procedure.

Sensitivity to monthly variations

The monthly variation in the radiative environment of the telescope consists of changes in Earth's albedo and temperature and a change in solar declination as seen from Earth. Because Earth's albedo and temperature are modelled to only be dependant of the latitude, the longitude over which the satellite flies and by extension the Sun's right ascension do not influence the telescope's temperature. The sensitivity check is intended to check the sensitivity of the telescope's temperature to the albedo and temperature models used. However, because the radiative environment cannot be decoupled from the monthly variation in solar declination, the sensitivity to a changing solar declination is checked. The solar declination values are automatically filled in in ESATAN, and the full list of albedo and temperature values can be found in appendix B.

The temperature variation of the booms and rods resulting from the change of months can be seen in figures 4.9a and 4.9b respectively. Although it is hard to make out the exact effect on the temperature profile per month, it is clear that changing the month has a significant effect. The influence of the change in solar declination can be seen in the shift of the peaks. As the solar declination changes, the satellite enters or leaves eclipse at a different part of the orbit, thus shifting the peaks.

The shape of the temperature profiles, however, is not very important. The temperature difference between the maximum temperature, or the temperature just before the eclipse, and the minimum temperature, or the temperature at the end of the eclipse, is important. In figures 4.10a and 4.10b respectively, the temperature difference between the maximum and minimum temperature is shown per month. The response to changes in albedo and temperature is significant, both for the booms and rods. Because the DST has to operate throughout the year, and because the translation of the secondary mirror depends on both the expansion of the booms and rods, a "worst" case expansion cannot be specified. Therefore, the design is optimised to operate with all combinations of boom and rod temperatures throughout the year.

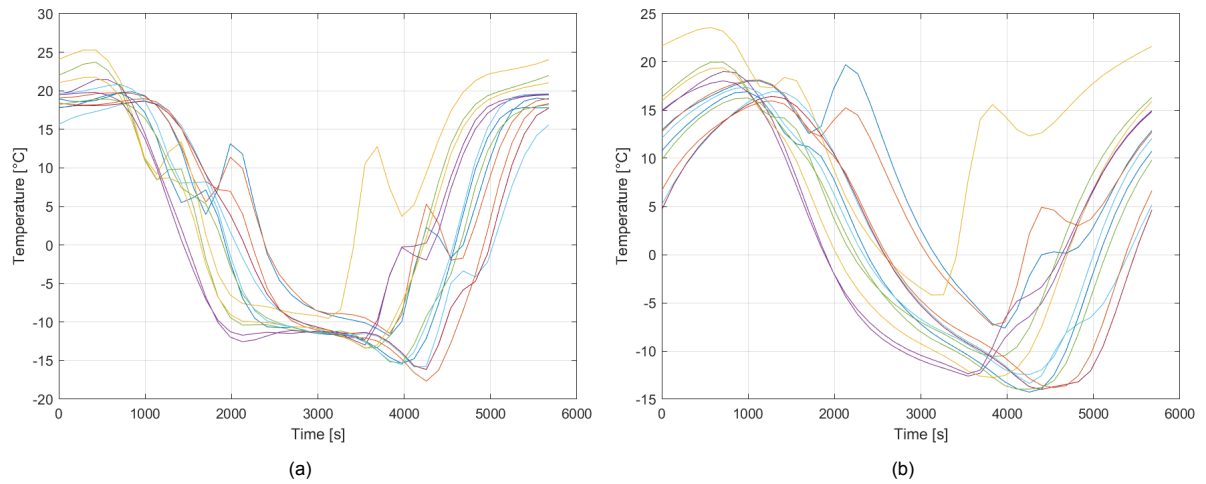


Figure 4.9: Average temperature sensitivity to a change of Month of a) the booms and b) the rods.

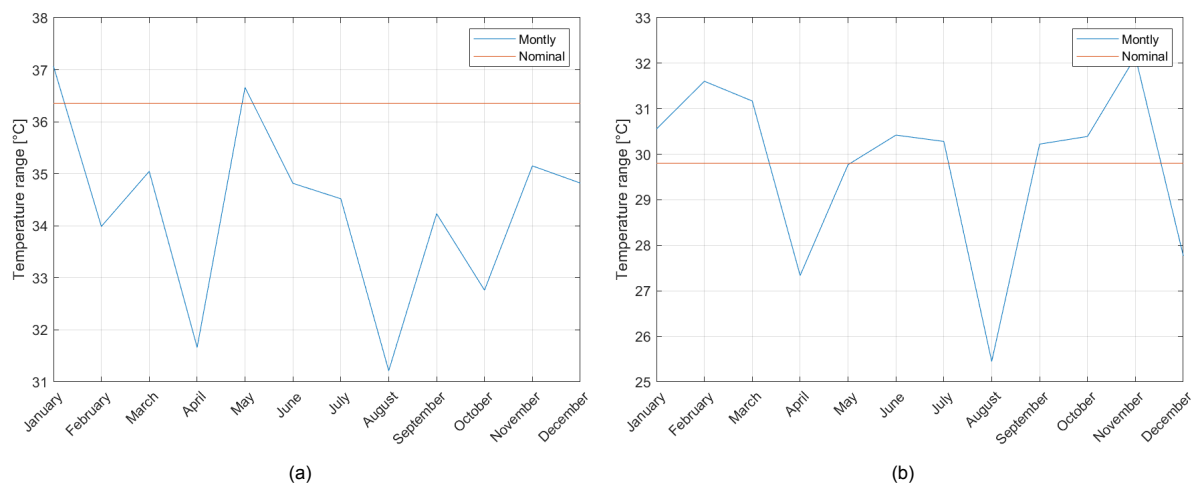


Figure 4.10: Average temperature range sensitivity to a change of Month of a) the booms and b) the rods.

Sensitivity to baffle conductance

As explained in section 4.1, the conductance between the in- and outside layers of the baffle as calculated by the Doenecke method generally has an uncertainty of 25%. The effect of 25% higher or lower conductance values is shown in figures 4.11 and 4.12. Figures 4.11a and 4.11b show the effect on the temperature of the inside of the baffle. As expected, a higher conductance means that the temperature range is bigger. The peaks are higher and the valleys are lower.

The boom and rod temperatures generally follow the temperature profile of the inside of the baffle, as is shown in figures 4.12a and 4.12b. In the nominal case the temperature range, or the difference between the minimum and maximum temperature, of the booms is 35.1 K. For the cases with reduced and increased conductance respectively the ranges are 33.9 and 36.3 K. For the rods, the temperature ranges are respectively 29.8, 29.2 and 30.3 K. Even though the temperature range itself does change significantly, the ratio between the temperature range of the rods and booms does not. If this ratio stays the same, the expansion of the booms and rods changes by the same amount, thus effectively cancelling out the effect of the changed temperature profiles. For the decreased and increased conductance, this ratio changes by respectively -1.7% and +1.4%. Therefore, if rods are used in the design of the SMSS, the translation of the secondary mirror is not very sensitive to a 25% change in baffle conductance. However, future design iterations might change this behaviour and should thus take into account all possible conductance values. Notably, if the rods are omitted from the design, a 25% change in conductance through the baffle does significantly change the amount of translation of the secondary mirror.

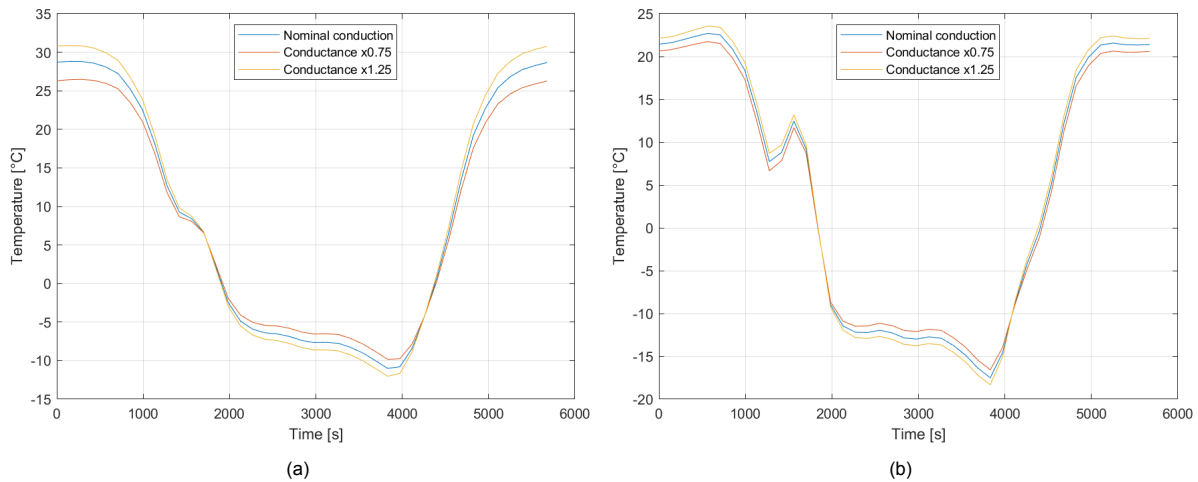


Figure 4.11: Temperature sensitivity to a change in conductance between the in- and outside of the baffle of a) the inside of the bottom panels of the baffle and b) the inside of the side panels of the baffle.

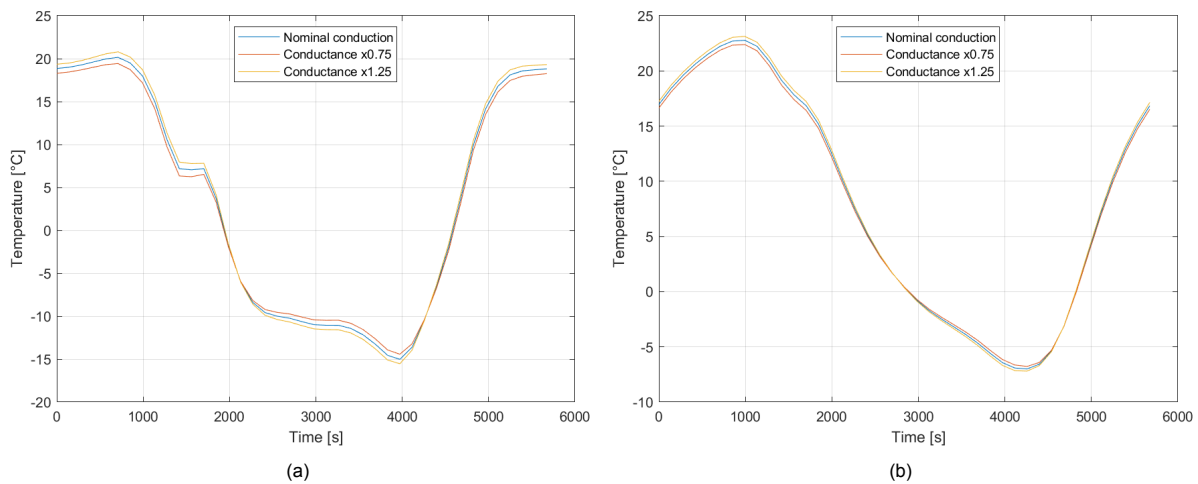


Figure 4.12: Temperature sensitivity to a change in conductance between the in- and outside of the baffle of a) the booms and b) the rods.

Sensitivity to CFRP interface conduction

The CFRP interfaces for which conductive values are calculated are between the deployable booms and CORE hinges and from the CORE hinges to the spider. For these interfaces, the same assumptions were used; therefore, the sensitivity to changes in both interfaces are checked simultaneously. The effect of increasing (x2) and decreasing (x0.5) the conduction through these interfaces on the temperature profile of the booms and rods can be seen in respectively figures 4.13a and 4.13b. The temperature profiles of the booms and rods vary just slightly, and the change in temperature range ratio between the booms and rods is +0.3% and -0.3% respectively. This means that they are not sensitive to a change in CFRP interface conductive values, and thus that these interfaces need not be considered any further.

Sensitivity to CORE hinge conduction

The sensitivity of the temperature profile of the booms and rods to a change in conductive values through the CORE hinges can be seen in figures 4.14a and 4.14b respectively. The difference can hardly be made out by looking at the graphs. The change in temperature range ratio for the booms and rods of around -0.01% and +0.00003% reflects the insensitivity of the temperature profiles to a change in CORE hinge conduction. Again, this means the conduction through the CORE hinges does not need to be considered any further.

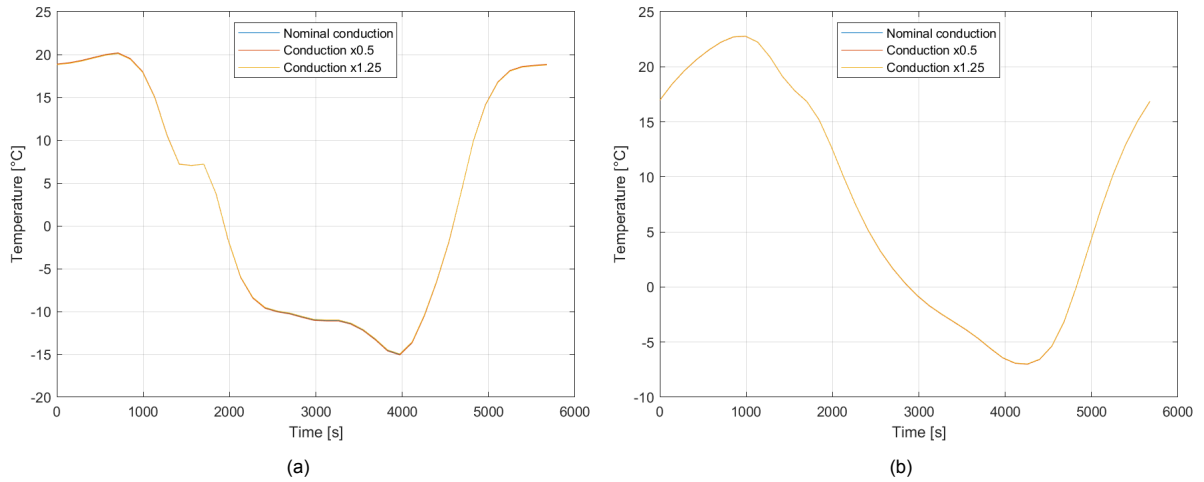


Figure 4.13: Temperature sensitivity to a change in conduction through the different CFRP components of a) the booms and b) the rods.

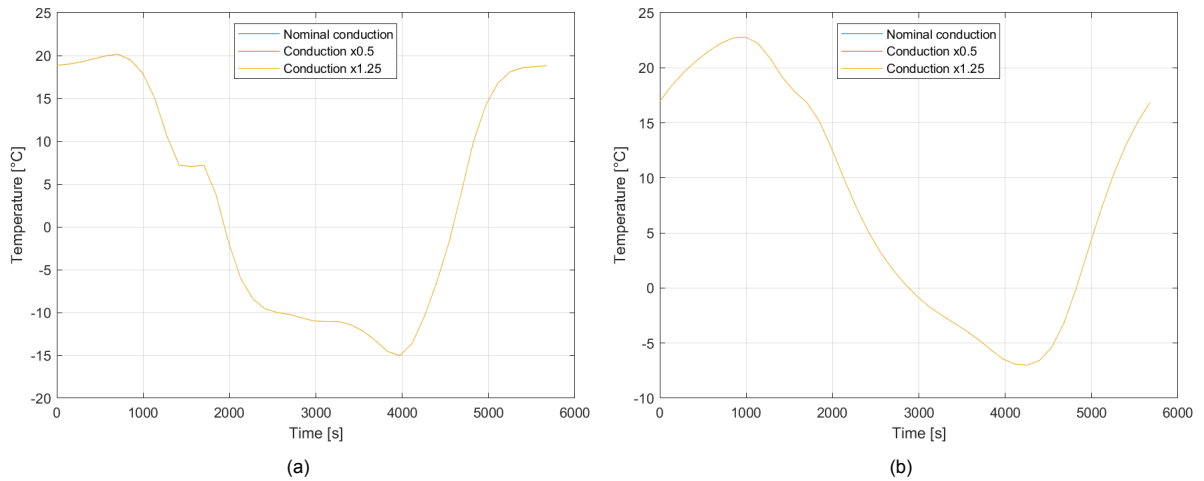


Figure 4.14: Temperature sensitivity to a change in conduction through the CORE hinges of a) the booms and b) the rods.

Sensitivity to spider-rod and rod-secondary interface conductions

The sensitivity of the temperature profiles of the secondary mirror and rods to a change in the conductive values of the spider-rod interface can be seen in figures 4.15a and 4.15b respectively. Here, the temperature of the booms is not taken into account because the spider-rod interface does not, or barely, affect the booms. What immediately stands out is the high temperatures of the secondary mirror. These high temperatures can however easily be explained because much of the incoming radiation is focussed on the secondary mirror by the primary mirror. Even though most of this focussed light is reflected towards the instrument housing because of the mirror's high reflectivity, the heat influx into the mirror is still significant. Since the temperature of the secondary mirror is higher than that of the rods, an increase in conduction between the rods and mirrors means a downwards shift of the secondary mirror temperature profile. The temperature range itself, however, barely changes and the mirror is therefore relatively insensitive to this change. Because the temperature range determines the expansion of the secondary mirror, the mirror is not sensitive to this change in conduction. For the rods, the change in profile is more apparent, with a -1.5% decrease due to the decreased conduction.

The response of the secondary mirror and rod temperature to a change in conduction in the rod-secondary mirror interface can be seen in figures 4.16a and 4.16b. Note that, even though the temperature profile of the secondary mirror looks dissimilar to the nominal case presented in figure 4.15a, the nominal case actually has the same profile (from around 63.9 down to around 62.7 K). The behaviour of the temperature profile looks the same as that of the spider-rod interface. The secondary

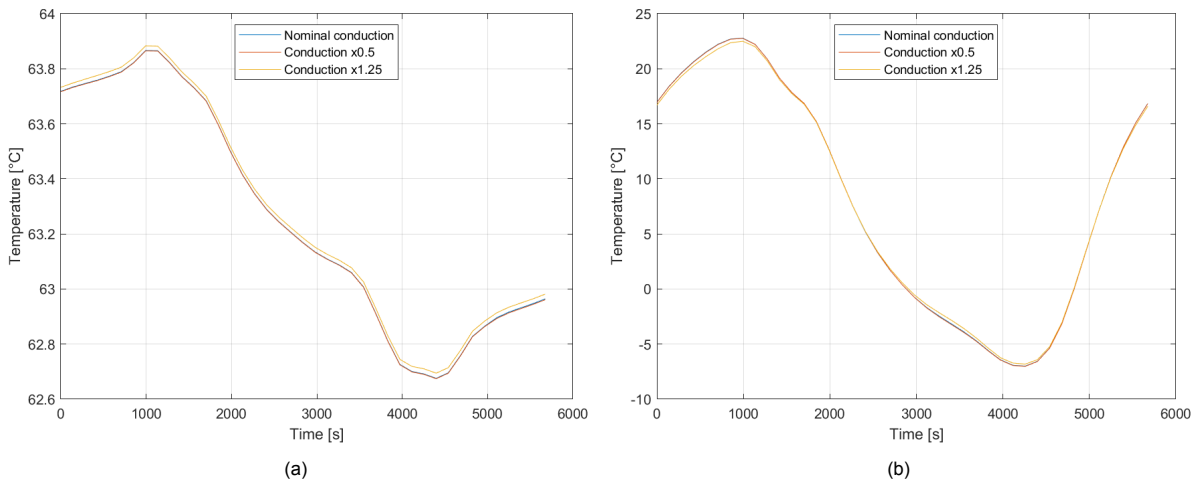


Figure 4.15: Temperature sensitivity to a change in conduction through the connection from the spider to the rods of a) the secondary mirror and b) the rods.

mirror temperature graph gets shifted upwards with lower conductive values and shifted downwards with higher conductive values. What's more, the temperature range of the secondary mirror changes by -1.2% and 2.7% due to a decrease and increase in conduction, respectively. For the rods, this behaviour is inverted. An increase in conduction means an upwards shift in temperature and a decrease in temperature range (-6.8%), while a decrease in conduction means a downwards shift in temperature and an increase in temperature range (+4.2%).

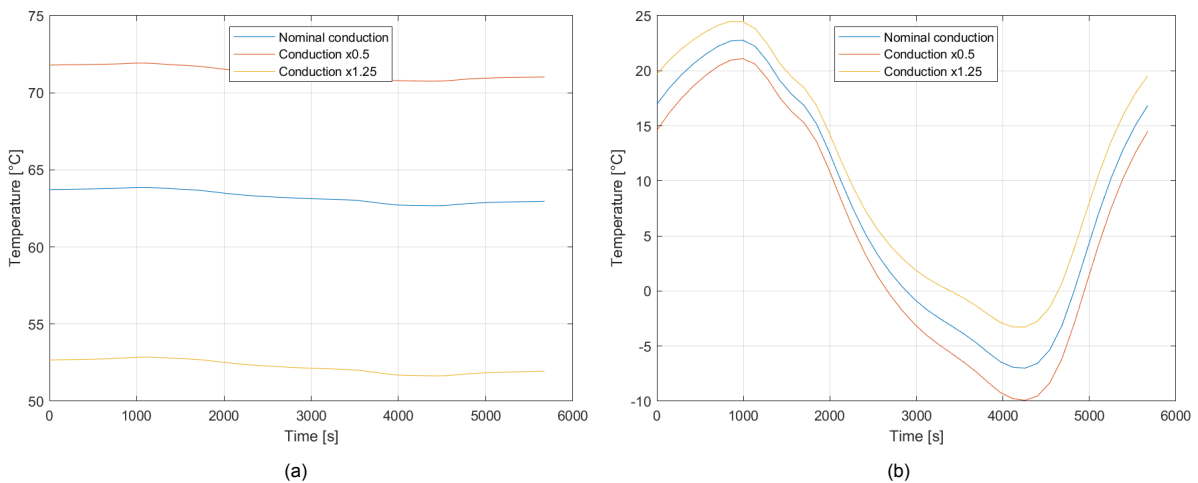


Figure 4.16: Temperature sensitivity to a change in conduction through the connection from the rods to the secondary mirror of a) the secondary mirror and b) the rods.

Concluding, the temperature of the secondary mirror and rods are sensitive to the conductive interfaces between the rods and the secondary mirror and spider. This sensitivity is taken into account in the conceptual design procedure, as presented in chapter 5.

4.4. Results

Concluding from section 4.3, the design procedure should be optimised to account for all possible circumstances. For this purpose, the best and worst cases of the temperature profiles of the booms and rods are shown in figures 4.17a and 4.17b respectively. These best and worst cases are created by combining factors that increase the temperature range of the booms for the worst case and combining factors that decrease the temperature range of the booms for the best case. Notably, the worst cases includes a 25% increase in conductance through the baffle. Because the rod temperature range also

plays a factor in determining these cases, these are not objectively the best and worst cases. It does, however, show within what temperature range the booms and rods are expected to operate. Note that, to enable easy comparison between the cases, the graphs were shifted so that the maximum temperature is shown on the left of the graph.

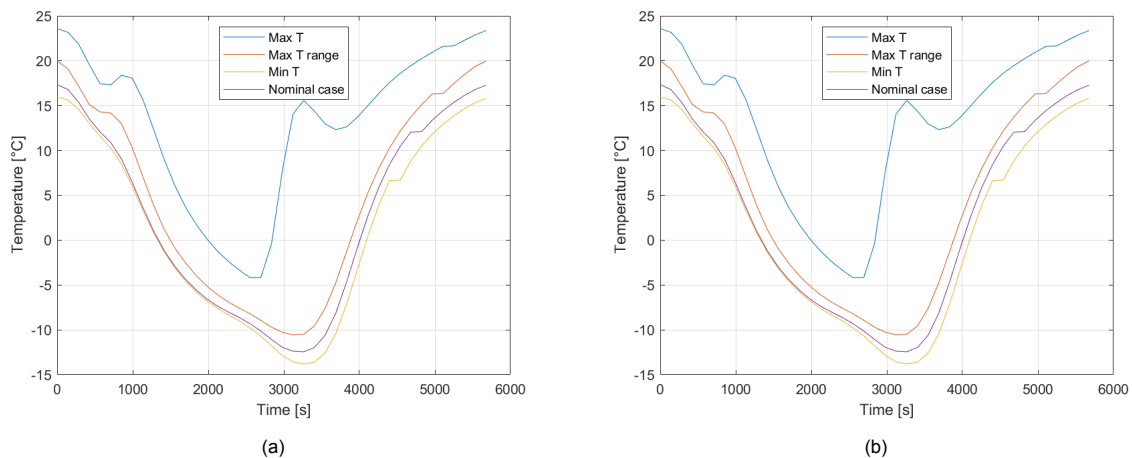


Figure 4.17: Different temperature profiles for the best to worst case scenarios of a) the booms and b) the rods.

The relevant temperature profiles are summarised in table 4.3. The nominal temperature case is shown on the first line, followed by the cases with the highest maximum temperature, the lowest minimum temperature and, finally, the highest temperature range over one orbit. The most important results, as highlighted in the table, are the highest maximum temperature, the lowest minimum temperature and the maximum temperature range. The maximum in-orbit drift is found when the temperature range is the highest, so at a temperature range of 37.1 K. Thus, if the SMSS is capable of keeping the in-orbit longitudinal drift of the secondary mirror to within 2 μm with this temperature difference, it is capable of stabilising the secondary mirror in all orbits. The difference between the highest maximum temperature and the lowest minimum temperature of 43.0 K is the temperature range that defines the maximum overall expansion of the booms throughout its life and thus the maximum overall translation of the secondary mirror. To meet the coarse alignment budget, the translation of the secondary mirror due to this maximum temperature variation has to stay below 10 μm . The conceptual design of the stabilising system, as presented in chapter 5, are initially mainly based on these results. These results are, however, only valid for the exact SMSS design as used in this chapter. Further simulations are required to find the temperature profiles of conceptually different designs. In these further simulations, as performed through this report, the worst-case parameters as defined in this chapter are used. This consists most notably of a 25% higher than calculated conductance through the baffle.

Table 4.3: Temperatures of the booms, rods and CORE hinges.

	Boom temperatures [K]			Rod temperatures [K]		
	Max	Min	Range	Max	Min	Range
Nominal case	20.9	-15.5	36.4	17.4	-12.4	29.8
Highest T	25.3	-9.5	34.8	23.6	-4.2	27.8
Lowest T	19.0	-17.7	36.7	16.0	-13.8	29.8
Max T Range	23.7	-13.3	37.1	20.0	-10.6	30.6
	top CORE temperatures [K]			Root CORE temperatures [K]		
	Max	Min	Range	Max	Min	Range
Nominal case	16.1	-12.7	28.8	14.4	3.7	10.8
Highest T	22.2	-4.7	26.9	18.8	8.8	10.0
Lowest T	14.6	-14.0	28.7	12.9	2.2	10.7
Max T Range	18.7	-11.1	29.8	16.0	5.1	10.9

5

Concept generation

In this chapter, the different concepts to stabilise the secondary mirror with regards to the primary mirror as formulated in Akkerhuis (2019) are expanded and evaluated. Firstly, the concepts are introduced in section 5.1 and the non-feasible concepts are eliminated. The concepts that are not eliminated are further detailed in section 5.2. Their working principles are discussed, and their strong and weak points explained. The concepts that cannot fulfil all requirements are eliminated. Finally, in section 5.3, the concepts are traded-off against each other, and the best concept is selected to be designed.

All concepts need to comply to the in-orbit drift budgets determined in equations (2.7) to (2.9), which are shown slightly modified in equation (5.1).

$$\begin{aligned} L_B - L_{SMSSz} &= 1571.07 \text{ mm} \\ \Delta z &= \alpha_B L_B \Delta T_B + \alpha_H (L_{HT} \Delta T_{HT} + L_{HR} \Delta T_{HR}) - \Delta L_{SMSSz} \leq 2 \text{ } \mu\text{m} \\ \Delta \gamma &= \tan^{-1} \left(\frac{\alpha_B L_B (\Delta T_{Bp} - \Delta T_{Bn}) + \alpha_H (L_{HT} (\Delta T_{HTp} - \Delta T_{HTn}) + L_{HR} (\Delta T_{HRp} - \Delta T_{HRn}))}{w_{sp}} \right) - \\ \Delta \gamma_{SMSS} &\leq 6 \text{ } \mu\text{rad} \end{aligned} \tag{5.1}$$

The results presented in section 4.4 form the baseline temperature ranges in which the concepts need to operate. From these results, combined with the values for the CTE and length of the relevant components as found in section 2.5, initial estimates of the translation and rotation that the SMSS needs to compensate for can be calculated. These estimations result in a maximum longitudinal translation of the secondary mirror of 70.7 μm and a maximum rotation around the X- or Y-axis of about 2.8 μrad . Note that these results are based on the baseline design presented in Krikken (2018) and Arink (2019). Any conceptual change also changes the above equations and thus yields other results. From these values, it becomes clear that the longitudinal in-orbit translation of the secondary is the primary driver of the SMSS design. The rotation of the mirror, even without correction, does not exceed the in-orbit drift budget. Furthermore, even though the maximum temperature difference of 43.0 K between the highest (maximum temperature in December) and lowest (minimum temperature in May) overall temperatures is higher than the maximum in-orbit temperature range, this maximum range corresponds to the coarse alignment budget, which is five times higher than the in-orbit drift budget. This 6 K higher temperature range does not account for a five times increase in translation, which means the in-orbit temperature range is critical. The main driver for the design of the SMSS is thus to make sure that the in-orbit longitudinal translation budget is not exceeded. That being said, all other budgets need to be met as well.

5.1. Identification and selection of design concepts

This section discusses the concepts that can potentially stabilise the secondary mirror. First and foremost, the different concepts ought to fulfil the inequalities shown in equation (5.1), of which the longitudinal translation is the main driver. Further design drivers are a low mass and low complexity. These

two criteria are chosen because they encapsulate most other criteria, which is further discussed in the trade-off as performed in section 5.3. The different methods to stabilise the secondary mirror utilise different parameters within these equations to meet the budgets. The first concepts, as described in section 5.1.1, makes use of athermalisation. Athermalisation uses a set temperature input to find a combination of materials and component lengths that keep the mirror as stable as possible. Next, the concepts based on thermal control are explained in section 5.1.2. Finally, section 5.1.3 treats the concepts that make use of active positioning. The different concepts are visualised in the Design Option Tree (DOT) in figure 5.1.

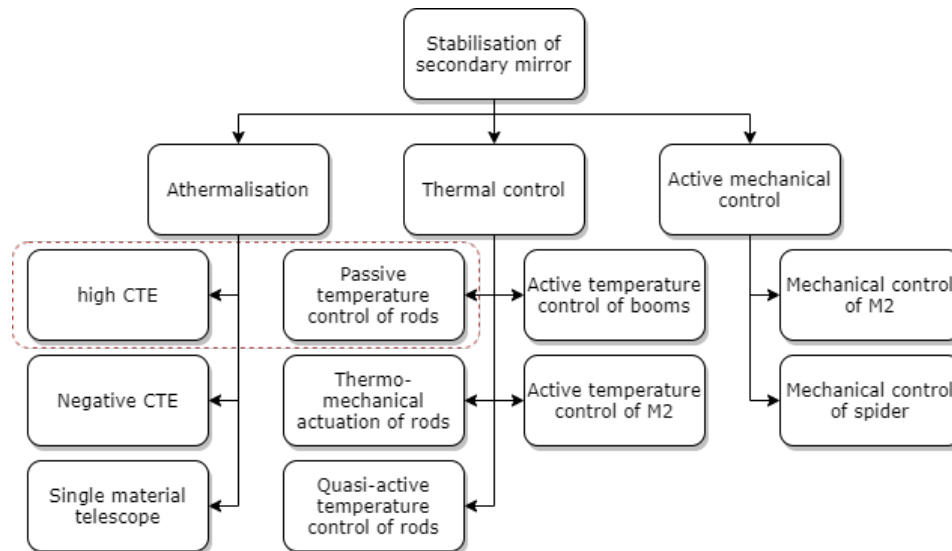


Figure 5.1: Design option tree of secondary mirror support structure.

5.1.1. Athermalisation

The first concepts to stabilise the telescope booms consist of athermalising the design. In pure athermalisation, the design has to operate correctly regardless of temperature. This means that the CTEs and lengths of the different components are adjusted to achieve the desired stability. The length is changed by making a component longer or shorter, while the CTE is changed by changing the used material. Stabilisation through athermalisation can be realised in multiple ways. Firstly, the rod and boom material and lengths can be chosen such that the expansion of the rods compensates for the expansion of the booms, thus achieving a total translation and rotation close to zero. Secondly, a negative thermal expansion material can be placed in series with the booms as to have a net-zero expansion. A final strategy employs a single-material telescope structure where all parts expand equally.

High CTE mirrored orientation beams

The expansion of the booms is driven by their temperature increase. Their low CTE of $0.8 \mu\text{m}/\text{m.K}$ means that, despite their high length, they only expand about $50 \mu\text{m}$ due to a 35 K temperature increase. This expansion can be compensated by using beams with a high CTE, which are orientated in the opposite direction of the booms. Now, the secondary mirror has to be mounted to remove any thermally induced stresses in the mirror. These mountings can take many forms, and one of these forms consist of the hexapod structure as proposed by Krikken[3]. By mounting the secondary mirror on rods with a high CTE and balancing the length of the rods such that they exactly compensate for the expansion of the booms, the telescope can be athermalised. In the design iteration presented in Krikken (2018), these rods are made out of aluminium 7075-T6 with a CTE of $23.6 \mu\text{m}/\text{m.K}$. This high CTE means that, with a similar temperature profile, the rods only need to be about 1/30th the length of the booms. This specific alloy is particularly well suited for this task because on top of its high yield strength and CTE it also has a high reduced tensile strength, which is a crucial trait for flexures.

Negative thermal expansion material

Instead of using high CTE beams in the negative z-direction, beams with a negative thermal expansion coefficient can be placed in series with the deployment booms. This means that when the temperature of the telescope increases the booms expand, but the part that is made of negative CTE material contracts, thus making it possible to nullify the translation of the secondary mirror. However, controlling the properties of negative CTE materials is hard, and their behaviour is difficult to predict. These problems can be solved by placing the materials within fibre composites, which stabilises the structure and allows for predictable behaviour.[43–45] These materials, however, have so far only been created in computer models and tested in laboratory environments, and even here much work remains. Commercial off-the-shelf (COTS) products made of negative CTE materials are definitely not available. The risk of too high development time and or too low performance is high. This concept is thus eliminated.

Single material telescope

The longitudinal misalignment of the secondary mirror is not only caused by the expansion of the deployment booms, but also because of the difference in CTE between the different components. A telescope can also be made such that all components expand and contract equally. Such equal expansion means that the image stays focussed, albeit it the image scale changes.[46] Single material telescopes are mainly used for ground-based applications, as a single-frame telescope is inherently bulky, and because the temperature of the frame needs to be homogeneous. Because the DST needs to be light-weight and deployable, and because it is complicated to precisely control the temperature of the whole telescope, this concept is also eliminated.

5.1.2. Thermal control

Instead of controlling the CTE and length of the different components in equation (5.1) to make sure the mirrors are properly aligned, the temperature can also be controlled. In the design of the DST a form of thermal control is already applied by the baffle, which passively shields the telescope from incoming radiation.[4] By blocking part of the radiation, the difference in radiation level reaching the telescope decreases, thus decreasing the temperature variation of the different components. Thermal control can also be applied to individual components. By changing the temperature of a component, the amount by which it expands or contracts also changes. In principle, all components of the DST can be thermally controlled, but here only the thermal control of the booms and rods is considered because they are critical for the stability of the secondary mirror. In the design of any thermal control system, MIS-REQ-14 should be taken into account. Because the thermal control system also has to be usable if the telescope is changed to a thermal infra-red telescope, the thermal control system should not significantly alter the infra-red radiation levels within the baffle. Furthermore, all components that have a direct line of sight to the field stop should reflect as little visible light as possible. For this reason, these components are coated with magic black, a coating with a high absorptivity. The coating of, for instance, the booms can therefore not be changed.

Thermal control is divided into two main groups, namely passive and active thermal control. Passive thermal control consists of designing the thermal system such that the different components are at the desired temperature, or in the desired temperature range, without actively controlling anything. The baffle is thus an example of passive thermal control. In active thermal control, the system can respond to changes in the thermal environment by, for instance, turning on heaters or increasing the emissivity of parts to increase the heat loss by radiation. The first concept is based on the passive thermal control of the rods, while the following three concepts are those based on heating the rods, booms or secondary mirror through electrical heaters. Finally, a concept using quasi-active thermal control of the rods is presented. Quasi-active control of the booms is not considered because this entails choosing a different coating, which is not possible for the booms. It must be noted that none of these concepts work without choosing a proper rod material and length to go with the temperature profile.

Passive thermal control of the rods

The temperature of the rods is determined by the amount of radiation they absorb and emit and their heat exchange with the secondary mirror and spider by conduction. The amount of radiation the rods absorb and emit can be controlled by changing the absorptivity and emissivity of its surface. Furthermore, the heat exchange between the rods and spider can be controlled by changing the conduction

through the rod-spider interface. The Albedo and infrared radiation coming from Earth heat the spider. Now, the temperature of the spider can be passively controlled by choosing the thermo-optic properties of the spider surface by changing the applied coatings. Here, variants like thermochromic coatings, which have varying thermo-optic properties depending on their temperature, could be utilised. This heat can then be transferred into the rods to increase the temperature variation in the rods. Passively controlling the rods can thus consist of selecting the surface coating of the rods and spider and defining the conductive path between the spider and rods.

Thermo-mechanical actuation of the rods

Electrical heaters can be applied to the rods to increase their temperature when necessary. In such a system, the lowest temperature of the rods is calibrated to match the lowest temperature of the booms to exactly align the mirrors. Then, as the booms heat up and expand, the heaters turn on and increase the temperature of the rods to exactly solve the equations in equation (5.1). Because there is no direct line-of-sight between the rods and the field stop, the radiation emitted by the heaters does not fall directly on the field stop, and thus MIS-REQ-14 is not necessarily violated.

Active thermal control of deployment booms

Instead of heating the rods, the heaters can also be applied on the deployment booms. The reasoning to apply this heat is, however, inverted. Instead of heating the rods to counter the temperature increase of the booms during the sunlit phase, the booms can be heated during eclipse. This flattens the temperature curve during the sunlit phase, thus decreasing the expansion of the booms. It would seem that actively heating the booms violates MIS-REQ-14, as infra-red radiation emitted by the booms might enter the instrument housing. However, because the heating is applied during eclipse to increase the minimum temperature, and not to increase the maximum temperature, the infra-red radiation level is not much higher than what would already be present. The temperature profile does, however, shift upwards, so care must be taken to ensure that the entire temperature profile does not shift upwards too much. Instead of increasing the minimum temperature of the booms by applying heat, the maximum temperature of the booms can also be decreased by applying cooling. A possible option to do this would be by using thermoelectric coolers, which operate on the Peltier effect. Other options like pumped fluid loops and phase-change materials are not considered as they are either very complex or bulky.[31]

Local heating of secondary mirror

The width of the secondary mirror and its radius of curvature change due to changes in temperature, thus shifting the focal point.[24, 47] The longitudinal translation of the focal point due to thermoelastic effects can be used to counter the expansion of the booms. The temperature can be increased by applying electrical heaters on the backside of the mirror. However, increasing the secondary mirror temperature increases the level of infra-red radiation entering the instrument housing. Furthermore, because the heating can only be applied to the backside of the mirror, local non-linear thermal expansion effects might occur. As a result, the manner by which the secondary mirror expands might be hard to predict[48]. These two reasons mean that it is impractical to apply heating to the secondary mirror, and thus that this concept is not considered feasible.

Quasi-active thermal control of rods

In quasi-active thermal control, no active heating is applied to components. Instead, the thermo-optical properties, so the emissivity and absorptivity of a surface, are changed. Changing the thermo-optical properties means a different heat-exchange with the environment and thus that the temperature changes. There are multiple ways to change the thermo-optical properties of a surface, of which electrochromic coatings show the most promise. By applying a small voltage to the coating, ions flow from the inner to the outer layer, thus regulating the emissivity and absorptivity of the coating. Such coatings should be applied to components with a direct line of sight to space, such as the spider. When applied to the spider, the temperature of the spider can be controlled. By including high-conductivity paths between the spider and the rods, the temperature of the rods can be controlled indirectly thus providing the required stability of the secondary mirror.[49–51]

5.1.3. Active mechanical control

Active control of the secondary mirror consists of using actuators to change the position and orientation of the mirror. Conceptually, there are two ways to achieve the required actuation, namely by directly actuating the secondary mirror or by actuating the spider as a whole. This actuation can be achieved by different motors, all with their pros and cons.

Actuated secondary mirror

There are two concepts currently used in similar projects to provide direct actuation of single element mirrors, namely by using a hexapod drive or by using an eccentric drive. Both drives can potentially meet the requirements. Hexapod actuators have the same overall geometry as the hexapod structure as used for the rods in the design of Krikken (2018). An overview of a hexapod actuator can be seen in figure 5.2. By actuating all six rods, the secondary mirror can be controlled precisely in all six degrees-of-freedom.

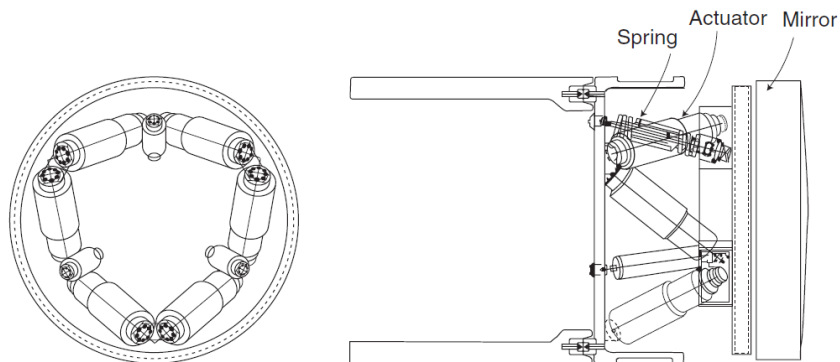


Figure 5.2: Hexapod mount used on the Subaru telescope. Retrieved from Bely (2003).

Eccentric drives consist of six angular motors, as shown in figure 5.3. A rotation of one of the shafts produces a displacement of the links as a function of the actuator shaft angle. These link displacements allow the mirror to be actuated in all six degrees-of-freedom.[52]

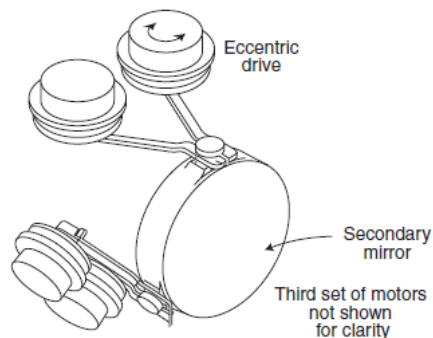


Figure 5.3: Eccentric drive. Retrieved from Bely (2003).

Actuated spider

Instead of directly actuating the secondary mirror, the actuation can also be applied on the interface between the booms and the spider. Such a concept would require one linear actuator placed between each boom and top CORE hinge. These linear actuators would allow for rotating the mirror around the X- and Y-axis and translate along the Z-axis.

5.1.4. Concept conclusion

In the following section, the concepts which have not been eliminated are further discussed. A final note on the discussed concepts is that almost all of them make use of passive thermal control and

athermalisation methods, in some way or another. In active thermal control, the rod material should still be chosen to fit the temperature profile, and for active actuation, the temperature of the actuators should also be taken into account. This means that going forward, the athermalisation concepts of using high CTE rods and the passive thermal control concepts are combined in one concept, henceforth to be called the athermalisation concept. The eliminated concepts are highlighted in red in figure 5.4, and the concepts that are further detailed are left blank. The athermalisation concept is the combination of the concepts utilising high CTE rods and passive thermal control, as visualised by the dotted line.

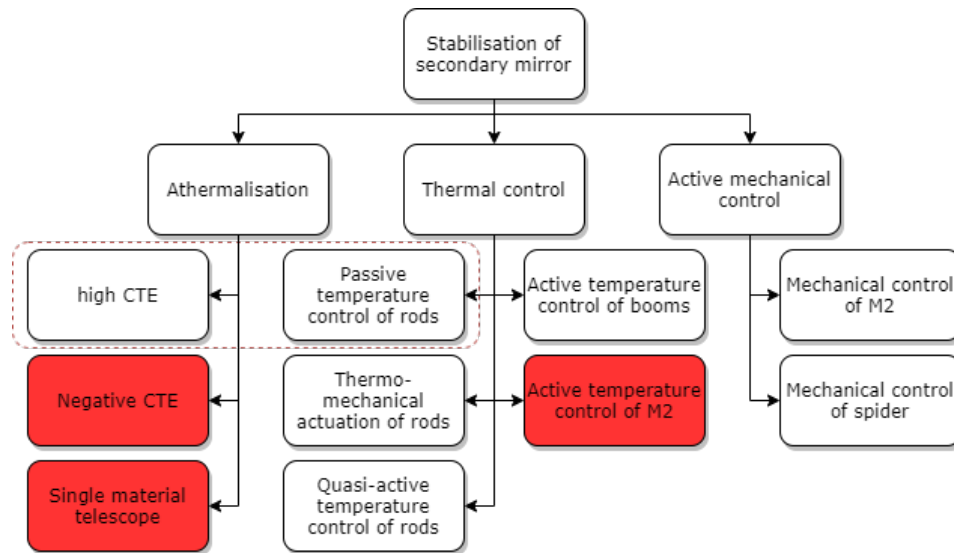


Figure 5.4: Design option tree of secondary mirror support structure with three concepts eliminated (red).

5.2. Preliminary design and analysis of selected concepts

All concepts, as presented in section 5.1, which were not eliminated, are potentially able to fulfil all requirements as posed on the stability of the secondary mirror. In this section, they are further investigated. Their working principles are given, and initial mass and power consumption estimations are made, which act as the main output of the preliminary designs. Their advantages and disadvantages are stated. As stated in the introduction of this chapter, the in-orbit temperature range of 37.1 K and the resulting longitudinal translation of the secondary mirror are used as the main driver for the conceptual designs. The concepts should thus be designed such that they are capable of providing 68.7 μm longitudinal translation. In section 5.2.7, an initial conclusion is drawn.

5.2.1. Athermalisation

This concept contains solely passive components. The secondary mirror mount consists of a hexapod structure made of Aluminium 7075-T6. For this initial design phase, the parameters, as defined in Krikken (2018) are assumed to be correct. These parameters are, for instance, the radius of the booms and the thickness and length of the flexures. They are based on a vibrational and stress analysis, which is out of the scope of this preliminary design phase. These parameters are mainly the radius of the rods and the angle by which they are placed. The radius of the rods is for now assumed to be 5 mm. The angle by which the rods are placed is determined by the circles that describe the attachment points on the spider and secondary mirror, and the points on which they are attached to these circles. Krikken uses a ratio of 2/3 for the radius of the secondary mirror attachment points and the radius of the spider attachment points. The size of the secondary mirror only allows for the attachment points to be placed on a circle with a radius of around 3.7 cm, meaning the spider attachment points are placed on a circle with a radius of 5.6 cm. The angle over which they rotate about these circles is assumed to be 60°.

With this information, a quick estimation of the mass of a system consisting only of the rods can be made. The length of the rods can be calculated by solving the system of equations as seen below. Here, the known values for the expansion of the core hinges and the constant part of the booms is already

filled in. Because the secondary mirror is mounted on negatively oriented rods, the distance between the primary and secondary mirror is decreased. For this reason, the booms need to be extended by the length in the z-direction of the rods.

$$\begin{aligned} L_B - L_{SMSSZ} &= 1571.07 \\ L_B \alpha_B \Delta T_B - L_{Rz} \alpha_R \Delta T_R &= \end{aligned} \quad (5.2)$$

With a temperature range of 30.6 K, the rods have a length in the z-direction of 8.6 cm. This means that the rods have a total length of 9.9 cm, giving them a mass of 0.022 kg per rod for a total mass of 0.130 kg. The length increase of the booms due to the negatively oriented rods is also 8.6 cm, which means an addition in mass of 0.054 kg. Furthermore, the increased length of the booms means the length, and thus the mass, of the baffle also increases. The variation in mass of the baffle results from the variation in length of the beams and MLI of the baffle. This variation is best described by finding the mass per meter of the baffle and multiplying this by the increase in length. The total mass per meter of the baffle is 2.218 kg/m. Thus, for an increase in length of 8.6 cm, the mass increases by 0.191 kg. In total, the system would have an added mass of around 0.374 kg. Note that this mass does not include the mass of the attachment points. For this initial mass estimation, these are not taken into account because all concepts include some form of attachment points. As such, they do not pose a real advantage for any of the concepts. Such parts are designed in the detailed design phase, as outlined in chapter 6.

It might be possible to decrease this mass by utilising passive thermal control of the rods. Here, three ways to increase the temperature range of the rods are considered. Firstly, the rod's thermo-optical properties can be changed by applying a coating. Secondly, the conductive values between the rods and the secondary mirror and spider respectively can be changed. Finally, the temperature of the rods can be influenced indirectly by changing the temperature of the spider, which can be passively controlled by changing the thermo-optical properties of the top-plate.

Because the thermal model of the telescope is already available within ESATAN, it is a trivial task to check the influence of changing the thermo-optical properties of the rods and changing the conductive values of the attachment points. It turns out that a coating with a high emissivity and absorptivity gives the highest temperature range within the rods. This is to be expected because a high emissivity and absorptivity give the fastest response to a changing radiative environment, as present within the baffle. Secondly, it turns out that reducing the conduction through the attachment point to the secondary mirror increases the temperature range of the rods. The conductive interface between the secondary mirror and rods was, however, already set to be as low as possible in the initial thermal model. There is thus no additional gain to be achieved here.

Then, for the third possibility of controlling the rod temperature via the spider top-plate. A set of varying coatings, ranging between values of 0.1 and 0.9 for both the emissivity and absorptivity, were checked. It turns out that the applied coating of magic black was already ideal for achieving the highest temperature modulation. However, even with the applied coating of magic black and the inclusion of a highly conductive path between the top-plate and the rods, it is not possible to increase the temperature range of the rods. This is mostly caused by the fact that the top-plate acts as a heat sink when leaving eclipse. After the eclipse, the temperature of the top-plate is much lower than that of the rods. This means that, after the eclipse, energy flows from the rods into the top-plate. Even though the temperature of the rods still increases, the temperature gradient of the rods is decreased. The main consequence is that the spider acts as a heat sink for the rods, which means that the assumption made in section 4.2 regarding the conduction between the rods and the spider was erroneous. This conduction was assumed to be high, whereas it turns out a lower value is preferable. Changing the conductance value of the rod-spider interface to 4000 W/m².K yields the best results.

The optimal passive thermal design yields a rod temperature range of 32.2 K. Furthermore, the boom temperature range has changed to 36.0 K. With these new temperature ranges, the length of the rods in the z-direction changes to 7.9 cm, leading to a total rod length and mass of 9.3 cm and 0.123 kg respectively, an additional boom mass of 0.049, an additional baffle mass of 0.175 kg and a total mass increase of 0.347 kg. This concept has the advantage that it is simple. There are no moving parts,

making it a very robust system. However, this analysis only shows whether the system can achieve the required full range of motion over the entire temperature range. This does not necessarily mean the secondary mirror stays within the in-orbit drift budget throughout the whole orbit. Figure 5.5 shows a mismatch between the temperature profile of the rods and booms. The eclipse, shown by the shaded area in the figure, is defined as the part of the temperature profile of the booms where the temperature is decreasing. This is not a perfect definition because the temperature does not necessarily decrease in eclipse, but the eclipse is expected to mostly align with a decrease in temperature. This definition is therefore suitable for this initial analysis. The telescope is only actively used during the sunlit phase, so the shaded area is left out of the analysis. The outer edges of the eclipse denote the maximum and minimum temperature of the booms. Ideally, the minimum and maximum temperature of the rods align perfectly with those of the booms. However, as seen at A and B, this is not the case. This misalignment means the rod temperature range as specified earlier is not valid; in reality, a lower range should be used. Furthermore, throughout the orbit, the shape of both temperature profiles differs significantly. This is best seen at C, where the temperatures are very different. Additional analysis shows that over the whole range of possible rod lengths, the lowest deviation in secondary mirror location is found to be $20 \mu\text{m}$. This translation is much higher than the allowed motion. The passive athermalisation concept is therefore not feasible.

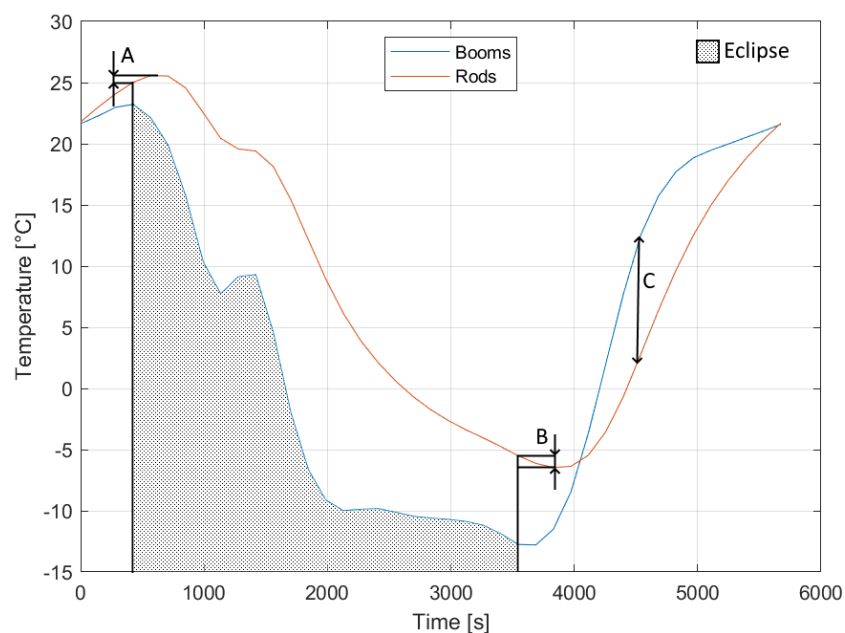


Figure 5.5: Mismatch between the temperature profile of the booms and rods. A. and B. respectively indicate that the maximum and minimum temperatures of the booms and rods do not occur at the same time. C. indicates that the temperatures of the booms rises much quicker than that of the rods.

5.2.2. Thermo-mechanical actuation of the rods

Heaters can be used to increase the maximum temperature of the rods. This increase in maximum temperature directly translates to a higher expansion of the rods and thus a lower initial length and mass. A higher heating power means a higher temperature range within the rods and thus shorter rods. It, however, also means a higher power consumption. To determine the optimal power consumption, a dynamic analysis accounting for different heater input levels is performed. The optimal solution is then found by finding the minimum SMSS mass. To calculate the length of the rods, the same principles as used for the passive athermalisation are used. Because of the complexity of the system, setting up analytic relations to determine the temperature of the rods with different heat input levels is time-consuming. Instead, a set of input heat powers is implemented in ESATAN. The resulting temperature profiles are used to set up analytic relations to calculate the mass of the SMSS.

The heat balance and resulting temperature of the rods without any heat applied can be seen in fig-

ure 5.6a. The dotted line represents the telescope leaving the eclipse, or at least the moment at which the temperature of the rods starts increasing. After this point, until the orange line crosses 0 again, there is a positive heat balance, meaning the temperature of the rods increase. The shaded area shows the area over which the heat balance is positive. The average positive heat balance is 1.32 W. Thus, with an average positive heat balance of 1.32 W, the temperature increases by 31.0 K. We know that the heat radiated by the rods scales by the temperature to the fourth power, thus that at higher temperatures more heat is radiated from the rods. This means that to achieve a higher maximum temperature, on average, even more power than 1.32 W is required. To check the behaviour of the heated rods, a heating power of 2 W (P) spread out evenly over all rods is used. Because the temperature profiles of the six rods are similar, it is at this point in the design phase not necessary to distribute the heat according to their individual heat balances. Applying this heat evenly over the six rods results in the temperature and heat balance shown in figure 5.6b. The jumps in heat balance are easily spotted where the heat balance graphs crosses 0. Then, as the temperature gradient of the rods increases, the difference between the two heat balance lines diminishes. This diminishing return makes sense because the higher temperature of the rods means more heat leaves the rods via radiation and conduction. The resulting temperature behaviour of the rods due to a consistently applied heat is thus as expected.

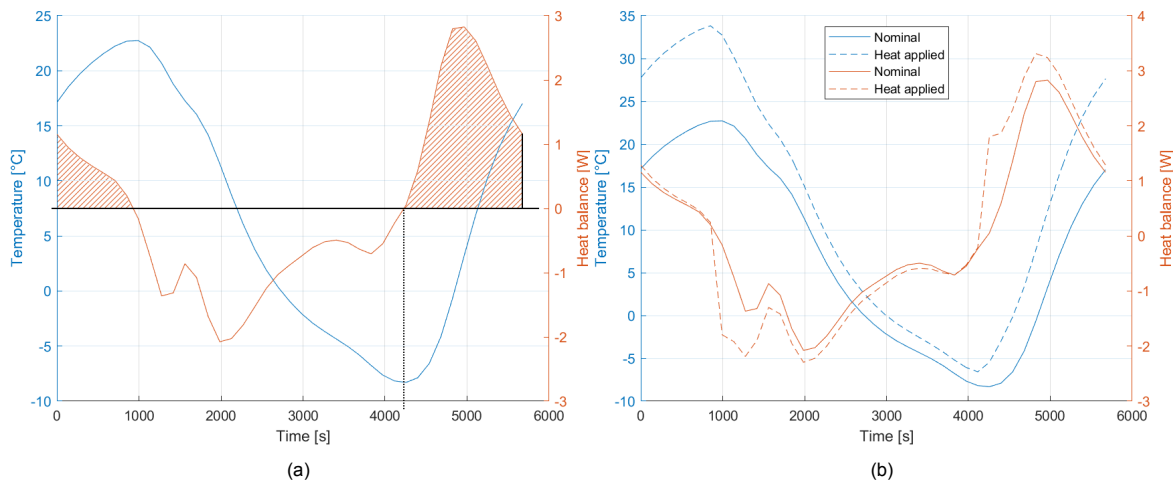


Figure 5.6: Temperature profile of the rods a) without and b) with heat applied.

With 2 W of applied heat, the temperature range was increased by 9.4 K. To find the optimal solution of input power and resulting temperature range, several power input levels were checked. The resulting temperature profiles of the rods can be seen in figure 5.7. The response to a higher heating power can easily be distinguished. The change in temperature range due to the applied heat is shown in figure 5.8. The red line shows a polynomial ($T_{range}(P) = -0.04935P^2 + 5.319P + 32.17$) fit to the found data points. The Root-Mean-Square Error (RMSE) is 0.16, which is sufficient in this design phase. With this fit, the optimal solution regarding power requirements, complexity and mass can be found.

Of course, the temperature of other relevant components, namely the booms, CORE hinges and secondary mirror, are also affected by heating the rods. The effect on the temperature range of these components and the accompanying polynomial fits is shown in figure 5.9. The process for obtaining these is the same as described for the rods.

The polynomial fits for the temperature ranges are given in equation (5.3).

$$\begin{aligned}
 T_{B_{range}}(P) &= 1.556 \cdot 10^{-4}P^2 + 0.016462P + 36.0149 \\
 T_{RC_{range}}(P) &= -4.6902 \cdot 10^{-5}P^2 + 0.013361P + 10.2547 \\
 T_{TC_{range}}(P) &= 3.6815 \cdot 10^{-4}P^2 + 0.040843P + 29.3254
 \end{aligned} \tag{5.3}$$

With these fits, and the fit for the rod mass, an equation can be set-up where the length of the rods, and by expansion also that of the booms and baffle, vary as a function of the input power. With this length variation, the mass of the system is directly calculated. This results in a graph where the mass is plotted as a function of the input power. This is shown the geometric mass in figure 5.11. This mass

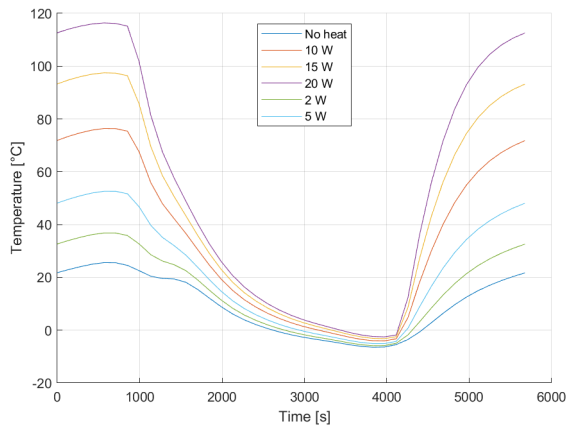


Figure 5.7: Temperature response of the rods to different levels of applied heat

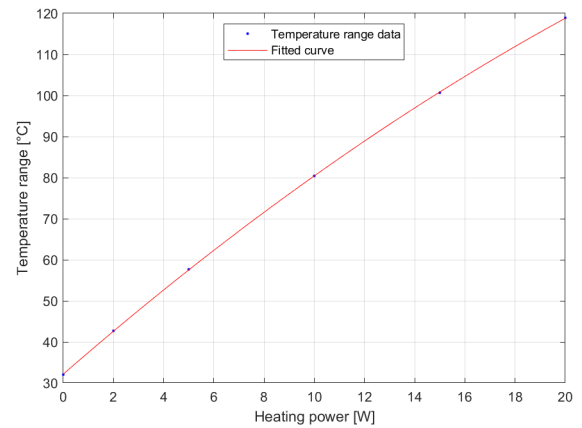


Figure 5.8: Polynomial fit of temperature range of the rods versus applied heat

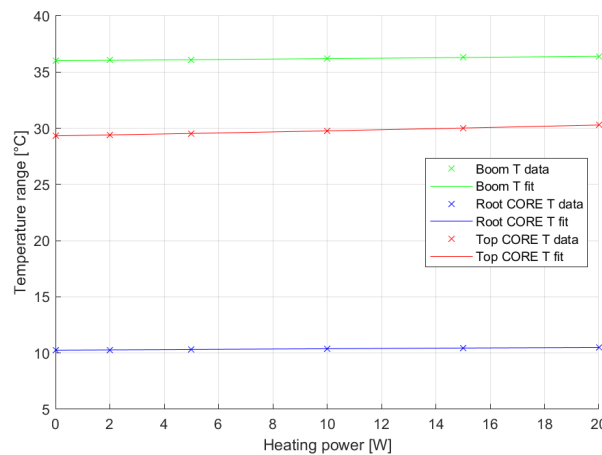


Figure 5.9: Polynomial fit of the temperature range of the booms and root and top CORE hinges.

is equivalent to the mass found in section 5.2.1.

Next to the decrease in mass of the booms, rods and baffle, the increase of mass due to additional parts also needs to be accounted for. These additional parts consist mainly of the heaters themselves and the cabling required to power the heaters. Of course, other parts are also present, but for a first-order estimation, these are sufficient. Lastly, due to the increased power draw, the solar array mass also increases.

A commonly used type of electrical heater is the film heater.[53] Film heaters can be applied on any surface, meaning they can also be applied on the round surface of the rods. The voltage of the satellite power system is assumed to be 28 V, a standard for small satellites. Assuming a 2 % voltage drop through the cables, which is the industry standard for maximum cable loss in satellites, a heater voltage of 27.44 V is achieved.[54] With this voltage, the ideal resistance is calculated by $R = U^2/P$. The product information of Minco Products, Inc., an aerospace heating system manufacturer, gives a standard resistance per unit area of $230 \Omega/\text{cm}^2$. Minco furthermore gives a heater weight of around $0.04 \text{ g}/\text{cm}^2$. [55] Using these relations, a quick estimation of the heater mass as a function of heater power is derived.

From the ideal resistance, the current running through the wire follows as $I = U/R$. Figure 5.10 gives the mass of cabling per meter as a function of the current. As the current running through the cables is low, only the bottom-left part of the graph is relevant. This part can be approximated by a line with a slope of $0.0014 \text{ kg}/\text{m}\cdot\text{A}$. The length of the cables follows from the path that they need to follow back

and forwards, namely over the width of the spider, through the booms and finally to the instrument housing. To account for twists and turns, another 25% is added to the final length of cable. The final cable length is also a function of the heater power, because the boom and rod lengths are dependant on this power. Multiplying the current by the mass per current and the cable length gives the cable mass.

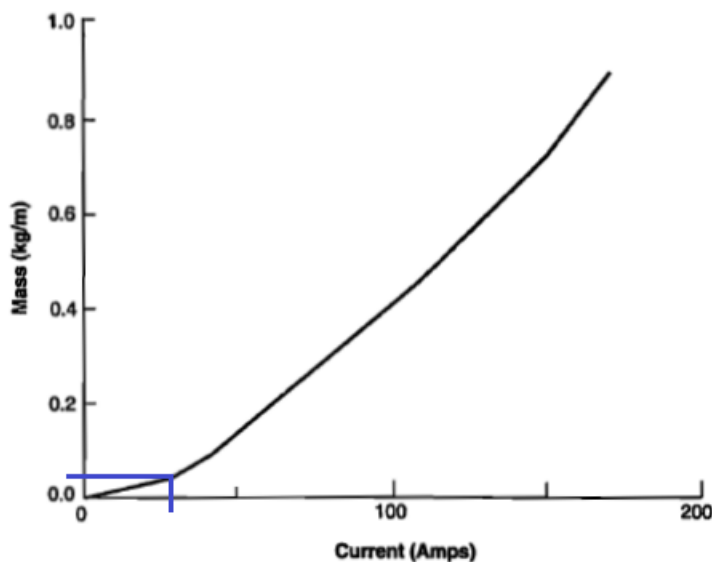


Figure 5.10: Cabling mass versus current through the cable. Retrieved from Larson and Wertz (2005).

The additional mass of the solar arrays can easily be found. Currently, triple junction gallium arside solar panels can reach a specific power of 108 W/kg.[56] This includes the solar cells as well as other additional components (wiring, glass, substrate). Note that this value only serves as an indication of what the total added mass of the system is, to enable comparison with other concepts. Other unknown factors, like solar panel orientation, also play a role. Such factors are to be considered in future work. The power consumption of the heaters follows from the power line voltage (U) and drawn current (I) by $P = U \cdot I$. The solar array mass then follows by multiplying this power by the specific power.

The geometry, heater, cable and solar array mass are all shown in figure 5.11. They are summed to get the total variable mass of the system utilising heated rods. For comparison, the mass of the passive athermalised system is shown as the horizontal line. It can be seen that with an applied heating power of 8 W, the variable mass of the heating system reaches a minimum of 0.2733 kg. This mass is expected to increase somewhat due to the added necessity of measuring the rod temperature.

Lastly, the temperature needs to be measured and controlled. Minco provides heaters with build in sensors, so these are already included in the heater mass. They provide Proportional/Integral/Derivative controllers for about 75 g per unit, combining these into a controller for all six rod heaters equals a controller mass of about 450 g.[55] This thus accounts for a total system mass of about 0.72 kg. The controllers provide control with a standard resolution of 0.1 K, which can be scaled up. With a standard resolution of 0.1 K the translational resolution directly follows from the length and CTE of the rods to be at most 0.2 μm . The expansion of materials by heating them is well understood, and with a good control system the secondary mirror can be stabilised with a high accuracy. It however comes with the significant disadvantages of added complexity, additional points of failure and power consumption.

5.2.3. Heating of booms

The process of heating the booms is opposite to that of the rods. Instead of adding extra heat while in sunlight to increase the maximum temperature, the heat is added in eclipse to decrease the temperature drop of the booms. The process in designing the boom heaters is however very similar to that of the rods. First, the time at which the heaters are turned on is identified. This is followed by multiple ESATAN runs to find the temperature response of the rods and other components to different heating

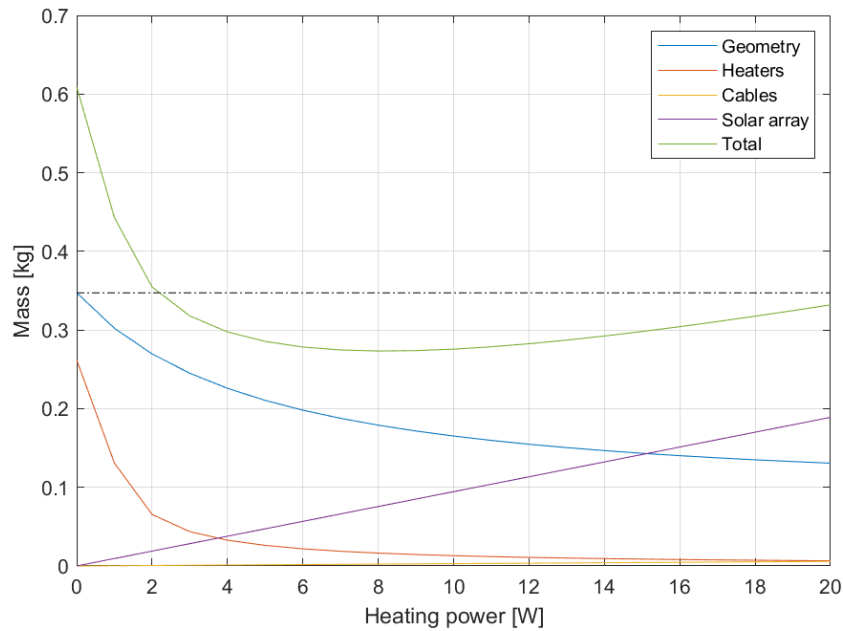


Figure 5.11: Added mass of the SMSS as a function of heating power.

power input. Then, the mass of the system is calculated.

The temperature and net heat balance of the booms without any heating applied is seen in figure 5.12a. The heat balance profile is more complicated than that of the rods because it fluctuates significantly. It is, therefore, harder to give a single time-frame in which the heaters should be turned on. Initially, the total heating power is set to be the opposite of the net heat balance of all booms and distributed evenly. This heating is only turned on when the net heat balance is negative, which is indicated by the area shaded in red. The resulting change in temperature and heat balance can be seen in figure 5.12b. The resulting behaviour is not entirely as expected. Even though the heat balance moves closer to zero, the average temperature increases and the temperature range decreases, the heat balance stays well below zero for a long time. Because the applied heat was set as the opposite of the heat balance of the booms, the resulting heat balance was expected to average around 0 W. Furthermore, the resulting temperature range decrease is minimal, with a change of about 0.5 K.

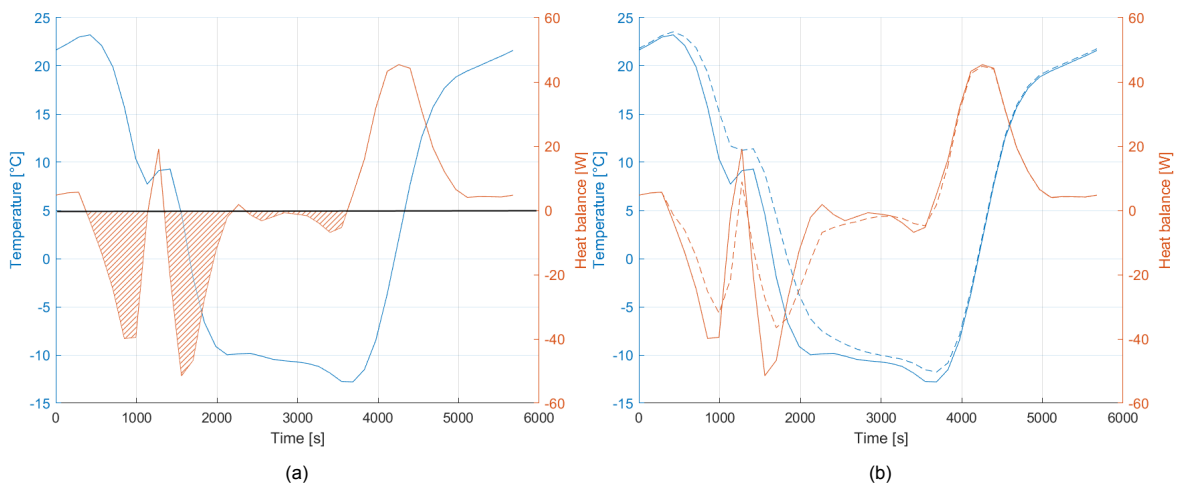


Figure 5.12: Temperature profile and net heat balance of the booms a) without and b) with heat applied.

Because the effect on the temperature range is so low, a different approach was used. Instead of using the summed heat balance of the four booms and evenly distributing the applied heat, the four

booms are treated individually. The applied heat is determined in the same way as before; however, the heat is now determined and applied per boom. The initial try, however, still did not result in the desired temperature range decrease. The temperature range only drops by about 0.7 K. The output of the first simulation is therefore used to iterate on the required heating power. The applied heat in the second iteration is then the sum of the applied heat in the first iteration plus the opposite of the heat balance found from the first iteration. This process is applied multiple times, for which the result can be seen in figure 5.13. It is clear that each iteration means an improvement over the previous iteration, but the response is still low. The resulting temperature ranges are plotted as a function of the total average applied heating power in figure 5.14. Even when an average heating power of 47.5 W is applied, the temperature range only decreases by 3 K. To gain any significant reduction in temperature range, heating in the order of hundreds of watts would be required. Additionally, the heating is applied during eclipse, which means batteries are required to provide power, further increasing the mass and complexity. Combined, these reasons make the concept not feasible and not further investigated. As stated before, cooling the booms would also be an option. However, space-borne Peltier elements have only been operated up to a few Watts.[31] The amount of power required to cool would be approximately the same as the amount to heat the booms, meaning an unrealistic amount of Peltier elements would be required. It can therefore safely be said that cooling the booms with thermoelectric coolers is also not feasible.

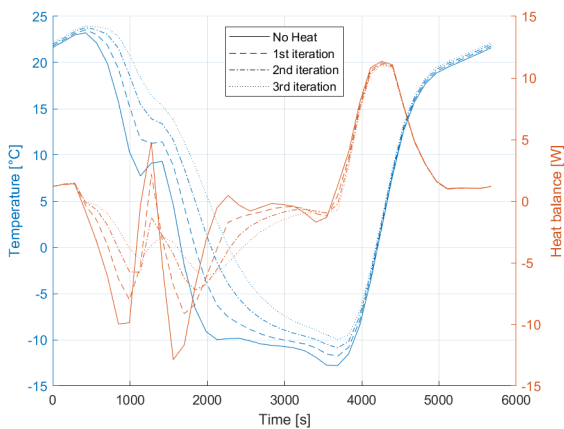


Figure 5.13: Temperature response of the booms to different levels of applied heat.

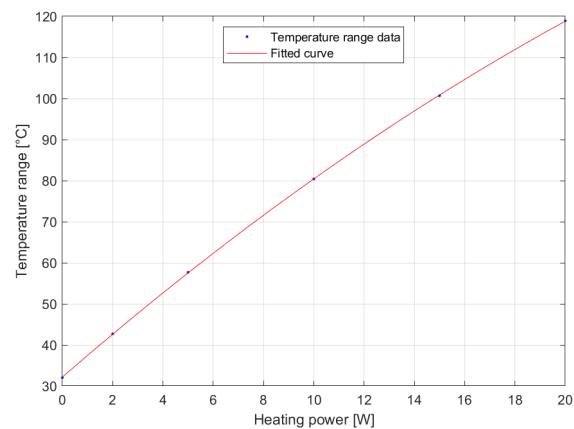


Figure 5.14: Polynomial fit of the temperature range of the booms as a function of the applied heat.

5.2.4. Quasi-active thermal control of rods

The quasi-active thermal control of the rods consists of applying coatings with changing thermo-optic properties. However, as is explained in section 5.2.1, the coating that is already used, namely magic black, already provides good properties regarding maximising the temperature ranges. To maximise the temperature range, the absorbed energy should be as high as possible during the sunlit phase, as low as possible during eclipse. Furthermore, the amount of released energy should be as high as possible during eclipse. Because of its high emissivity and absorptivity, the energy absorbed during sunlight phases is already maximised. During eclipse, the high emissivity means that the highest amount of energy is radiated from the surface, thus decreasing the minimum temperature. One possible improvement in its radiative properties is a low absorptivity during eclipse, which would mean less absorbed energy. However, as figure 5.15 shows, the primary source of visible light, the albedo heat source, is zero for a significant portion of the eclipse. Modulating the coating of the top-plate to have a low absorptivity during eclipse would therefore have a minimal effect. The potential gain lies in the shaded area, which is the start of the eclipse and thus the period where the temperature starts decreasing rapidly. If the absorbed albedo is decreased during this period, the temperature drops even more. The result of a simulation where 90% of this shaded heat is removed from the system, simulating an adaptive coating where the absorptivity goes to zero in this part of the orbit, is shown in figure 5.16. The influence on the temperature during this time is evident, as the temperature indeed drops more rapidly. The temperature is, however, quickly normalised after this initial drop. Overall, there is no net gain in temperature range. Moreover, electrochromic coatings are currently not even capable of achieving

such a high absorptivity modulation. This concept is, therefore, infeasible and not further analysed.

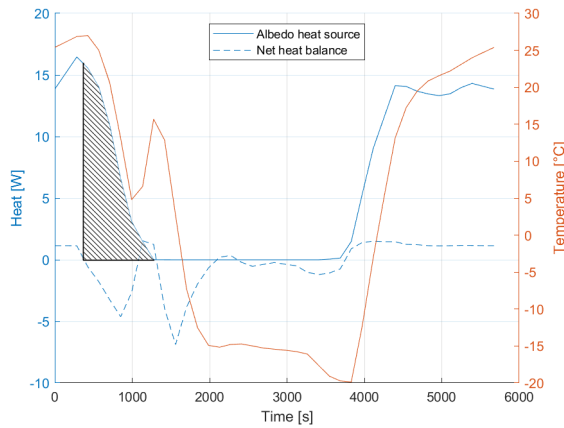


Figure 5.15: Temperature profile, net heat balance and impinging Albedo radiation of the rods.

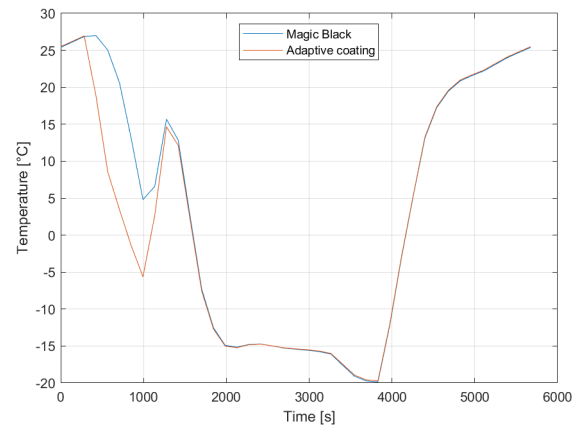


Figure 5.16: Temperature profile of the rods with and without adaptive coating.

5.2.5. Actuation of secondary mirror

In this concept, instead of controlling the temperature to keep the translation of the secondary mirror within the specified bounds, the translation of the secondary mirror is taken as input. It is used to find the required actuation of the secondary mirror. The translation of the secondary mirror is seen in figure 5.17. In spaceborne telescope structures, two main types of actuation for translating secondary mirrors are conventionally used, namely the hexapod drive and the eccentric drive. For the hexapod drive COTS products are available. This is not the case for the eccentric drive. The development of a stand-alone secondary mirror actuation system utilising an eccentric drive would be costly and time-consuming. The result would probably not be better than any COTS products currently available. For this reason, only COTS hexapods are taken into consideration.

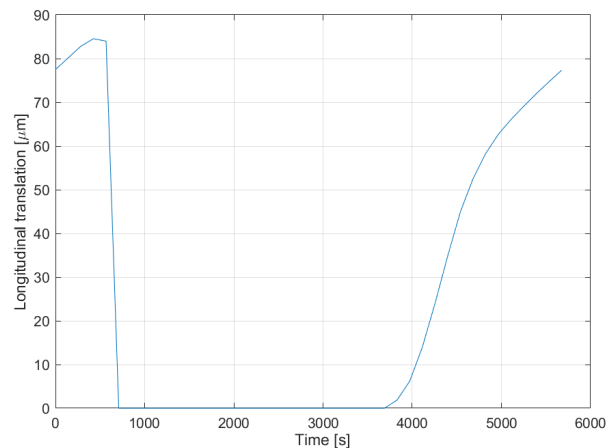


Figure 5.17: Longitudinal translation of the secondary mirror.

There are several COTS hexapod drives capable of achieving the requirements set on the positioning of the secondary mirror. Suppliers of hexapod drives include Physik Instrumente from Germany and Symétrie from France. The potential products and their main parameters are summarised in table 5.1. Here, the smallest products capable of achieving the required range of motion and accuracy within a space environment are considered.

These three products show that it is possible to achieve the fine positioning control required. They all have a high enough travel range and low enough resolution and repeatability to achieve positioning

Table 5.1: Parameters of three different actuators.

	NANOPOS [57]	Q-821 [58]	P-911KNMV [58]
Supplier	Symétrie	PI	PI
Mass [g]	505	550	?
Longitudinal travel range [mm]	4	3	1.5
Resolution [nm]	10	1	100
Repeatability [nm]	75	~ 60	~ 60
Operating range [K]	+ 4 to + 40	~ 0 to 50	~ 0 to 50
Size [mm]	Ø 70	80 x 73	Ø 100
Height [mm]	68	48	90

within the in-orbit and coarse alignment budgets. This is possible with hexapod drive masses as low as 0.5 kg. The height of the hexapod drives is around the same as that of the athermal rods, meaning the additional baffle and boom mass is about the same. Besides the hexapod drives themselves, controllers are required. Physik Instrumente and Symétrie can provide these with masses as low as 2 kg. Custom solutions might give a lower controller mass. Of course, these drives and controllers also consume power. However, because they are not operated continuously and do not have a very high power draw, this does not mean any significant increase in battery or solar array mass. Cabling, however, does need to be present, but as the analysis of the rod heating system cable mass shows, this mass is also low. In total, a system utilising hexapod drives has a mass around 2.5 kg.

5.2.6. Actuation of spider

Actuation of the entire spider can be achieved by placing actuators in between the deployment booms and the top CORE hinges. This provides for movement along the Z-axis and rotation around the X- and Y-axis. Because the translations along the X- and Y-axis and the rotation around the Z-axis are not expected to be critical, this is sufficient for this initial design phase. The rotation around the X- and Y-axis is harder to achieve than by using a hexapod, because the actuators are placed further away from the rotation axis. However, as is shown in the introduction, the maximum rotation around these axis is expected to stay within the budget so this should not pose a problem. Furthermore, if each actuator exactly compensates for the expansion of each deployment leg, the rotation can, in principle, be kept at zero.

The actuation can be achieved by means of different linear actuators. Linear actuators are commercially available from many suppliers. Some potentially viable actuators are summarised in table 5.2. Again, only the smallest products capable of achieving the required range of motion and accuracy within a space environment are considered.

Table 5.2: Parameters of four different actuators.

	P-841.6 [59]	L-220 V6 [60]	KeevoDrive® [61]	N-111.201 [62]
Supplier	PI	PI	Micromotion	PI
Mass [g]	62	200	19	245
Longitudinal travel range	90 μ m	26 mm	2 mm	10 mm
Resolution [nm]	1.8	550	310	0.025
Repeatability [nm]	?	1 μ m	350 nm	?
Operating range [°C]	-20 to + 80	5 to 40	- 35 to 70	0 to 55
Length [mm]	122	48	44	?

Of the actuators shown in table 5.2, the KeevoDrive® has the lowest mass, but the lifetime of 500 hours might be too low. The next best option regarding mass is the P-841.6. With a mass per unit of 62 g, the total actuator mass is 248 g. Integrating this too form a rigid connection to the booms and

CORE hinge requires additional parts, increasing the mass by about 50g. Additionally, a mount for the secondary mirror is required to remove thermally induced stresses. An excellent option to do this would, for instance, be by using a kinematic mount[3]. The mass of a kinematic mount is expected to be about the same as a passive hexapod mount, so about 150 g. Because the actuators are placed in series with the booms, the boom length is slightly shorter, decreasing their mass by about 75 g. Cabling is required for each actuator separately, but the mass is low, around 10 g. Physik Instrumente provides controllers with a mass of 400 g per unit, for a total of 1600 g. This means that a system with a mass of around 1900 g might be possible. There is, however, a big downside to using linear piezo actuators, which is their continuous power draw. The P-841.6 has a maximum voltage of 100 V with an average current of 0.06 A. Taking the average voltage, this means an average power consumption of 3 W per actuator with a total of 12 W continuously applied during sunlit phases. With a solar array specific power of 108 W/kg[56], this accounts for a mass increase of 0.11 kg. The total added mass of a system where the whole spider is actuated would thus be about 2.1 kg.

5.2.7. Concept conclusion

The concepts highlighted in green in figure 5.18 are the concepts that are potentially able to meet all requirements. With the parameters found in this section, the final trade-off can be performed in section 5.3.

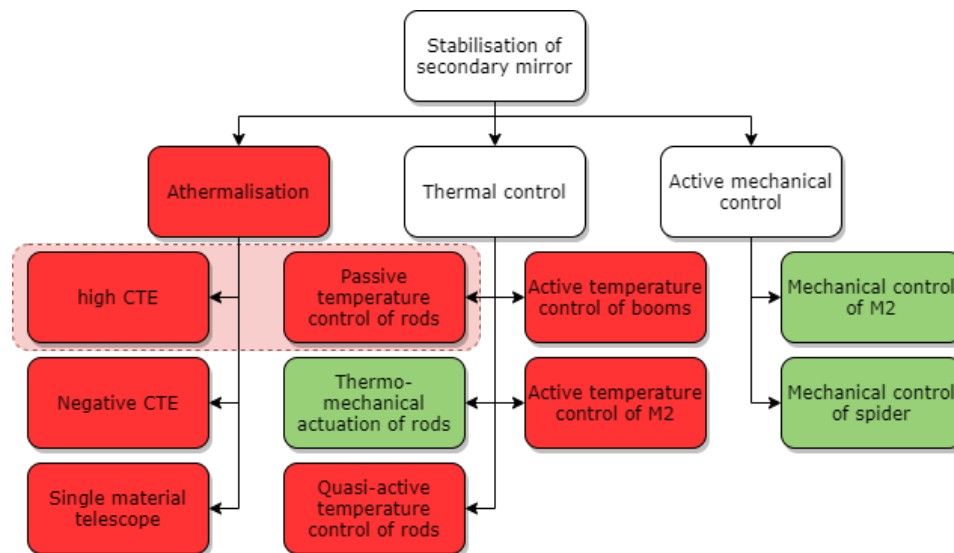


Figure 5.18: Design option tree of secondary mirror support structure with remaining concepts (green) and infeasible options (red).

5.3. Trade-off

To find the best concept to keep the secondary mirror stable, a trade-off is performed. The three concepts are traded-off using five criteria, namely the accuracy, mass, complexity, stiffness, volume and dynamic response. Here, the range of motion is not included because all concepts can achieve the required range of motion. The criteria are defined as follows:

1. **Accuracy:** The accuracy is defined as the ability of the concept to keep the translation and rotation of the mirror close to zero. This is amongst others determined by the resolution and repeatability.
2. **Complexity:** The complexity is defined by the amount of (moving) parts, the way in which these parts are integrated in the system and the ease by which these parts can be manufactured. Increased complexity means higher production costs and lower reliability.
3. **Mass:** The mass is simply defined by the mass calculated in section 5.2. The power consumption is included in the mass criterion in the form of for instance increased battery and solar array masses.

4. **Volume:** The volume is mainly defined by the longitudinal length of the concept. A higher length means a higher stowed volume.
5. **Stiffness:** The stiffness is determined by the strength and length of the components, and the way in which the components are connected to each other. A lower stiffness means a system that is more prone to vibrate, which increases the chance of vibrations with an amplitude that makes it impossible to keep the mirrors stable.
6. **Dynamic response:** The system should be capable of quickly responding to all changes in temperature. This means that the displacement or rotation of the secondary mirror caused by any positive or negative temperature change should be compensated for before the relevant budgets are exceeded.

The weight of the different criteria is determined using the Analytical Hierarchy Process (AHP). The AHP method is a useful tool and widely used to make multi-criteria decisions.[63] It is used to determine the relative figure of merit of different options by the pair-wise comparison of each option.[64] Firstly, the relative figure of merit for each trade-off criteria is determined. This is done by finding the relative importance of each pair of criteria. These are then placed in an n by n matrix, where the lower off-diagonal elements are the inverse of the upper elements. The relative figure of merits are then found by solving the eigenvector, which represents the weight of each option. The resulting weights are presented in table 5.3. The complexity and accuracy are found to be the most important, followed by the mass and dynamic response and, finally, the volume and stiffness. The consistency of the resulting weight vector is verified using the Consistency ratio (CR). The weights are consistent when this ratio is lower than 10%.[63, 64] In this case, the CR is 7.1%, which means the determined weights are consistent and therefore accepted.

Table 5.3: Trade-off weights for deciding the best concept to stabilise the secondary mirror.

Criterion	Weight
Accuracy	0.213
Complexity	0.282
Mass	0.151
Volume	0.132
Stiffness	0.075
Dynamic response	0.147

5.3.1. Graphical trade-off

The easiest way to perform a trade-off, if possible, is by means of a graphical trade-off. In graphical trade-off tables, outliers and clear winners can easily be identified. The graphical trade-off table is presented in figure 5.19. The graph contains five colours, each representing a different score. Green means excellent performance, blue means good performance, yellow means acceptable performance, orange means that clear deficiencies are present and red means that the score is unacceptably low. The height of the rows represents the weight of the criteria. The rationale for the scores is presented below.

Accuracy

With a resolution of $0.2 \mu m$ and a high repeatability, Concept A is capable of keeping the secondary mirror within the stated budgets, but not by a wide margin. Concept B can provide translation and rotation of the secondary mirror with high accuracy in all six degrees-of-freedom. Concept C allows for excellent longitudinal translation resolution, but not for good angular resolution, but it cannot provide lateral movement and rotation around the z-axis. These movements are, however, not expected to be required, and probably are not even measured. This means that Concept C can provide all the required actuation with the same accuracy as concept B, giving them both an excellent score.

Complexity

Concept A is the most simple, because it does not have any moving parts. It does, however, require heaters, sensors, control algorithms and draws power. It therefore scores good. Concepts B and C score the lowest. They employ moving parts, which inherently are more subject to failure. Concept B requires intricate control algorithms. Concept C is easier to control but requires more cabling and separate control because the actuators are placed in different positions.

Mass

The score on mass simply follows from the added masses calculated in section 5.2. With a mass of 0.72 kg, concept A has the lowest mass and scores high. With masses of 2.5 and 2.1 kg respectively, concept B and C have relatively high masses, thus giving them the lowest score.

Volume

Concept A and B have a longer boom length than C meaning they have a higher total stowed volume. Their volume is however not too high, giving them a good score and concept C an excellent score.

Stiffness

Geometrically, concept A and B are about the same. Because they add length to the booms, the stiffness of the booms goes down. The rods reduce the stiffness further as they provide an additional mode of vibration. Concept C requires actuators to be placed in between the booms and the top CORE hinge. Done adequately, this should not reduce the stiffness significantly. Because the booms are shorter for concept C than for both other concepts, it scores the highest.

Dynamic response

Concept B and C are both capable of providing all required actuations quickly, making them both score excellent. Concept A can provide nominal control of the mirror. However, in the case of off-nominal temperature variations, for instance, with sudden temperature drops, Concept A relies on the passive radiative and conductive properties of the rods to cool down. As the satellite experiences differing albedo and IR radiation from Earth every orbit, these off-nominal temperature variations are expected to happen and are indeed found in a separate ESATAN analysis. This means that Concept A cannot provide actuation quick enough to keep the secondary mirror within all budgets, which is unacceptable.

Graphical trade-off table

Concept A scores good at all criteria but shows unacceptable dynamic response which rules it out as a contender. Concept B and C score the same on most criteria, except for volume and stiffness where concept C scores better. These are, however, not very important criteria, as seen by their relative height in the graph. The graph, therefore, suggests concept C to be the winner. However, because the differences are small and found in the two least important criteria, no conclusive decisions can be made from this table. To find the unbiased winner, a further numerical trade-off is performed in section 5.3.2.

Concepts	A. Rod thermo-mechanical	B. M2 Mechanical control	C. Spider mechanical control	
Criteria				
Accuracy	B	G	G	
Complexity	B	Y	Y	
Mass	B	Y	Y	
Volume	B	B	G	
Stiffness	B	B	G	
Dynamicity	B	B	G	

	Green	Excellent
	Blue	Good
	Yellow	Neutral
	Orange	Clear Deficiencies
	Red	Unacceptable

Figure 5.19: Graphical trade-off table for deciding the best concept to stabilise the secondary mirror.

5.3.2. Numerical trade-off

The numerical trade-off consists of grading the concepts on their performance on all five criteria. To ensure that the results are correct, this is done in two ways. Firstly, by grading the concepts on a 1-5 scale and secondly by finding the relative merit of the concepts per criterion by using the AHP method. By multiplying the weight and the scores and summing the result, the total score is found. The results are shown in table 5.4. Both scoring methods show that concept C scores the best. What's more, a design criterion which was not considered in this trade-off is the induced stresses in other parts. Because the actuators used for the actuation of each spider leg keep the spider "level", no stresses are build up in the spider legs. If the booms are allowed to expand individually, each leg would be at a different z-coordinate. Because the system consists of four booms, it is overconstrained. A different translation of each spider leg would therefore create stresses in the spider. This is thus largely avoided by using actuators on each deployment leg. With the graphical and numerical trade-off both showing that concept C, the mechanical actuation of the entire spider, is the winner, and the fact that the induced stresses are minimised, concept C can confidently be advanced to the detailed design phase. The detailed design of the concept providing actuation for the entire spider is presented in chapter 6

Table 5.4: Numerical trade-off of three concepts.

	Weight	1-5 Grade		AHP score	
		Concept B	Concept C	Concept B	Concept C
Accuracy	0.213	5	5	0.513	0.487
Complexity	0.282	3	3	0.489	0.512
Mass	0.151	2	3	0.455	0.545
Volume	0.132	4	5	0.476	0.524
Stiffness	0.075	3	4	0.455	0.545
Dynamicity	0.147	5	5	0.455	0.545
Total Score		3.70	4.06	0.479	0.521

6

Detailed design

This chapter presents the detailed design of the three main parts of the design. Firstly, in section 6.1 the design process for actuating the secondary mirror is discussed. Section 6.2 then presents the steps taken to find and design the best concept to measure the displacement of the secondary mirror. Finally, in section 6.3, the best way to mount the secondary mirror to the spider is selected and designed. Each section individually consists of first selecting the different methods by which the primary purpose of the part can be accomplished. The designs based on these different methods are then outlined, which is followed by a trade-off to determine the final design of each part.

6.1. Actuation

The actuation system, as described in section 5.2.6, was a conceptual one, merely used to find initial estimates of the mass and power consumption of the different secondary mirror concepts. Here, the system is designed in detail. Multiple actuators and their performances are described, after which the best one is chosen. To actuate the spider, four individual actuators are placed at the end of each deployment leg, in between the boom and the CORE hinge. Another location could be between the root CORE hinges and the booms, but this requires more force because the moved mass is larger. Placing the actuators at the root of the booms however comes with the advantage that the cables do not have to run through the booms. At this stage in the design, it is not known if, or indeed how many, cables can run through the booms without hindering the deployment of the mid-hinge. It is therefore for now assumed that the actuators are placed at the top of the booms. If future analysis shows that this significantly hinders the functioning of the expansion booms, moving them to the root of the booms should not pose significant problems besides perhaps a change in actuator. The actuators are placed below the top CORE hinges, because for the CORE hinges to function properly, they have to be directly attached to the spider.

In choosing the right actuator, a few key parameters must be kept in mind. The following list of minimum requirements is used in determining whether an actuator is potentially viable:

- To allow for translational sensing errors, the accuracy of the actuator must at least be **1 μm** .
- The stroke of the actuators should at least be **90 μm** , in line with the maximum secondary mirror translation found in figure 5.17.
- The push/pull F of each actuator should at least be **0.12 μN** . This is derived from the mass of the spider and the time required to provide the actuations via $F = m \cdot a$. With a maximum required translational speed of the mirror of 0.07 $\mu m/s$ and a preliminary resolution of 0.1 μm , the required actuation is about 0.1 μm per second. This requires a maximum acceleration (a) of 0.2 $\mu m/s^2$. The combined movable mass, so the mass of the top CORE hinges, the spider, secondary mirror and secondary mirror interface, is 2.4 kg.
- During launch, the actuators have to withstand forces of $F = m \cdot a = 2.4/4 * 30 * 9.81 = \mathbf{176.6 N}$. This value is derived from requirements M2-MEC-25-01, M2-MEC-25-01 and M2-MEC-25-01 in appendix A, which specify the launch loads to be 30 g in the X, Y and Z directions.

- The motor must survive the temperatures experienced during LEOP and operate at temperatures of around **-20 to + 50 °C**, as found from the thermal results presented in chapter 4.

6.1.1. Actuator types

The different design options and initial conclusions are in large part based on the primary mirror positioning actuator selection for the DST performed in Pepper (2018). The requirements posed on the actuators are mostly analogous to those posed on the actuators in Pepper (2018). They differ slightly because the secondary mirror actuation requires a lower accuracy but a higher stroke compared to the PMAO. The initial analysis is, therefore, also mostly analogous and reused in this work. The difference lies in the final actuator selection.

Four types of different actuators are defined, being electrical, piezoelectric magnetic and phase-change actuators. These four different types are sub-divided in multiple different motors, as visualised in figure 6.1. Of these motors, the red-shaded ones are initially ruled out. The stick-slip piezoelectric stepping motor and both phase change motors are not yet proven to operate in the harsh environment of space, and thus not considered a feasible option. Voice-coil motors are not considered feasible because they require power for both stiffness and stability of the motor, which causes significant issues for both the thermal control of the motors and power requirements for the motors.[2] Lastly, Direct Current (DC) motors are ruled out because they are considered to have much of the same traits as electrical stepper motors, but worse because they require additional position sensors and are best suited for continuous operation instead of move and hold duties, as foreseen for the spider actuation.[2, 65] The remaining options are electrical stepping motors, linear piezoelectric motors and piezoelectric inchworm stepping motors. Concepts using these motors are presented below.

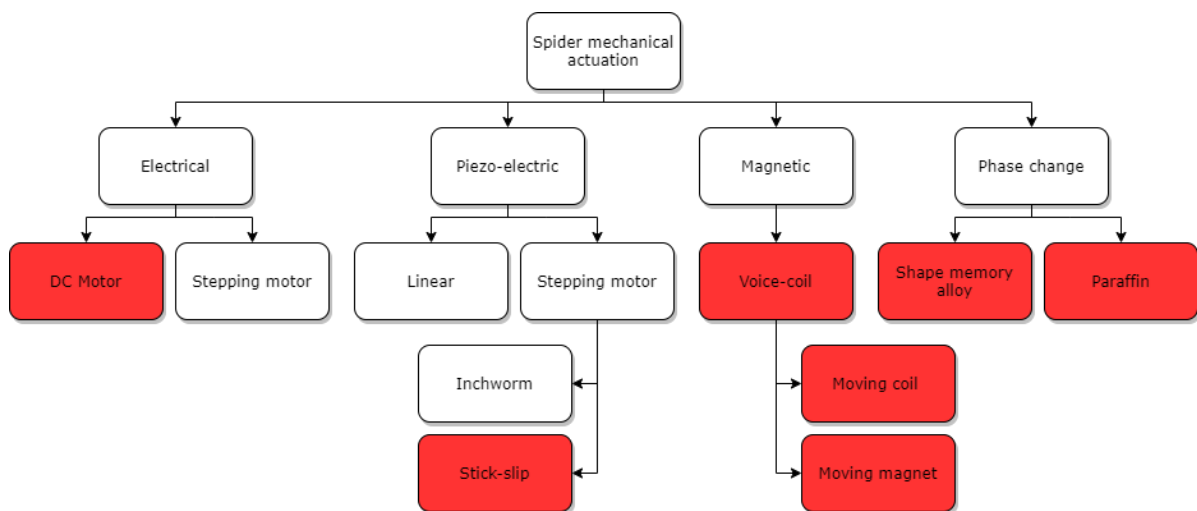


Figure 6.1: Actuator Design Option Tree. As adapted from Pepper (2018)

Electrical stepping motor

Stepper motors are a type of electromechanical brushless motor. They convert digital pulse inputs into discrete angular output motions of uniform magnitude rather than continuous motion. Each pulse steps the rotor shaft to a new precise position and latches it magnetically in this position. There are three types of stepper motors, namely permanent magnet and variable reluctance motors and a combination of both. Permanent magnet steppers can hold their position without being powered if the external torques do not exceed the detent torque of the motor, whereas variable reluctance motors can only hold their position when they are powered. The hybrid version is used when very fine steps are required, but the output torque is more variable than that of the other two motors. Stepper motors have lower torque capabilities than other motors, can have backlash, are comparatively large and require lubrication. However, their capability for very high-resolution control still makes them the most sought after solution for space mechanisms. They do however require gearing to provide for linear actuation.[66]

Space-rated stepper motors, in combination with rotary to linear-conversion gearing, are available from several suppliers, but precise numbers of the resulting linear repeatability and total mass are hard to obtain. Phytron provides some stepper motors suitable for high-vacuum and space applications. The LA 25.200.1.2 is a linear actuator assembly rated for high-vacuum and extreme temperatures[67]. Even though this particular actuator is not space-rated, it is very similar to their phySPACE™ space-rated actuators and therefore considered to be a good starting point to estimate the parameters for the actual space actuators[68]. The linear actuator assembly can provide positioning accuracy of up to 0.01 mm. This is not nearly enough, so additional gearing is required. This gearing can be included in the form of a 5:1 planetary gear stage.[67] Including two of those, as visualised in figure 6.2, increases the accuracy by 25 to 0.4 μm .

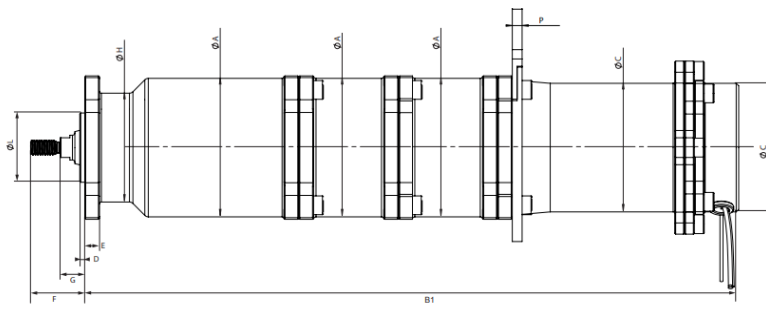


Figure 6.2: Linear stepper assembly with 25:1 gearing. As adapted from Phytron GmbH (2018)

Phytron provides actuator controllers with all required specifications, of which the most suitable is the APS[69]. Four of these are required, resulting in a total controller mass of 64 g. With a motor current of 1.2 A and an operating voltage of 24 V, the power draw during operation is 28.8 W. However, the power is only drawn for short durations. The maximum speed of the assembly is 0.06 mm/s. Such speeds are however not required. Even with a speed of 0.01 mm/s, a translation of 0.1 μm only takes 0.01 s. Because the controller can provide the required short power pulses, the average power consumption is taken to be the wattage required for one movement divided by 1 second. This results in a power consumption for one actuator of 0.288 W.

The results is a linear stepper motor assembly, as visualised in figure 6.2, with a total added mass of 474 g, a power consumption of 1.152 W, a diameter of 28 mm (A in the figure), an initial length of 133.1 mm (B1 in the figure), a maximum force of at least 30 N, a maximum speed of 0.06 mm/s, a stroke of 13 mm and finally an accuracy of 0.4 μm . A disadvantage of using this linear electrical stepping motor is its length. The actuator assembly effectively replaces part of the boom. This actuator is made mostly out of aluminium parts with a CTE of 23.6 $\mu\text{m}/\text{m}\cdot\text{K}$, which means an increase of 22.8 $\mu\text{m}/\text{m}\cdot\text{K}$ in CTE over the length of the actuator assembly. In the worst-case scenario, this would cause an increased translation of the secondary mirror of 112.6 μm . The phySPACE™ actuators also come with the option to be made from titanium, which would decrease this additional translation to 39.5 μm . This issue is worsened slightly by the power dissipation of the motors. The temperature differences caused by an average motor dissipation of 0.072 W are found from ESATAN to be small but significant. The average maximum boom temperature is found to increase by around 0.065 K, while the average maximum top CORE hinge temperature is increased by around 0.51 K. This respectively causes additional expansions of 0.08 μm and 0.33 μm , for a total of 0.41 μm . This would mean that the total added translation due to a linear stepper motor is 113.0 μm when the conventional aluminium actuators are used or 39.9 μm when the titanium version is used. With a total stroke of 13 mm, both do not cause problems in this regard. However, the additional translation does need to be measured, which might pose additional problems. Furthermore, the actuation itself might cause vibrations in the secondary mirror. Both issues can be accounted for, but certainly might present undesired additional design issues.

Linear piezoelectric motor

Piezoelectric motors are typically made of a thin solid material with electrodes deposited on opposing faces. They operate on the principle of the inverse piezoelectric effect. When a voltage is applied to the electrodes, they induce a strain which results in solid deformation. They feature high displacement accuracies, can produce large forces and have a high response speed. A piezoelectric actuator is usually rigidly connected to the component being displaced, which adds stiffness. Linear piezoelectric motors have a major disadvantage because they require continuous power to hold their position.[70] They also have significant advantages in the fact that they can provide high resolution without transmission and can be designed to survive launch without the use of an Hold-Down & Release Mechanism (HDRM).[2]

Two different viable linear piezoelectric motors were identified, the first one being the P-841.6 from Physik Instrumente and the second one the APA100M from Cedrat technologies. Their relevant parameters are summarised in table 6.1. They both meet all prerequisites. The accuracy of both actuators is not explicitly mentioned, but with a good closed-loop positioning control algorithm accuracies nearing the resolution can be reached. Both have a resolution of about 1 nm, so both can reach very high accuracies. The differentiation between both actuators lies in the fact that the APA100M has a lower mass but a higher input voltage. However, because the input voltage is already above the nominal satellite voltage of 28 V[54], a conversion has to be applied anyway, meaning the higher input voltage of the APA100M is not of much importance. Furthermore, the APA100M is much shorter in length. Because the actuators have a much higher CTE than the booms, the total translation of the secondary mirror is increased by both actuators. To minimise this increase in translation, it is preferable to have an actuator with a lower length. For these reasons, the APA100M is selected to be the linear piezoelectric motor to enter the actuator trade-off.

Table 6.1: Data of the P-841.6 and APA100M linear piezo actuators. Data retrieved from respectively Physik Instrumente (PI) GmbH & Co. KG (2020) and Cedrat Technologies (2014).

	P-841.6	APA100M	
Travel range	90	126	μm
Resolution	1.8 / 0.9	1	nm
Push/ pull capacity	1000/ 50	234.5/234.5	N
Mass	62	19.5	g
Length	122	25.0	mm
Input voltage	0 to 100	-20 to 150	V
Lifetime		$> 10^{10}$	cycles

Because the input voltage of the APA100M is above the nominal satellite voltage, the actuator system requires a step-up converter. In the selection of the piezo controllers, it is important to know the maximum current draw of the piezo actuator. The maximum current is calculated as shown in equation (6.1)[72]. Here, C is the capacitance of the actuator and dV/dt the change in voltage over time. The capacitance of the actuator is provided to be $3.15 \mu\text{F}$ [71]. The maximum change in voltage over time is defined by the voltage range and stroke of the actuator and the required translational speed. The maximum required translational speed is determined in section 6.1 to be about $0.1 \mu\text{m/s}$. With a total stroke of $126 \mu\text{m}$ and a voltage range of -20 to 150 V, the voltage change required to provide $1 \mu\text{m}$ translation is 1.35 V . This means that, to achieve a speed of $0.1 \mu\text{m/s}$, dV/dt has to be 0.135 V/s . The maximum required current then follows to be $0.425 \mu\text{A}$.

$$I = \frac{dQ}{dt} = C \frac{dV}{dt} = 3.15 \cdot 10^{-6} \cdot 0.135 = 0.425 \mu\text{A} \quad (6.1)$$

With a maximum voltage of 150 V and a maximum current of $0.425 \mu\text{A}$, the maximum power draw of one actuator is $63.75 \mu\text{W}$. The hold power is not precisely known, but it is known to be only necessary to compensate for the very low leakage currents, and correspondingly only a fraction of the maximum power required for a position change[72]. The hold power is, therefore, also assumed to be negligible. Cedrat Technologies provides several controllers for piezo actuators, of which the CCBu20 is the most suitable. With a maximum output current of 30 mA, it can easily provide the required current for the actuators. It can serve two channels, meaning that two of them are required to serve all four actuators.

The mass and power consumption are 250 g and 5 W respectively per piece, which totals 500 g and 10W.[73] Both values are relatively high for a controller that only needs to provide output currents of $63.75 \mu W$, and can be reduced by a custom design. Such a tailored design will look somewhat similar to the design shown in figure 6.3. This electronics board is explicitly designed to control a hexapod piezo actuator for a very high accuracy pointing system[74]. Without going into detail about which exact electronics will be used in the custom controller, we know the controller can be made lighter than the electronics board described in Defendini et al. (2000), because it requires less in- and outputs and because the used electronics in the custom design will be of a newer and more efficient design. The controller used in Defendini et al. (2000) has a mass of 50 g, so it can safely be assumed that the custom controller, in this case, will be lighter than 50 g. The power consumption of the actuators combines to at most $255 \mu W$. In assuming a voltage up-converter efficiency of 75%, the required input power is $340 \mu W$. The electronics of the board however also require power, for which an idle load of 1 W can be assumed (personal communication, J. Bouwmeester, 16 August 2020). With an actuator power consumption as low as $340 \mu W$, the total power consumption of the actuator system is then also 1 W. Such a power load is in line with the power consumption of the electronics board described in figure 6.3, which requires a power supply lower than 1 W fro a 28 VDC unregulated bus[75].

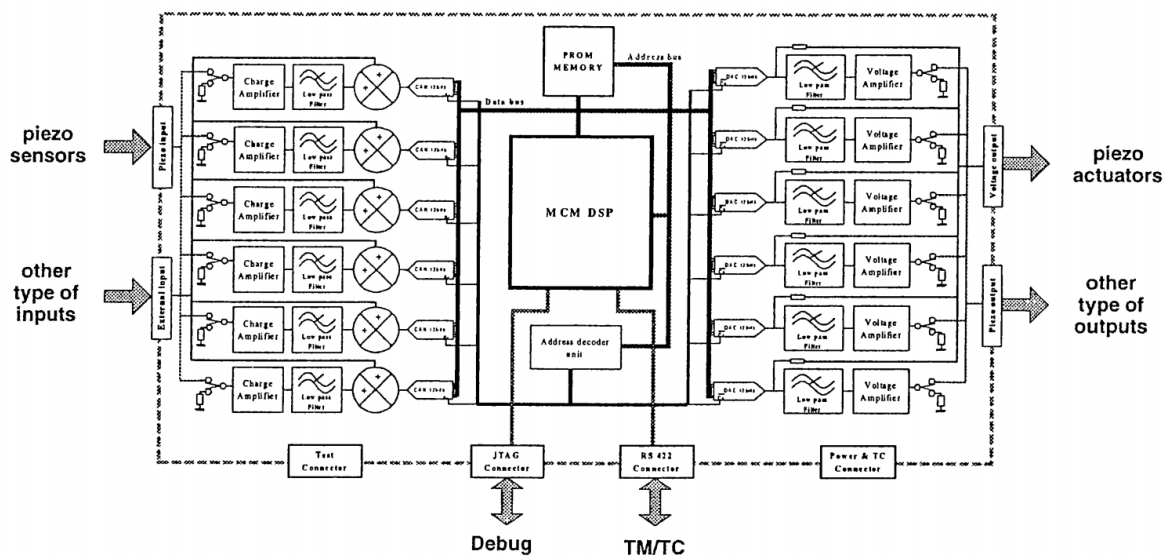


Figure 6.3: Piezo hexapod controller. Retrieved from Defendini et al. (2000).

The accuracy of the actuators depends on a lot of factors, such as hysteresis, drift, creep, gain and also vary with temperature. However, with a good closed-loop positioning control algorithm, the error in positioning can be reduced down to the resolution of the actuator within milliseconds, as shown in figure 6.4. The achievable resolution of the APA100M is, while taking into account an amplifier SNR of 85 dB, equal to 7 nm.[76] This means that the achievable accuracy is 7 nm.

Summarising, the total added mass of the actuator system is equal to 220.6 g, the power draw is 1 W and the accuracy is very high at 7 nm.

Piezoelectric inchworm stepping motor

Inchworm style piezoelectric actuators operate by means of the alternating expansion and contraction of at least two sets of piezoelectric stacks in contact with a driven runner, as visualised in figure 6.5. They are not as stiff as linear piezoelectric motors when clamped because they rely on friction, but they do provide power-off hold. An HDRM is required to survive launch forces.[2].

Although no piezoelectric stepping motor that meets all requirements is found, the Physik Instrumente N-310.10 is the closest possible fit. It has a travel range of up to 10 mm, resolution of 0.03 nm, 10 N push/pull force and 12 N holding force and an operating temperature range of 0 to 50 °C. Although the maximum permissible force is not explicitly mentioned, similar Physik Instrumente piezoelectric stepping motors specify a maximum lateral force of 10 N[78]. With assumed launch loads of

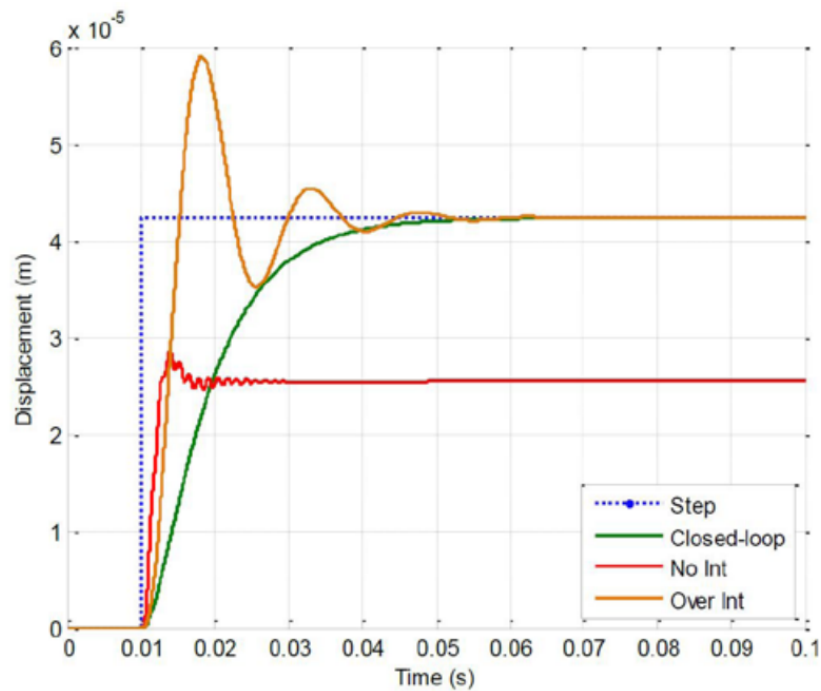


Figure 6.4: Step response of a piezo actuator with and without optimised PID closed loop. Retrieved from Cedrat Technologies (2019).

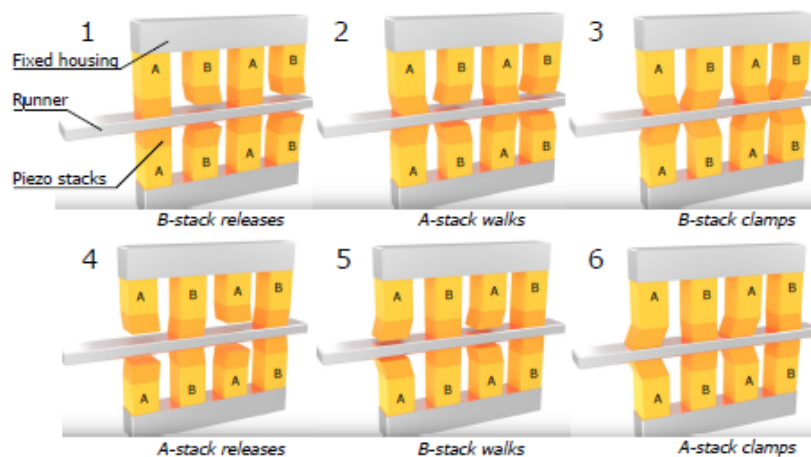


Figure 6.5: Example of a walking drive inchworm style piezoelectric actuator. The different piezoelectric elements expand and contract alternately to provide linear motion. Retrieved from Pepper (2018) as adapted from Physik Instrumente. (2020).

18 N, this is too low. This, combined with the fact that the temperature range is not sufficient, means piezoelectric stepping motors are not further considered a viable option to provide the spider actuation.

6.1.2. Actuator trade-off

The trade-off in actuators is between the Phytron LA 25.200.1.2 linear electrical stepping motor assembly and the Cedrat Technologies APA100M linear piezoelectric motor. The respective (system) parameters are shown in table 6.2.

The graphical trade-off table is presented in figure 6.6. Not all prerequisites posed on the actuators as stated at the start of this section are used in the trade-off, because they were mainly used as selection criteria for determining the viable actuators. The criteria used for the trade-off are the complexity, mass and accuracy of the concepts. Overall, concept A has some obvious disadvantages. Concept B scores much better regarding its complexity and accuracy, and only scores slightly lower in

Table 6.2: Actuator comparison.

	A. LA 25.200.1.2	B. APA100M	
Total mass	476.7	670.6 g	g
Stroke	13	126	mm / μm
Length	133.1	25.0	
Accuracy	0.4	0.007	μm
Push/ pull capacity	>30	234.5	N
Power consumption	1.152	10	W
Lifetime	$> 20 \cdot 10^6$	$> 10^{10}$	cycles

the power department. Concept B, the linear piezoelectric APA100M actuator, is therefore chosen to be used to provide the necessary actuation of the secondary mirror. Another advantage not previously mentioned is the fact that linear piezo actuators can provide active damping to vibrations.[79] Because the amplitude and frequency of the experienced vibrations during operation are not known, and their classification is not part of this thesis, it is not known whether linear piezo actuators are capable of damping the vibrations in the SMSS. It might, however, be worth investigating in future work, as further explained in chapter 9. The rationale for the scores is presented below.

Concepts	A. LA 25.200.1.2	B. APA100M	
Criteria			
Complexity	Y	G	
Mass	G	G	
Accuracy	Y	G	
Power	G	B	

Green	Excellent
Blue	Good
Yellow	Neutral
Orange	Clear Deficiencies
Red	Unacceptable

Figure 6.6: Actuator trade-off.

Complexity

The actuators of concept B are readily available, and integration within the telescope is simple. It, therefore, scores excellent. For the actuators of concept A, this is not the case. They already need some modification from the manufacturer, and they also affect other parts of the design. Due to the high length and high CTE of the assembly and its power dissipation, the translation of the secondary mirror is increased. This means more stringent requirements on the displacement sensing concepts are placed. In the final design, the vibrations caused by the actuators must also be accounted for. Concept A, therefore, scores much lower than concept B.

Mass

A quantitative scoring scheme for the mass was set-up where the SMSS mass budget was taken as reference point, as shown in table 6.3. The mass of both concepts is below 5% of the total SMSS mass budget, giving them both an excellent score.

Accuracy

Concept B can reach an accuracy of 7 nm within milliseconds, making it score excellent. Concept A has an accuracy of 0.4 μm . Even though this is enough, it is not exceptionally high. Concept A therefore scores neutral.

Table 6.3: Quantitative mass scoring scheme. Percentages are relative to total system SMSS mass budget of 14 kg.

0 - 5%	5 - 10%	10 - 25%	25 - 50%	>50%
0 - 0.7 kg	0.7 - 1.4 kg	1.4 - 3.5 kg	3.5 - 7 kg	>7 kg
Excellent	Good	Neutral	Clear deficiencies	Unacceptable

Power consumption

A scoring scheme similar to that set-up for the mass is set-up for the power. However, with no formal power budgets set-up for the entire DST, the score is harder to determine. In this case, the typical power consumption of small satellites is taken as a reference. From Larson and Wertz (2005), we know that a typical small satellite has a total power consumption of 200 W, with the payload consuming about 20% of that. Because of the non-traditional nature of the DST, this payload power consumption might prove wrong; it does, however, provide a good reference point on which the scores can be based. The relative scores are then calculated as shown in table 6.4. The power consumption of concept A is very low at 1.152 W, making it score excellent. Concept B scores neutral, with a power consumption of 10 W.

Table 6.4: Quantitative power scoring scheme. Percentages are relative to average small satellite payload power consumption of 40 W[54].

0 - 5%	5 - 10%	10 - 25%	25 - 50%	>50%
0 - 2 W	2 - 4 W	4 - 10 W	10 - 20 W	>20 W
Excellent	Good	Neutral	Clear deficiencies	Unacceptable

6.2. Measuring the secondary mirror translation

To enable proper control of the actuators, the amount of actuation required has to be known precisely. Whereas the deformable mirror is controlled via a stochastic descent algorithm, which iteratively focusses the mirror by random position adjustments to find the optimum solution, this is not possible for the secondary mirror actuators. The number of degrees-of-freedom (translation and rotation) makes it exceedingly hard to find the optimum solution. The process of finding the correct displacement for all four actuators through a stochastic descent algorithm would be time-consuming. Because the secondary mirror needs to be relocated several times during orbit, this would mean the telescope goes out of focus a significant portion of the time during which the telescope should be imaging (personal communication, D. Dolkens & H. Kuiper, 29 July 2020). This behaviour is unacceptable, meaning that the absolute position and rotation of the secondary mirror have to be known. In this case, because each actuator compensates for the expansion of one of legs of the deployment mechanism, the exact longitudinal expansion of each leg has to be measured. This can be measured in different ways, for which the concepts are presented in section 6.2.1. These concepts are then traded-off in section 6.2.2. Note that some estimations made in this section are very sensitive because of the lack of information. The trade-off in itself is, therefore, also very sensitive. Further design developments in future work might significantly change the trade-off parameters.

6.2.1. Sensing concepts

To find the exact longitudinal expansion of the deployment legs, two main methods can be used, as shown in figure 6.7. Firstly, the translation can be calculated by measuring the temperature along the length of the legs and converting this to the expansion of the material using equation (2.3). Such measurements are typically done using either thermocouples or thermistors. Other sensors, such as Integrated Circuit (IC) and Fibre Bragg Grating (FBG) sensors are also possible. However, IC sensors have no space heritage and thus a low Technology Readiness Level (TRL). Because their TRL is low and they do not provide obvious advantages over other types of sensors, they are not considered here. Furthermore, thermocouples typically are larger and heavier for the same performance than thermistors[80], meaning that only thermistors and FBG sensors are considered. Secondly, the displacement can be found by measuring the material strain. This measurement can be done by either

using strain gauges, piezoelectric sensors or FBG sensors. Piezoelectric sensors, however, suffer from distinct long-term stability issues, making them infeasible for space-applications[81]. Thirdly, the displacement can be measured directly employing either laser interferometry or cameras. The five remaining concepts, as shown in figure 6.7, are described, and initial estimates on the mass and accuracy are made.

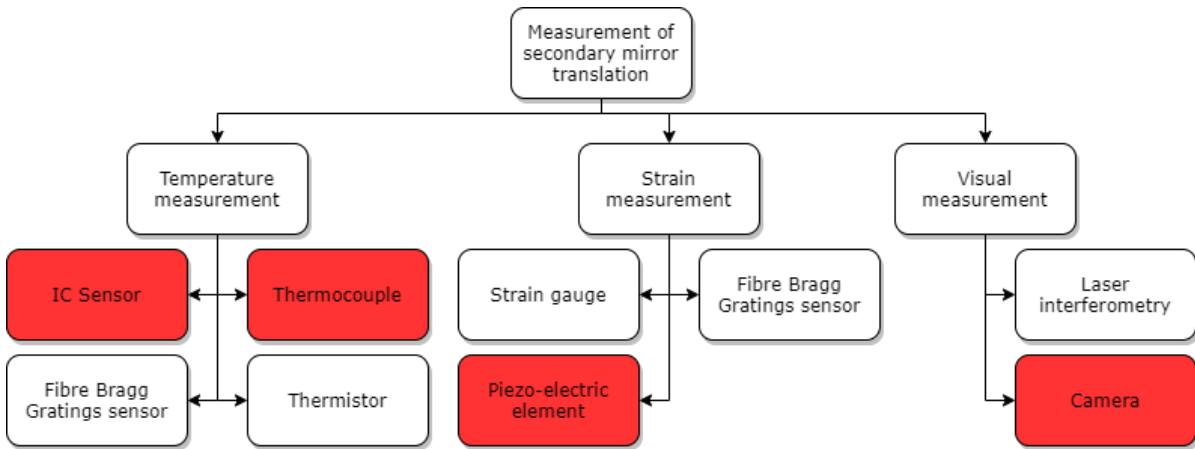


Figure 6.7: Design Option Tree for finding the best concept to measure the secondary mirror translation.

Temperature measurement

For most pure materials, the process of expansion and contraction is mostly linear and predictable. This is however not the case for CFRP materials, as shown in figure 6.8. Figure 6.8 shows the first couple of thermal cycles of expansion and contraction of a CFRP specimen. Even after multiple cycles, significant hysteresis is seen when the temperature decreases. Even though the temperature mostly increases during the sunlit phases, meaning that during imaging the translation is mostly linear, analysis has shown that there are also periods where even in the sunlit phase the temperature of the booms decreases. This hysteresis in thermal expansion and contraction can lead to errors in strain prediction of up to 5% of the total strain.[82, 83] The total expansion of the booms is about $50 \mu m$, meaning the error due to hysteresis of the expansion and contraction of the booms can get as high as $2.5 \mu m$. Even without taking into account errors from other sources, this is already too much. This means that calculating the translation of the secondary mirror by measuring the temperature of the booms is not an option. This applies to both the concept utilising thermistors and FBG sensors.

Strain gauge

The optimum amount and location of strain gauges is a question of mass and complexity versus accuracy. Note that, in this discussion, the required number of sensors is still determined by the temperature values as found from the ESATAN simulations. However, because the strain is measured directly, the measurements are not influenced by the hysteresis in the expansion of the booms. Firstly, the expansion of the deployment booms. The longitudinal temperature distribution of one of the booms at seven time-steps throughout the orbit is shown in figure 6.9. It can be seen that from node 4 up to node 23, the temperature can be approximated by a parabolic line. Before and after these nodes, thus node 1 to 3 and node 24 and 25 show non-linear behaviour due to their proximity to the CORE hinges. This means that the strain of the booms from node 4 to node 23 can be measured on a few nodes along the length of the boom, from which a polynomial fit is created. The best results are found by taking the strain of the booms at node 4, 5, 7, 13, 18, 22 and 23 to create a 4th degree polynomial fit. Because only the total expansion of the booms is required, and not the local deformation, the fit is used to calculate the total expansion of the booms. The maximum error in the predicted translation is found to be $0.285 \mu m$. This, however, means that the strain needs to be measured along nine locations of the booms. Another good fit is found by leaving node 7 and 18 out and applying a parabolic fit. This results in a translation error of $0.426 \mu m$, but requires fewer sensors.

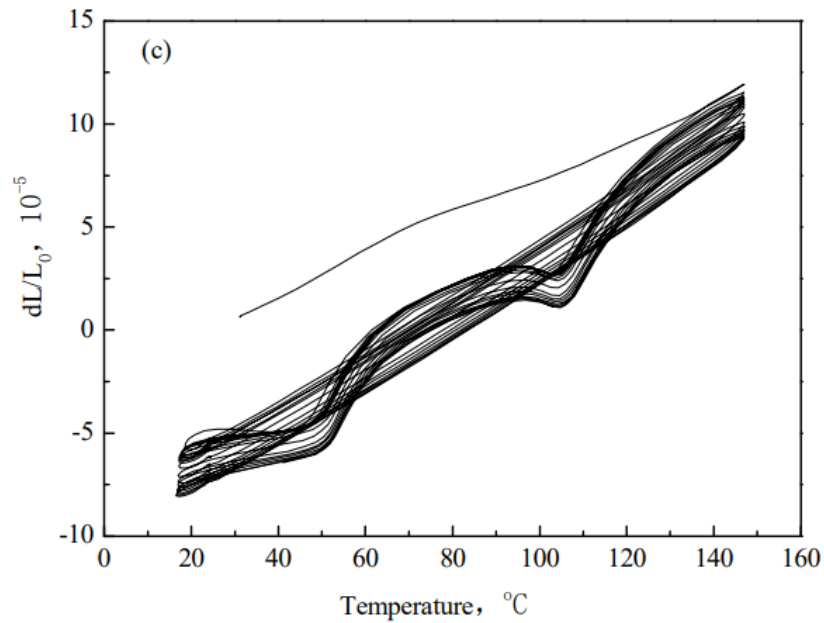


Figure 6.8: Thermal recycling hysteresis curve of carbon fibre reinforced composite. Retrieved from Song et al. (2017).

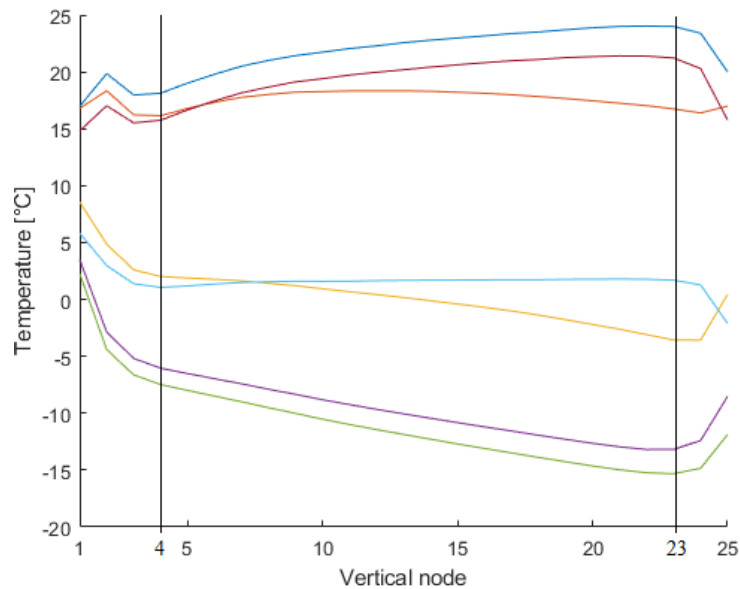


Figure 6.9: Vertical temperature distribution of one of the nodes. The seven lines each represent one time-step in orbit. Node 1 is closest to the instrument housing and node 25 closest to the spider.

Besides the errors introduced due to imperfect information about the longitudinal strain variation, the strain also differs in the vertical slabs of the boom. The temperature and strain not only differ over the circumference of the booms but also through the wall thickness. Because of the low wall thickness, the difference in temperature between the in- and outside of the booms is small. This means that the strain is largely the same on the in- and outside of the booms. Of course, even here some variation is possible, but this variation is assumed to be negligible because of the thinness of the walls. Placing the strain gauges on the inside of the booms provides distinct advantages. It allows for simple cable management inside of the booms and means the cabling does not require any specific coatings. All sensors are therefore placed on the inside of the booms. The temperature distribution of a few cross-sections of the booms can be seen in figure 6.10. The temperature distribution as seen in the blue

and red lines in figure 6.10 represents a sine wave, for which the average temperature can easily be calculated by measuring any two opposing points on the circumference of the boom. However, the other lines deviate from a pure sine wave with bumps in the temperature around a 135 degree angle, meaning more measurement points are required for strain predictions. The error in total calculated translation is calculated for different sensor arrangements, where the amount of sensors is varied from 2 to 16 nodes over the circumference of the booms, as seen in figure 6.11. It is apparent that indeed calculating the average strain with only two nodes introduces high errors, with a maximum translation error of $1.07 \mu\text{m}$. Increasing the number of sensors leads to clear improvements in temperature prediction accuracy, with the maximum error going down to $0.071 \mu\text{m}$ when four sensors are used and even going down to $0.018 \mu\text{m}$ and $0.014 \mu\text{m}$ with respectively 8 and 16 sensors. Doubling the number of sensors from 4 to 8 only increases the accuracy of the prediction by $0.054 \mu\text{m}$, whereas the complexity and mass of the system double. The strain of the booms is, therefore, be measured by four opposing sensors on each vertical node. This analysis is valid for all vertical nodes except for the one in the middle (node 13), where the booms are cut-out to create the strain-energy deployment hinge. Here, the temperature is measured using two sensors.

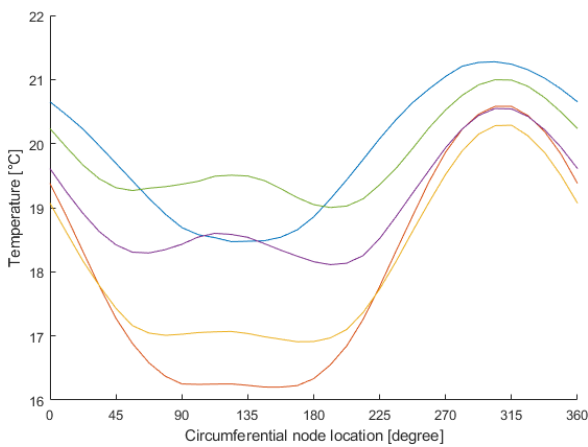


Figure 6.10: Temperature distribution around the circumference of a boom.

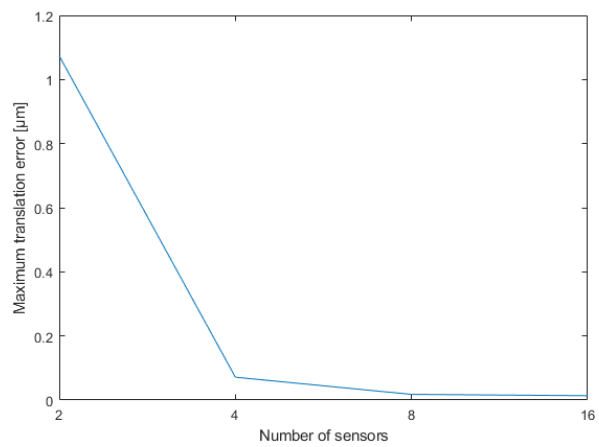


Figure 6.11: Temperature measurement error due to discrete amount of nodes.

Another error arises due to the non-uniform temperature distribution along the circumference of the boom. Locally, the temperature difference between the hot and cold side of the boom can go up to around 5 K. The local difference is, however, not of importance, but the averaged difference. The maximum difference in average temperature over the circumference of the booms (so, for instance, the average of the temperature at 135 degree compared to the average temperature at 315 degree) goes up to 1.7 K. This means that, if the booms are allowed to expand freely, one side expands about $2.25 \mu\text{m}$ more than the other. This process is visualised in figure 6.12. In this case, the temperature of side 1 increases, on average, more than that of side 2, causing $\Delta L_{b,1}$ to be higher than $\Delta L_{b,2}$. However, because the booms are essentially clamped in one direction (and allowed to rotate in the other) between both CORE hinges, the exact bending modes are complex and require extensive additional modelling. Such models are out of the scope of this conceptual design. What is known, is that the longitudinal expansion lies somewhere between the expansion of $\Delta L_{b,1}$ and $\Delta L_{b,2}$. In consultation with L. J. Kootte, an Aerospace Structures and Materials PhD candidate, it was found that the actual expansion of the booms can be taken to equal $\Delta L_{b,ac} = \Delta L_{b,a} - 0.15 \cdot (\Delta L_{b,1,a} - \Delta L_{b,2,a})$ with a correction error of 15 % (Personal communication, L. J. Kootte, 5 August 2020). This thus introduces an additional error of $0.337 \mu\text{m}$.

Strain gauge sensors can again only be placed on the inside of the CORE hinges. However, because the thickness of the CORE hinges is very small, the difference in strain over the in- and outside of the half-cylinders is considered to be negligible. The only error then arises due to averaging errors. Two configurations are considered, namely configuration A and B as seen respectively in figure 6.13a and figure 6.13b. Configuration A consists of four strain gauge sensors placed on each half-cylinder. They are placed on the sides of the hinge-halves because the horizontal parts do not add to the longitudinal expansion of the deployment legs. The longitudinal expansion is calculated by multiplying the

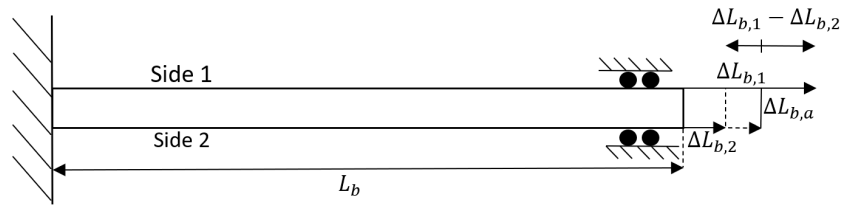


Figure 6.12: Differential expansion of the booms.

strain found at the respective gauge by the longitudinal length of the area that the gauge covers. It is found that the maximum error in the prediction of the total expansion of the top hinges is $0.023\mu\text{m}$ when configuration A is used and $0.029\mu\text{m}$ when configuration B is used. For the root hinges, the error when taking configuration A and B is respectively $0.013\mu\text{m}$ and $0.028\mu\text{m}$. The gain in accuracy due to doubling the number of gauges is low, so configuration B is chosen for both the top and root CORE hinges. However, the expansion of the CORE hinges is expected to be highly non-linear due to high internal stresses within the hinges. An additional correction error of half of the previously mentioned errors is therefore accepted.

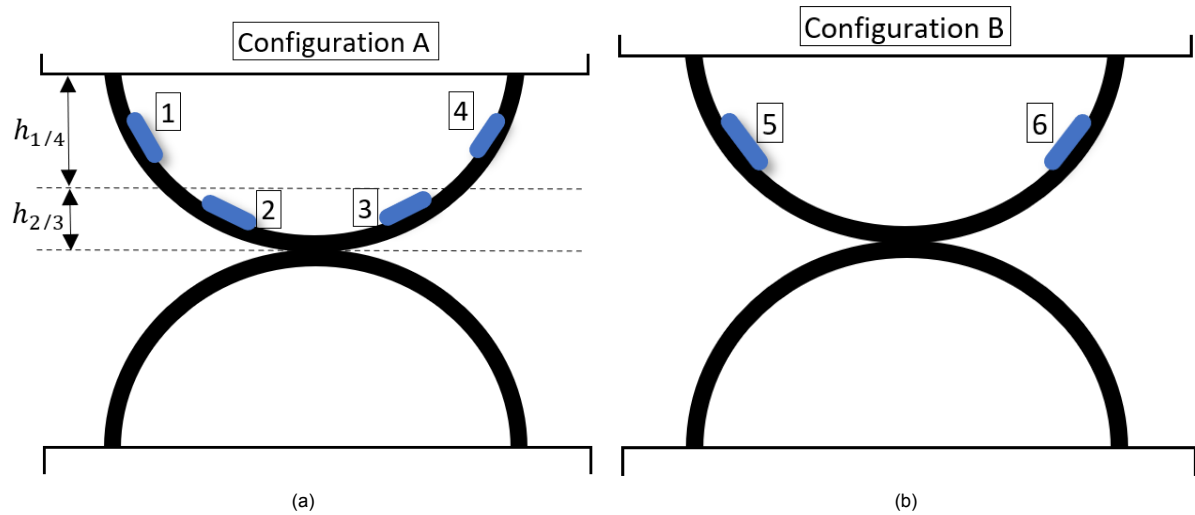


Figure 6.13: Configurations for strain gauge distribution in the CORE hinges.

The resistance of the strain gauges is not only dependant on the strain, but also on the temperature of the gauge. By matching the temperature response to the CTE of the booms, the error introduced by this temperature response can be minimised. However, with a temperature response of $0.5\mu\text{m}/\text{m.K}$, it does not perfectly match the CTE of the booms of $0.8\mu\text{m}/\text{m.K}$. A further temperature tolerance of $0.3\mu\text{m}/\text{m.K}$ adds to the problem. The CTE of the hinges is matched with a difference of $0.2\mu\text{m}/\text{m.K}$. The predicted accuracy of the total strain can thus degrade very much with changes in temperature. This means that, for the error to stay reasonable, the temperature needs to be measured at the strain gauge locations. This can be done by using the system of thermistors, as discussed in section 6.2.1. By using this system, the average temperature of the booms is predicted with an accuracy of 0.423K , whereas the temperatures of the root and top CORE hinges is predicted with respectively 0.09K and 1.18K . This means that the temperature-induced error caused in the booms, top and root hinges can go up to respectively $0.419\mu\text{m}/\text{m.K}$, $0.001\mu\text{m}/\text{m.K}$ and $0.023\mu\text{m}/\text{m.K}$ for a total error of $0.4434\mu\text{m}/\text{m.K}$. The total error caused by both the errors in measuring the strain and temperature of the CORE hinges and the booms can go up to $1.202\mu\text{m}$.

Then for the sensors themselves. Micro Measurements, a provider of space-rated strain gauges, specifies that their most accurate high life-time strain gauges can reach an accuracy of 1% [84]. The accuracy in terms of displacement is then a function of the maximum expansion of the booms. With a maximum expansion of $80\mu\text{m}$, the error can go up to $0.8\mu\text{m}$. However, this random error is decreased by the

inverse square of the number of sensors. This would typically only be the case if all sensors are placed on the same location, however as the total expansion is a function of the average of all sensor readings, it can also be applied in this case.[85]. With a total of 48 strain gauges per deployment leg, this error goes down to $0.116 \mu\text{m}$. This means the total error in translation increases to $1.318 \mu\text{m}$.

Over the course of the lifetime of the telescope, it orbits Earth about 27000 times, meaning the sensors will go through 27,000 heat cycles. The strain gauges provided by Micro Measurements have a fatigue life of up to 1 million cycles. Even though this is more than the cycles that the telescope will go through and exact failure rates are unknown, it can safely be assumed that in using such a high number of sensors at least a few will fail during the lifetime of the satellite. This inevitably means that over the lifetime of the telescope, the accuracy of the translation predictions goes down. With a total number of strain gauges of 56 per deployment leg, they will cumulatively go through about 1.5 million cycles. One could thus expect about two strain gauges to fail per deployment leg. In taking a conservative margin of error of 2, four strain gauges could fail per leg. A gauge failure at any of the middle vertical nodes 7, 13 or 18 can, at most, increase the total error by $0.308 \mu\text{m}$, which could cumulatively lead to an increase in error of $0.794 \mu\text{m}$, which is unacceptable. Therefore, the strain gauges at these four locations are made fully redundant, so eight are placed along the circumference of the boom. At any other location along the length of the boom, the maximum error due to gauge failure is $0.05 \mu\text{m}$, for a total of $0.2 \mu\text{m}$ if four gauges fail. This is deemed to be acceptable, so no redundancy is required. A gauge failure at the top and root CORE hinges can cause errors up to $0.460 \mu\text{m}$, which is too high. The gauges at the top and root hinges should, therefore, also be fully redundant. The same story applies to the thermistors. IST AG, a provider of European Space Components Coordination (ESCC) qualified thermistors, provides platinum thermistors with a stable lifetime up to 70,000 cycles[86]. This means a total of $2 * 20$ sensor failures can be expected per leg. The error in average temperature increases by 0.046 K per thermistor failure, even at the least critical thermistor locations. This means an induced translational error of $0.045 \mu\text{m}$ per thermistor failure. This is too high, meaning that all thermistors should be made redundant. Lastly, it is assumed that no systemic error is present, because this can be resolved by focussing efforts outside of the imaging phase (Personal communication, D. Dolkens, 29 July 2020).

The strain measurement system consists in this configuration of 60 strain gauges per boom and 8 for every CORE hinge for a total of 304 strain gauges to be placed on the deployment legs. These strain gauges have a mass of about 0.05 g per piece, so all strain gauges combined have a mass of 15.2 g . It furthermore consists of in total 464 thermistors, also with a mass per piece of 0.05 g , thus totalling 23.2 g . All sensors combined, however, require 1536 wires with an average length of 0.85 m , so a total cable length of 1305.6 m . Draka Fileca S.A.S., a provider of ESCC qualified cables, details that their single enamelled cables have a weight of 1.23 g/m [87]. The total cabling mass is then 1605.9 g . The gauges also draw power, but very little. Typically, strain gauges have a resistance of 1000Ω , with a voltage across these gauges in the range of 3 to 10 V [88]. A typical strain gauge thus has a power draw of about 0.025 W , meaning that the combined power draw is 7.6 W . The power draw of the thermistors is even lower, at a total of 0.042 W . The total system mass is then around 1715.2 g . This, however, does not yet include any central data acquisition system. Besides the fact that no COTS space-rated data processing units for such a high number of channels are available, the mass of such a data acquisition system is expected to be very high.

Concluding, the necessary accuracy of at least $2 \mu\text{m}$ can be reached. This however goes at the cost of a very complex system with a lot of individual sensors and cables. The exact mass of such a system is not known, but expected to be very high. For these reasons, this system is omitted from the trade-off.

Fibre Bragg grating sensors

Fibre Bragg grating sensors are built up of an optical fibre in which Bragg gratings are introduced. These gratings reflect particular wavelengths of light and transmit others. As light travels through the fibre, any strain or temperature difference applied to the Bragg grating causes a wavelength shift and magnitude change of the reflections, which allows for accurate measurements over long periods of time.[89] Their working principles are shown in figure 6.14. Stretching a FBG sensor, as shown in

figure 6.14a, causes a change in grating period which results in a change in wavelength of the reflected ultraviolet light. The gratings reflect wavelengths within a very low bandwidth, the so-called peaks in the spectrum. Each grating consists of many thousands of fringes, as shown in figure 6.14a. Each of these gratings reflects a small fraction of all incoming wavelengths. Because each fringe reflects light with a different phase shift, interference occurs, which erases most of the light. However, the reflections with equal phase shifts accumulate to a strong reflection peak. This behaviour is visualised in more detail in figure 6.14b. A grating with ten fringes is shown on the top. Below, three different light beams with different wavelengths are shown. The first one has exactly the same wavelength of the grating period, which means all fringe reflections are in phase, causing a reflection with an energy level 10 times as high as a single fringe reflection. The other beams contain wavelengths with respectively 10% higher and 10% lower periods than the grating. This results in each reflection having a different phase, meaning the light interferes and cancels out. By this mechanic, and measuring the reflected light, the period of the grating can be determined accurately. With this period, in turn, the strain can be determined.

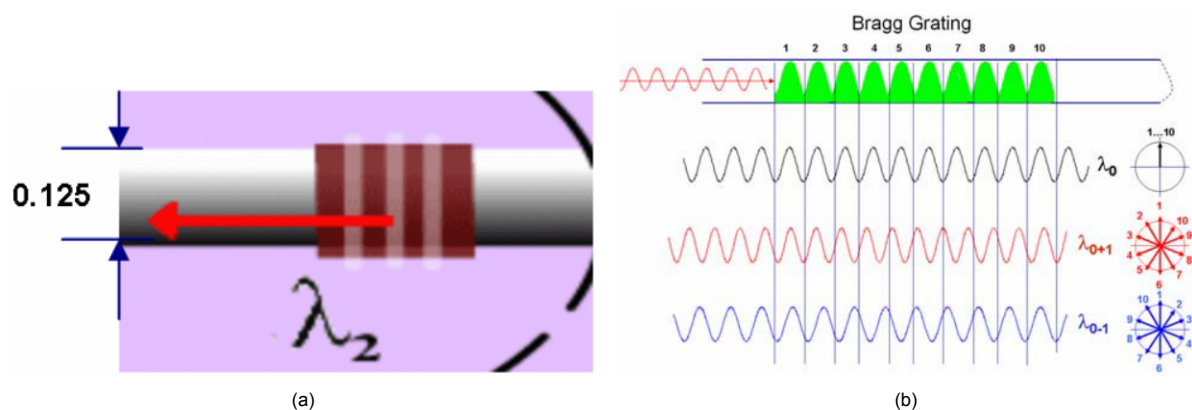


Figure 6.14: Overview of Fibre Bragg Gratings a) Fibre Bragg Grating schematic and b) Functional principle of Fibre Bragg Gratings. Both retrieved from Kreuzer (2020).

FBG sensors already have flight heritage on the Proba-2 demonstration mission[91], proving their applicability in space applications. They provide some distinct advantages. Firstly, they require no power in the fibres, which means no additional power cables run through the booms. They can, furthermore, easily be placed in series, have very high long term stability ($> 10^7$ cycles) and can be very accurate. However, the measured strain also depends on the temperature of the fibre, for which it cannot provide self-compensation. A 1 K change in temperature of the fibre shows results equivalent to $7 \mu\text{m}/\text{m}$ mechanical strain, meaning very high errors are found if the temperature is not measured independently. This issue can be resolved by either measuring the temperature or by placing the strain-measuring FBG sensor on a location of the specimen without any mechanical strain.[90] The second way is not possible within the booms, because the fibres need to be placed within the booms. This means that the temperature of the fibre needs to be measured. Any sort of temperature sensor can do this, including pure temperature measuring FBG sensors. The difference between a strain-measuring FBG sensor and a pure temperature-measuring FBG lies in the way by which the gratings are attached to the specimen. If the grating itself is structurally attached to the boom, it follows the expansion of the boom and is thus a strain-measuring sensor. If the grating is not attached to the boom, and sufficient spacing is used between the attachment points of the fibre and the grating, the boom is allowed to expand without introducing a strain in the grating. The grating is then a pure temperature-measuring sensor. The elegance of the solution lies in the fact that in one optical fibre different types of measurements can be done, by structurally attaching some gratings to the boom and not attaching others. Because of the possibility of integrating multiple types of gratings within one fibre, a solution comprised solely of FBG sensors is considered preferential over using other types of temperature sensors.

FBGS, a FBG sensor manufacturer, specifies that their fibres can include up to 40 gratings.[92, 93] Because the cost of adding more gratings within the fibre is low, namely equal to the added mass of the grating, which is 1 g for glue-able gratings[94], as much as possible are used. The gratings do

however need to be spaced apart to accommodate the optic fibre and allow for the pure-temperature measuring gratings to be independent of the boom expansion. With a minimum spacing of 10 mm and a maximum grating length of 10 mm[93] between the gratings, the maximum of 40 gratings can be placed along the length of the booms.

Over the spacing between two gratings, the temperature can differ by up to 0.7 K. The elegance of FBG sensors lies in the fact that in one fibre, pure temperature measuring and strain measuring gratings can be used. In doing so, 20 temperature measuring and 20 strain sensing gratings can be used over the length of the boom. With 20 strain gratings, the total strain can be predicted with an accuracy of $0.122 \mu\text{m}$. However, the strain measurements are also dependant on the temperature of the gratings. With 20 temperature sensors, the temperature anywhere on the boom can be predicted with an accuracy of 0.098 K. This, combined with a measurement error of 0.05 K, means the temperature of the strain measuring gratings can be predicted with an accuracy of 0.148 K. With a thermal sensitivity of $7 \mu\text{m}/\text{m}/\text{K}$, this introduces a temperature-induced strain measurement error of $1.0360 \mu\text{m}$. The circumferential averaging error, as discussed for the strain gauges, is $0.053 \mu\text{m}$ and the correction error is $0.335 \mu\text{m}$. Measuring the strain in the CORE hinges using FBG sensors is possible, but impractical. It requires multiple fibres to zig-zag across the hinges, quickly increasing the mass and complexity of the system. It is therefore much simpler to use strain gauges, and the accompanying thermistors, in the CORE hinges. This is done similarly to what was discussed in section 6.2.1. This introduces an additional translational error of $0.081 \mu\text{m}$.

For both the FBG sensors and the strain gauges, the random error is 1%. Because the total number of sensors (the amount of gratings per boom) is higher than the number of strain gauges as discussed in section 6.2.1, the additional error is also a bit lower at $0.089 \mu\text{m}$. Combined, the total translational error equals $1.662 \mu\text{m}$. FBG sensors have high lifetimes. They typically have an operating lifetime of 10^7 cycles. This means that, over the lifetime of the telescope, the sensors are not expected to fail. Furthermore, adding more fibres would significantly increase the total mass of the system. Even though the accuracy is quite low at $1.662 \mu\text{m}$, it is still sufficient. Therefore, using four fibres per boom is deemed to be preferable over using eight fibres. FBG interrogators, the system which emits the light and measures the wavelength shift, are available commercially. COTS versions with eight channels were found with a mass of 4.9 kg per interrogator. These are however not rated for use in space, so a customised product is required. The proba-2 mission used a custom 6-channel interrogator with a mass of 1.3 kg and a power consumption of 3.5 W[95]. In assuming that half the mass of this interrogator consists of the laser channels and half of the electronics and the cover, each measurement channel is calculated to have a mass of about 108 g. 16 Channels then have a mass of 1733 g. The casing and electronics also have to be scaled up. In going from 6 to 16 channels the volume almost triples, which means the casing mass almost doubles to 1250 g. By applying the same reasoning, a total power consumption of 8.03 W is found. Furthermore, with a mass of 1 g per grating, 40 gratings per fibre and 4 fibres per boom, the total grating mass is 640 g. The fibre has a weight of 0.3 g per meter[96]. With a total length of 1.25 m per fibre, the total optical fibre mass equals 6 g. Additionally, a total of 64 strain gauges and 80 thermistors is placed on the CORE hinges. These sensors themselves have a total mass of 7.2 g and the accompanying cables and cable interfaces have a total mass of 160.6 g.

In summary, the accuracy of the longitudinal translation using FBG sensors in the booms and strain gauges in the CORE hinges is $1.635 \mu\text{m}$ at Beginning-of-Life (BOL). The total system mass is expected to be 3.769 kg and has a power consumption of 8.03 W. Because no COTS space-rated interrogators are available and stress-measuring FBG sensors are not yet tested in space, the TRL of the system is low. There is, however, no reason to think the technologies involved would not operate in a space environment.

Visual measurement using cameras

The distance of an object can be measured directly if the actual length or width of the object is known. This can be done by counting the amount of pixels that the object spans in the image. Even though the principle is relatively easy, implementing it to measure such small translations is not possible with the currently available hardware. If, for instance, the width of the spider legs is used as a reference,

an easily distinguishable parameter as seen from the instrument housing, a longitudinal translation of $1 \mu\text{m}$ would cause a change in apparent spider leg width of $5.19 \cdot 10^{-9}$ rad, which is thus the minimum required angular resolution. Besides a lot of practical issues, using equation (2.1) quickly shows that this requires an aperture diameter in the order of 100 m. This simple calculation thus shows that measuring the translation of the secondary mirror by utilising cameras is not a viable option.

Visual measurement using laser interferometry

DIMs use the interference of light to measure relative displacements. By monitoring the deviation in amplitude caused by interference of a reference beam and the measuring beam, the displacement of the measuring leg can be determined accurately. This principle is shown in figure 6.15. DIMs can provide for very precise displacement measurement over very small to very large distances.

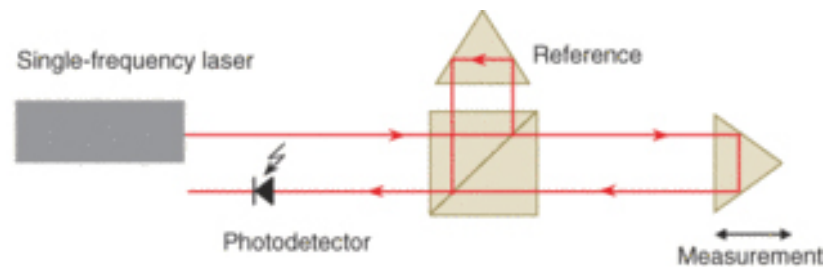


Figure 6.15: Displacement measuring interferometer. Retrieved from Motion X Corporation (2019).

DIMs are typically used in industrial applications to measure the shape of component up to nanometre or even picometre scale, for instance in the production of mirrors for telescopes. Another use-case is the measurement of gravitational waves by measuring the distance between satellites, for instance as is planned for the Laser Interferometer Space Antenna (LISA) mission. These two applications show that it is possible to use DIM for measuring very small and large scale distances with very high accuracy. However, DIM are typically not commercially available for the precise use-case as mentioned here. They do not have, as far as the knowledge of the author goes, any flight heritage to measure the distance between components within a single satellite. There is, however, no apparent reason as to why DIMs would not operate in a space environment. If anything, the accuracy of DIM is better in a high vacuum because of the lack of disturbances due to atmospheric changes.

An example of a DIM with the required range and accuracy is the Industrial Displacement Sensor (IDS) as produced by Attocube. In using the appropriate sensor head, the displacement can be measured up to a distance of 4 metres with high accuracy, as visualised in figure 6.16. At a distance of 1.85 m, the expanded measurement uncertainty is about $0.5 \mu\text{m}$. However, Attocube specified that even though the sensor heads can withstand high vacuums, the main body of the DIM is not space-certified (personal communication, I. Park (Attocube), 20 August 2020). Furthermore, no other COTS DIMs were found with the required specifications. This means that, if a DIM is used, companies have to be willing to put in a lot of work to design and certify a DIM for use in space. That being said, if such DIMs become available, they would provide a simple and good solution. Therefore, a hypothetical system using a DIM is outlined here and given a low TRL in the trade-off.

The main body of the IDS has a mass of 730 g and a power consumption of 8 W, whereas each laser has a power of $400 \mu\text{W}$. The sensor heads have a mass of 50 g and the fibres a mass of around 20 g per fibre. Furthermore, four reflectors are required. These reflectors can be as small as 9 by 9 mm and have a mass of around 1 g.[98] The mass and power consumption of the body can probably be minimised for use in space, but because the exact hardware and modes of operation of the IDS are not known, this is hard to substantiate. Furthermore, comparable systems are barely present; the only other DIM that is planned for use in space is the system used in the LISA mission. The ratio between DIM power consumption and laser power of the LISA satellites is 40, much lower than that of the DIM[99]. However, because the scale of both systems is so different (laser power of 2 W versus $400 \mu\text{W}$), no hard conclusions can be drawn from this comparison. It does however strongly suggest that with a custom design, the total power consumption, as well as the mass, can be reduced drastically. For now, the mass and power consumption of the IDS as provided by Attocube are therefore assumed

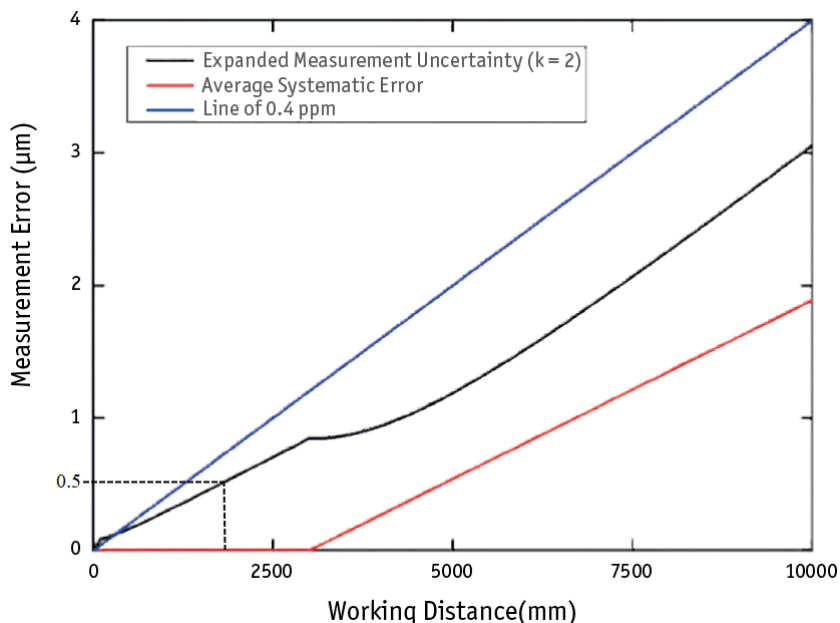


Figure 6.16: Accuracy of the IDS. Adapted from attocube systems AG (2018).

to be required. Further research into IDSs for use in space is required to determine the actual system parameters. Recommendations regarding this issue are presented in chapter 9.

In summary, a system utilising IDSs to measure the displacement of the spider legs provides a simple solution, but as of now, no COTS systems are available. The system is for now assumed to have a total mass of about 1014 g and power consumption of 8 W.

6.2.2. Displacement measurement trade-off

The two concepts that present viable options are the ones measuring the strain by means of FBG sensors and the displacement through laser interferometry. In the upcoming discussion, the former is called concept A and the latter concept B. The criteria on which these concepts are traded-off are the complexity of the system, the accuracy, the mass, the power consumption and the degree to which they are proven to work in space, their TRL. Because cost data is hard to obtain, it cannot directly be quantified. Cost is therefore not individually part of the trade-off. Furthermore, the difference in cost between both concepts is expected to be small. A graphical trade-off is shown in figure 6.17. Because concept A has clear deficiencies regarding all criteria except for its power consumption, it is regarded as a poor option. Concept B performs well on all criteria except for its TRL. This means that, in principle, the concept provides a good solution. It does require a big commitment from private companies to develop the required technologies. However, because it is the only concept shown to be viable on all other criteria, it is chosen to be used to measure the displacement of the secondary mirror. The rationale for the scores is presented below.

Complexity

Concept B consists of a simple system. The main body is placed in the instrument housing, and the sensors heads and reflectors can be placed on mountings at the instrument housing and the spider legs. The fact that the optic fibres have to run from inside of the instrument housing to the sensors heads means that the system does not score excellent. Concept A requires much cabling to run from the instrument housing to and through the booms. Each boom has to accommodate four optic fibres and 18 electrical cables for the strain gauges and thermistors. Because the boom mid-hinge relies on its flexing properties for deployment, special arrangements have to be made for these cables as to not hinder the deployment. Furthermore, all sensors have to be read out, meaning a computer with 144 connections is required for the strain gauges and thermistors, which in itself might pose a big problem. These reasons make that concept A has apparent deficiencies.

Concepts	A. Fibre Bragg Grating sensors	B. Laser interferometry
Criteria		
Complexity	O	B
Accuracy	O	B
Mass	O	B
Power	B	B
TRL	O	O

Green	Excellent
Blue	Good
Yellow	Neutral
Orange	Clear Deficiencies
Red	Unacceptable

Figure 6.17: Graphical trade-off table for deciding the translation measurement concept.

Accuracy

The score regarding accuracy is determined using a scoring scheme. With an accuracy of $1.635 \mu m$, concept A does not meet the requirements but still has apparent deficiencies. Concept B easily meets the requirements with an accuracy of $0.5 \mu m$. It therefore scores good.

Mass

The same scoring scheme as used for the actuators, as shown in table 6.3 is used. With a total mass of 3.769, concept A has apparent deficiencies regarding its mass. With a total mass of 1.014 kg, concept B scores good.

Power

Again, the same scoring scheme as used for the actuators, as shown in table 6.4 is used. With a power consumption of 8 W, both concept A and B score good.

Technology Readiness Level

Fibre Bragg Gratings have been shown to operate in space, but only as temperature sensors and not as strain sensors. However, because there is no structural difference between both types of FBG sensors, there is no reason to believe FBG strain sensors cannot operate in space. The difference between both sensors lies in the way in which they are attached to the specimen. Attaching FBG strain sensors requires the gratings to be structurally fixed to the booms, for which numerous methods are already available. However, a lot of design work and verification activities have to be done to make sure that these sensors can operate in space. Concept A, therefore, has clear deficiencies. The same reasoning applies for concept B. Laser interferometers are proven to have the required accuracy over the required range, and with other missions, like LISA, proving the required technology operates in space, there is plenty of reasons to believe laser interferometers can operate in space. Concept B, therefore, also has clear deficiencies but is still acceptable.

6.3. Secondary mirror mount

With the omission of the secondary mirror hexapod flexure mount, as explained in section 5.3, a new mount has to be chosen. A lot of system work is already performed in Krikken (2018), and does not have to be repeated. A big part of the discussion presented in this section is therefore inspired on Krikken's work. Krikken defines six different concepts, namely hard mounts, clip mounts, elastomer mounts, bonded mounts, kinematic mounts and flexure mounts. Whereas Krikken chose a hexapod mount specifically for the reason that it can make the telescope athermal, it is the same underlying principles for

which a hexapod mount is not a good option. A hexapod mount puts the secondary mirror closer to the primary mirror, thus requiring the booms to be longer and heavier. Furthermore, the length of the legs makes them susceptible to thermal expansion. Even though this expansion might counter the boom expansion, it still needs to be measured, thus requiring additional hardware and thereby complexifying the system. An additional design effort is therefore required. The different design options as identified in Krikken (2018) are presented and discussed in section 6.3.1. In this discussion, particular attention is paid to the unconventional cross-shape of the secondary mirror. Most conventional mounting methods are based on either square or circularly shaped mirrors, and as such do not present a viable option. In this discussion, only tried and proven mounting methods are considered, because anything else would unduly increase the amount of required design work.

6.3.1. Mounting concepts

Several different mounts are commonly used for mounting small non-metallic mirrors. The mounting concepts considered here in respective order are hard mounts, clip mounts, elastomer mounts, bonded mounts, kinematic mounts and flexure mounts.

Hard mounts

In a hard mount, the mirror is clamped between rigid parts of the mount, typically between a retainer and the mounting cell. The retainer ring often has a loose fit within the thread, enabling it to self-align during tightening. Two types of hard mounts are typically identified, as shown in figure 6.18a and figure 6.18b. In figure 6.18a, the alignment is provided by precision-milled pads within the mount. In figure 6.18b, temporary centring screws are used to maintain radial alignment during assembly. After tightening the retainer ring, epoxy is applied after which the temporary screws are removed. The advantage of these mounts lies in their simplicity, in form and manufacturing method.[22] However, threaded retainers do not adapt well to non-circular symmetric applications, making them an infeasible option for the cross-shaped secondary mirror of the DST.[100]

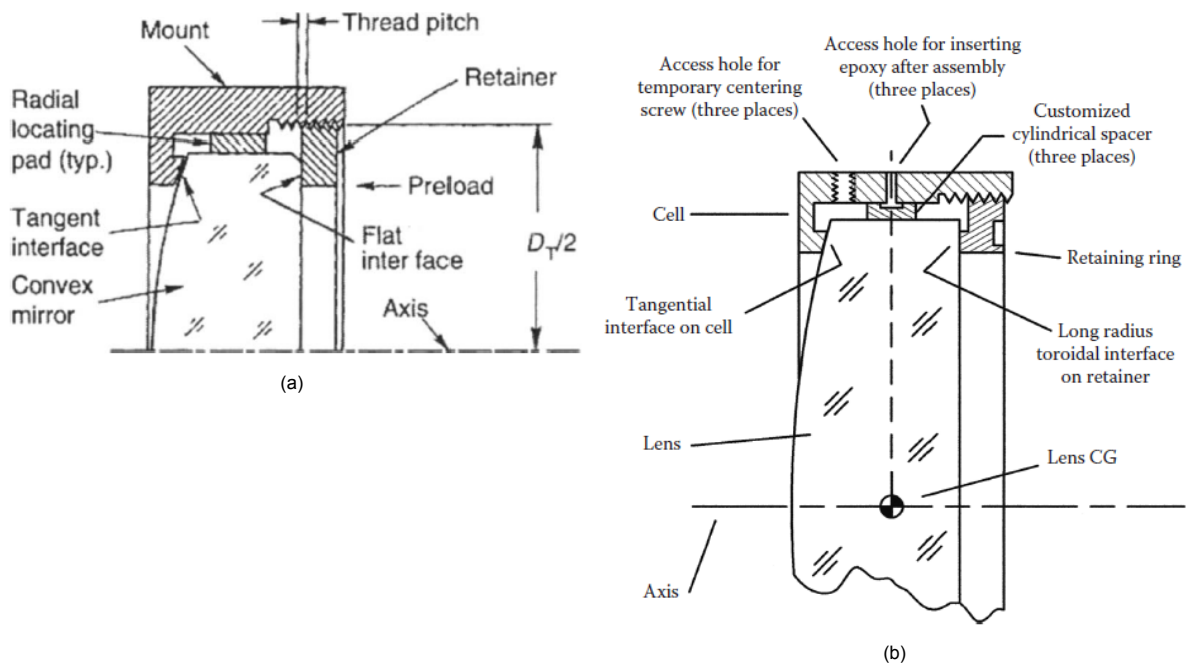


Figure 6.18: Two different types of hard mounts. a) is retrieved from Yoder (2008) and b) is retrieved from Yoder and Vukobratovich (2015).

Clip mounts

Instead of using a retainer ring, as used in hard mounts, the preload can be provided through clips, as visualised in figure 6.19. The mirror is pressed against the back of the mount by the clips, where it can be axially aligned. The radial alignment is achieved in a similar fashion as the process used for

hard mounts.[100] The advantages and disadvantages of clip mounts are mainly similar to those of hard mounts, and so is the fact that they are not well suited for non-circular mirrors.[22] Clip mounts are therefore also not considered a viable option.

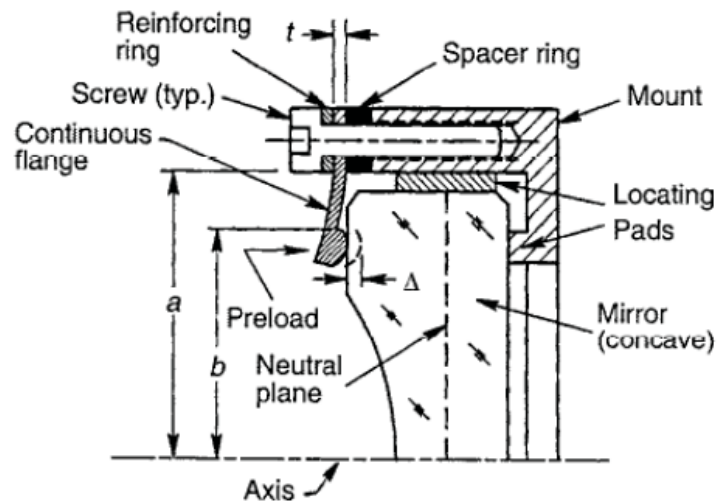


Figure 6.19: Clip mount. Retrieved from Yoder (2008).

Elastomer mounts

Elastomer mounts are similar to clip and hard mounts in that they have a main mount, or cell, surrounding the mirror. This is visualised in figure 6.20. To provide enough bonding area, the mirror itself is made a bit bigger than what is required for the optical path. Elastomer mounts provide some distinct advantages over the previously mentioned mounts. The gap between the cell and the mirror can be designed such that the mount is athermal.[22] Furthermore, this type of mount can be used to mount non-circular mirrors. However, because the mirror needs to be bigger and the cell again surpasses the mirror size, the mount might interfere with the optical path of the primary mirror. This degrades the image quality and as such is not considered to be a viable option.

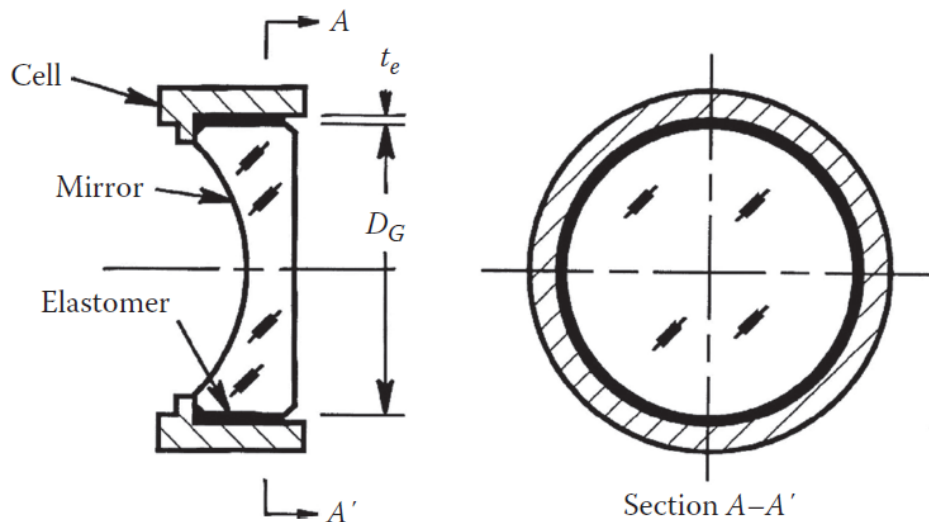


Figure 6.20: Elastomer mount. Retrieved from Yoder and Vukobratovich (2015).

Bonded mounts

Bonded mounts consist simply of a bonding agent applied directly between the mirror and the support. This type of mounting can be used for mirrors with a radius up to 15.2 cm. Furthermore, the ratio of the

largest mirror face dimension to the thickness of the mirror should be no higher than 10:1 and preferably lower than 6:1, to avoid excessive distortion of the mirror during curing or under temperature changes. With a ratio of 7.8:1 for the DST secondary mirror, this type of mount can be used, but care must be taken to not introduce excessive stresses. The minimum bonding area, A_{min} , is calculated as shown in equation (6.2). Here, m , is the mass of the mirror, a_G the worst case acceleration, f_s the safety factor and G the adhesive's shear or tensile strength.

$$A_{min} = \frac{ma_G f_s}{G} \quad (6.2)$$

From Yoder (2008), the shear strength of 2216B/A epoxy, a commonly used bondage agent, of $1.758 \cdot 10^6 \text{ kg/m}^2$ and a standard safety factor of 2-5 is found. Taking a safety factor of 3.5 (middle of the range) and an acceleration factor of 30 G, in line with the quasi-static acceleration loads which the telescope has to survive, results in a minimum bonding area of 5.92 cm^2 . In applying the bonding agent, a multitude of configurations is possible, of which a few are shown in figure 6.21a. Good results are typically found if the bonds are placed on the "0.7-zone".[22] The exact manner in which this is done does not significantly affect the performance of the bond, as long as the total bonding area is equal or larger than the minimum bonding area. Using multiple bonding areas has the added advantage that thermal expansion problems are minimised and also helps secure the mirror in a more kinematic fashion.[100] An example of how this is applied in this case is seen in figure 6.21b.

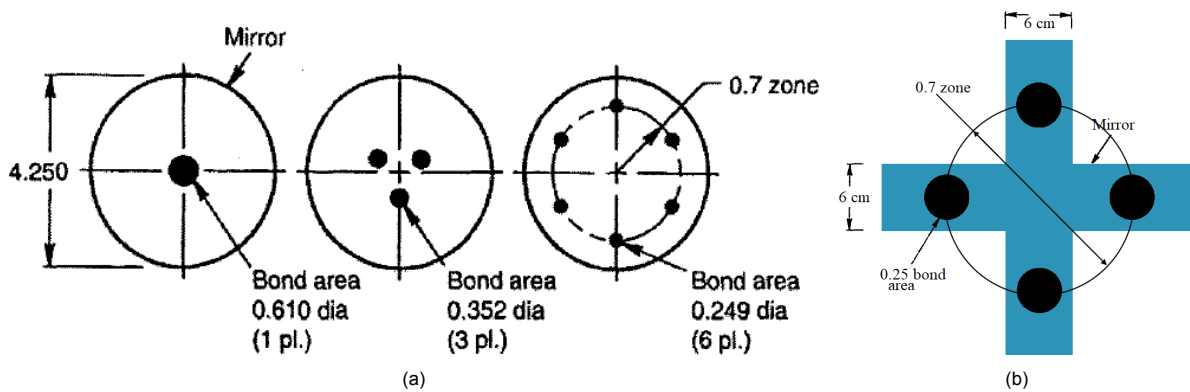


Figure 6.21: Bonding surfaces for mounting mirrors. a) Example of possible distributions as retrieved from Yoder (2008) b) Example distribution for DST secondary mirror.

Bonding a mirror directly to CFRP plates is not a problem, as was shown in Catanzaro et al. (2000). The support structure therefore exists of a thin CFRP sheet. This has the advantage that the CTE of the CFRP material already used is close to that of the glass mirror. A problem that might arise due to unequal thermal expansion of the mirror and mount is the introduction of exceedingly high stresses in the mirror. The maximum stress is found using equation (6.3a), as defined in Chen and Nelson (1979). Here, α_1 and α_2 are the coefficient of thermal expansion of the mirror and mount respectively, ΔT is the maximum temperature deviation from the assembly temperature, G is the shear strength of the bonding agent, R is the radius of the bond, η is the thickness of the bond, and β is defined in equation (6.3b), where t_1 and t_2 and E_1 and E_2 are respectively the thickness and elastic moduli of the mirror and mount.[100]

$$\tau_{max} = \frac{(\alpha_1 - \alpha_2) \Delta T G \tanh(\beta R)}{\beta \eta} \quad (6.3a)$$

$$\beta^2 = \frac{G}{\eta} \left(\frac{1}{E_1 t_1} + \frac{1}{E_2 t_2} \right) \quad (6.3b)$$

Even though the CTE of CFRP can be modified by changing the layup of the fibres or the epoxy fractions, some difference between the CTE of the mirror and mount can still be expected. The maximum temperature deviation from the assembly is found during the LEOP, where the temperatures can be between 188 K and 384 K[4]. The typical thickness of epoxy bond layers is about 0.102 mm[22].

In using a CTE of $0.8 \mu\text{m}/\text{m}\cdot\text{K}$, the same as that of the booms, the maximum shear stress does not exceed 6.38 kPa. With a silicon carbide fracture strength of 600 MPa[100], the bonds can easily withstand the thermal stresses.[100]

The bonds are thus capable of withstanding both the launch loads and thermal stresses. Then, for the mechanical design of the mount. The top-plate of the spider, as used to prevent radiation from passing through the spider, can be repurposed to form the mounting plate. A circular support with the same radius as the 0.7-zone, as seen in figure 6.21b, is added to add stiffness to the support plate. This supporting structure has a mass of 65 g. The mass of the epoxy bond layer, with a thickness of 0.102 mm, area of 5.92 cm^2 and a density of 1.3 g/cc [103] totals about 0.78 g.

In conclusion, mounting the secondary mirror by bonding provides a light simple and solution. Because of the relatively low CTE of the CFRP mounting plate, the thermal stresses in the mirror stay low. The total mass of the mount equals about 68 g.

Kinematic mounts

A kinematic mount consists of two parts. The first part contains three V-grooves in different directions. Three portions of spheres are attached to the second part such that they fit into the grooves on the first part, thus allowing relative motion. Because of this configuration, both parts are allowed to expand and contract freely without introducing thermal stresses. The two parts are typically preloaded by means of either gravity or springs. On Earth, kinematic mounts provide a useful solution because of their simple yet effective design. However, kinematic designs have certain limitations, of which the most relevant one is that the accelerations to which a kinematic mount can be subjected are limited. Because in space applications the launch loads always have to be accounted for, it is very difficult, or neigh impossible, to use kinematic mounts in space.[22] For this reason, they are not considered in the trade-off.

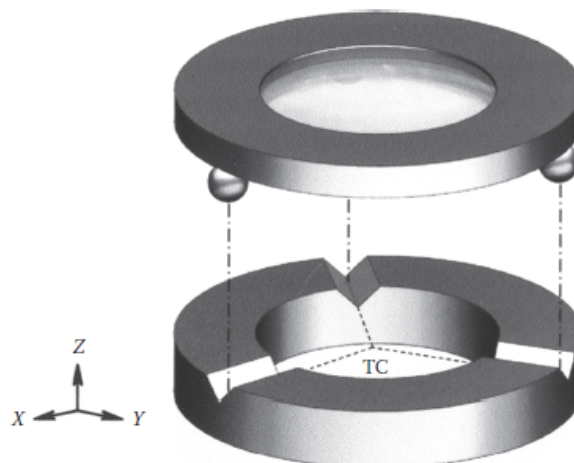


Figure 6.22: Kinematic mount. Retrieved from Yoder and Vukobratovich (2015).

Flexure mounts

Another way to provide relative motion is by making use of flexures. Instead of allowing the different parts to slide over one another, relative motion is achieved by flexing the material of the mount. Flexures are usually designed with compliance in one direction but stiffness in the two orthogonal directions. This usually results in a system which allows movement in one degree of freedom, generally about the mirror's central axis. Whereas for most mirrors this is not a problem, because they are rotationally symmetric, this is not possible in this case. The cross-shape of the mirror does not allow it. However, flexures can take many different forms. Some examples of flexures that can potentially be used are shown in figure 6.23. In designing a flexure, the engineer is free to create whatever shape desired, as long as the correct number of degrees of freedom is constrained. It must, however, be acknowledged that a custom-fit flexure mount significantly adds to the amount of design work the engineer has to do, on top of added complexity in manufacturing, assembly and verification activities. Keeping this

in mind, if flexures are correctly designed, they have the potential to outperform any other mounting.[22]

In figure 6.23a the mirror is bonded to three flat flexures, which are in turn mechanically attached to a circular structure with the same diameter as the mirror. Because the flexures are flat, they can bend radially to accommodate differences in thermal expansion. Even though the secondary mirror is not circular, this principle can be used, for instance by introducing an additional slab of material on the mirror to create a "mushroom mirror", as shown in figure 6.23b. A mushroom mirror has a cylindrical protrusion centrally located on its back face. This protrusion can be an integral part of the mirror or bonded in place. The mounting consists of a number of flexure blades machined into a cylindrical portion of the mounting flange. Each flexure is radially compliant, similar to the flexure blades in figure 6.23a. In figure 6.23c, the outer rim of the mirror is bonded to the centres of three tangentially oriented flexures which are bonded to the mounting structure at both ends. Again, this option might also be used if a mushroom type mirror is used.[22]

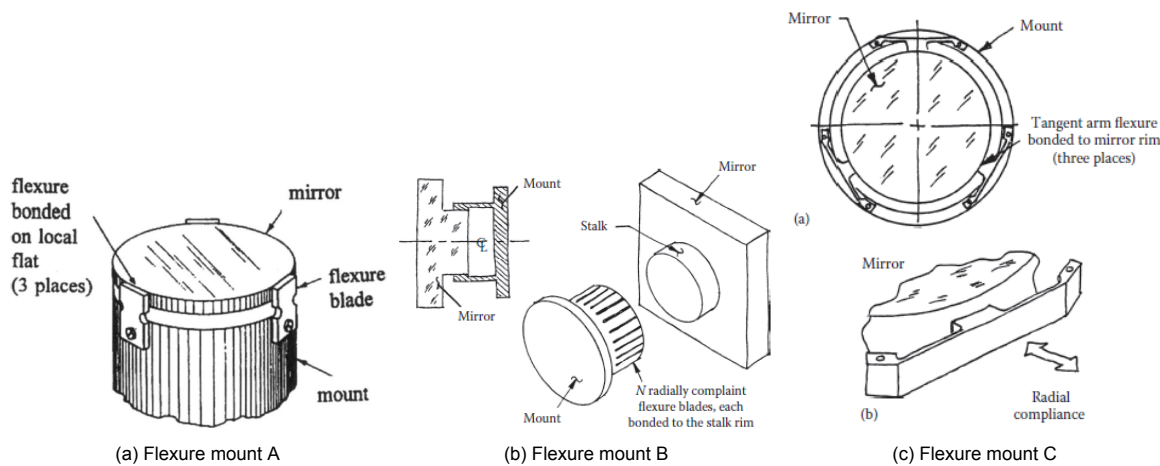


Figure 6.23: Three different flexure mounts. All are retrieved from Yoder and Vukobratovich (2015).

In light of the non-standard shape of the mirror, most conventional methods of creating flexure mounts are not possible. Because any part extending further out than the secondary mirror might obscure the optical path of the primary mirror, such parts are not allowed. However, adding a "stalk" to the back of the mirror to create a mushroom mirror seems to be a good option. In using this shape, all three flexure methods, as seen in figure 6.23, are viable options. The question then is which flexure is the best, which is a hard question to answer without analysing each flexure in full. However, in this case, a qualitative analysis might also suffice. In form, flexure mount A is the most simple. The shape of the flexure blades is easy to manufacture, and the way by which they are attached to both the mirror and the mount is quite simple. The circular shape of the mount can furthermore be integrated into the shape of the spider, meaning no additional mount is required. In function, flexure mount B is quite similar to flexure mount A. However, it requires a new mount to be designed and manufactured, which increases the complexity of the manufacturing process. The flexures of flexure mount C can, as is the case for flexure mount A, easily be attached to the spider. However, the shape of the flexure blades themselves is much more complex than those of flexure mount A. Because the functionality of all three flexure mounts is quite similar and flexure mount A provides the most simple solution, flexure mount A is deemed to be the best option.

Flexure mount design

Here, the conceptual design of flexure mount A is discussed. To create flexure mount A, three main parts are required. Namely a circular structure in the spider to attach the blades to, the blades themselves and the stalk of the mushroom. The first step in designing these components is to find the loads that they have to withstand. The flexures have to withstand quasi-static combined loads in the X+Y, X+Z and Y+Z directions of 30 G. This means, with a mirror mass of 1.01 kg, that the maximum combined load is 300.3 N. Because this load is carried by three flexure blades the maximum load per flexure is estimated to be 100.1 N.

Firstly, the flexure blades. To determine the shape and size of the blades, the material properties of the flexures need to be known. This means that the first step is to find the best material. In this case, the discussion performed in Pepper (2018) on the correct material choice for flexures is very useful. Because the functionality of the flexures of the primary mirror is largely the same as those of the secondary mirror, the discussion on material selection in Pepper (2018) is also applicable in this case. Pepper's analysis results in the graph shown in figure 6.24. Here, the different materials are evaluated on all different traits as identified on the horizontal axis. It was found that Ti-6Al-4V titanium alloys has the best overall performance, with aluminium 7075-T6 and Beryllium I-70 as secondary options.

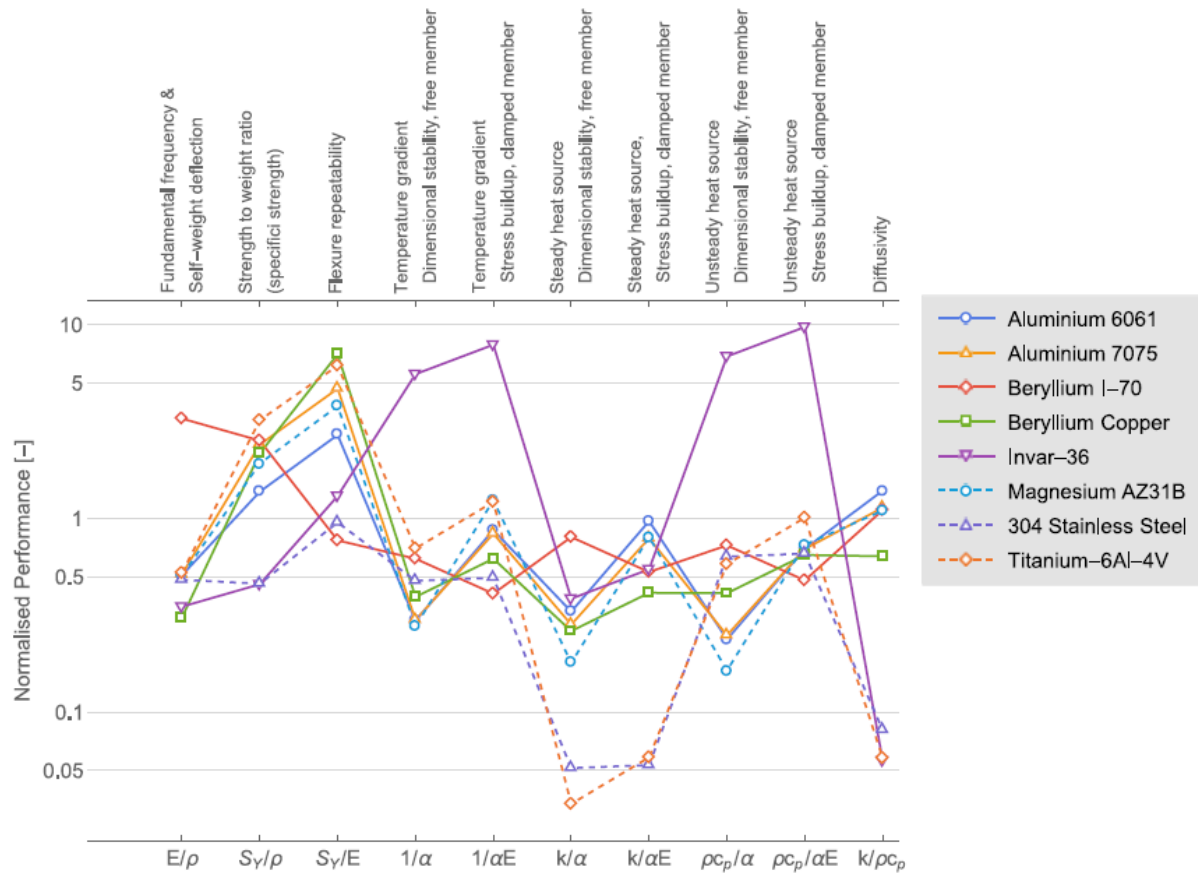


Figure 6.24: Flexure material profiles. Note that scores in each property group are linked to provide a visual cue for comparison only, the line has no physical meaning. As retrieved from Pepper (2018).

In the design of the flexures, some useful rules of thumb can be used. The width (b), length (L) and thickness (t) and the load in X, Y and Z direction are shown in figure 6.25. Firstly, the width of the flexure should be higher than the length, but no more than twice the length, or $L \leq b \leq 2b$. [100, 104] Secondly, the thickness of the blade should not be bigger than one-tenth the width and length, or $L/t > 10$ and $b/t > 10$. [105] To find the maximum shear and bending stress in the structure equations (6.4a) and (6.4b) are applied in all combined loading cases. The maximum equivalent stress of all load cases is then found using equation (6.4c). The blade design should be such that the yield strength of Ti-6Al-4V of 1060 MPa is not surpassed. [100] In doing so, a reasonable design is found with $t = 0.6$ mm, $L = 6$ mm and $b = 9.6$ mm. The maximum equivalent stress is found to be 1050 MPa. This seems close, but the maximum load case of 30G already contains safety margins, meaning additional safety factors are not required. These dimensions largely correspond to the dimensions found in Pepper (2018) and are therefore assumed to be correct. With a titanium alloy density of 4.43 g/m^3 [100], the combined mass of the flexures is only 0.15 g.

In Yoder and Vukobratovich (2015), the preferred method to attach the flexure blade to the mirror is mentioned to be by bonding. In using equation (6.2) and again assuming a bonding shear strength of 17.2 MPa, a minimum bonding area of 20.1 mm^2 is found. The minimum height of the mirror stalk is then determined to be 2.1 mm. To allow for easy manufacturing and assembly, a stalk height of 1 cm

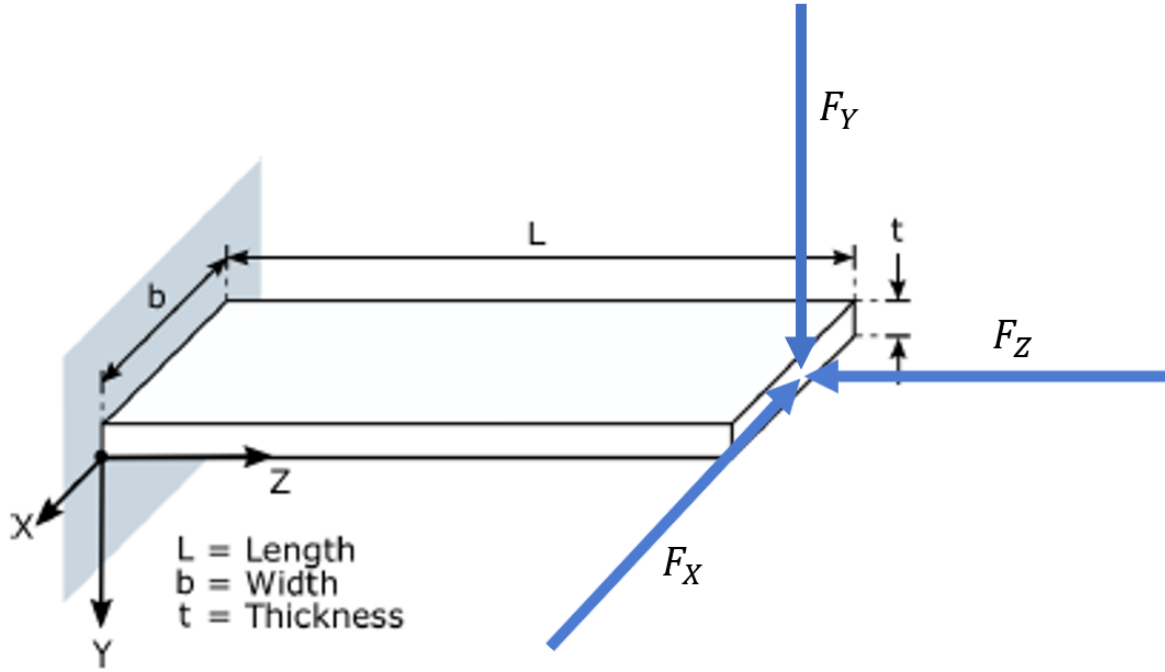


Figure 6.25: Schematic of a flexure blade.

is assumed. The stalk mass is then easily calculated to be 49.3 g. Then, the mounting circle on the spider. Here, the ring on which the hexapod legs are mounted, as outlined in Krikken (2018), is largely reused. This circular structure made of CFRP is resized to have an outer radius of 4.24 cm. Then, with an inner radius of 3.34 cm, a wall thickness of 1 mm and a height of 4 cm, the total mass of this structure is equal to 31.8 g. The flexures and mount are visualised in figure 6.26.

$$\tau = \frac{F}{bt} \quad (6.4a)$$

$$\sigma = \frac{FL}{bt^2/6} \quad (6.4b)$$

$$\sigma_{eq} = \sqrt{\sigma_{xx}^2 + \sigma_{yy}^2 + \sigma_{zz}^2 - \sigma_{xx}\sigma_{yy} - \sigma_{yy}\sigma_{zz} - \sigma_{zz}\sigma_{xx} + 3(\tau_{xy}^2 + \tau_{yx}^2 + \tau_{zx}^2)} \quad (6.4c)$$

A downside of this type of mounting is that it, similar to the hexapod rods, moves the secondary mirror closer to the primary mirror. This means that the booms and the baffle need to be extended by the length of the flexures, so by 6 mm. The additional mass is calculated in the same way as described in section 5.2.1, which leads to an additional mass for the booms and baffle combined of 17.1 g. Furthermore, the flexures are also affected by temperature changes. In assuming that the temperature profile of the flexures looks similar to that of the hexapod rods, a temperature variation of about 30 K can be expected. Ti-6Al-4V has a CTE of $8.6 \mu\text{m}/\text{m}\cdot\text{K}$, leading to a total expansion of $1.55 \mu\text{m}$. This expansion is significant and must be accounted for. This can, for instance, be done by choosing a different flexure material, one with a lower CTE. In using beryllium I-70, another good option as described in Pepper (2018), this expansion can be reduced to $1.13 \mu\text{m}$. This is, however, still too much. Samara-Ratna et al. (2015) describes the possibility of measuring the strain of flexures, but also mentions distinct problems in non-linear expansion of the flexures and high measurement errors. This is in part because of the main function of the flexures, which is flexing. Furthermore, because of the small size of the blades used in this project, it might prove very difficult to apply strain gauges to the flexure blades. Another way to find the expansion is again by measuring the temperature. The expansion of metals is mostly linear[107], so the hysteretic issues found in composite structures are not present. However, errors still arise due to imperfect measurements and because the expansion

itself is not necessarily perfectly aligned with the z-axis. For this reason, a maximum error in predicting the expansion of the flexure blades of $0.1 \mu\text{m}$ is assumed to be present. An additional mass of 27.3 g is also expected because of the need for power cables.

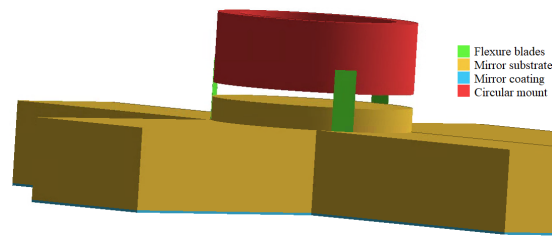


Figure 6.26: Conceptual design of the secondary mirror flexure mount.

To summarise, the total mass of a system employing flexures is 108.6 g. The thermal expansion of the flexures introduces a maximum error of about $0.1 \mu\text{m}$.

6.3.2. Trade-off

Of all concepts discussed above, only the bonded and flexure mounts are considered to be viable options. In choosing the best mounting method for a telescope mirror, simple designs are always preferred over complex designs. Even though flexure mounts provide an elegant solution to many problems typically experienced in mirror design, such as decreasing the stresses in the mirror, a simple design might still be the preferred option if it meets all requirements. In this case, using a bonding agent to mount the secondary mirror is more than sufficient. It firmly attaches the mirror to the spider without introducing excessive stresses in the mirror. What is more, the bonded mount is lighter and does not suffer from thermal expansion in the same way that the flexure mount does. It can therefore confidently be said that in this case, a simple design in which the mirror is bonded to the spider provides the best solution.

7

Verification

The detailed design as presented in chapter 6 has to fulfil all requirements, as seen in appendix A. For this purpose, the verification methodology, as presented in figure 2.21, is followed. All requirements are found in table A.2. Firstly, the bottom-level design is verified. Each component is checked on its performance and whether it can survive all envisioned conditions in section 7.1. Then, a system-level verification is performed in section 7.2. Here, it is verified whether the SMSS provides the required translation and whether it can survive all mission phases. The chapter is concluded by looking at the entire telescope. Does it meet all requirements, and does it have the desired functionality? For further verification, an elaborate testing campaign for each component and the system as a whole is required. However, this verification effort remains entirely in the analytic domain, because setting up and performing the required tests is time-consuming and cannot reasonably be done within the time-line of this thesis. The compliance to all relevant requirements is presented in table A.3.

7.1. Component verification

The main focus of this section lies on verifying that each component provides the required performance and can survive all conditions experienced during the entire lifetime of the telescope. Specifically, each component has to withstand a quasi-static acceleration of 30 G simultaneously applied in the X + Y, Y + Z and Z + X directions and survive the extreme temperatures experienced during the LEOP. Furthermore, each component shall operate in a vacuum at the nominal temperatures found during normal operation. Lastly, each component has to operate for at least five years. The components considered in this verification effort are the ones that were designed in this thesis, namely the IDS, the linear piezo actuators and the bonding between the secondary mirror and the spider. Each component, in theory, provides the functionality for which they are meant. The piezo actuators can provide linear actuation with the required accuracy, the secondary mirror bonding securely attaches the mirror to the spider without introducing too high stresses, and the DMI can, in theory, measure the displacement of each deployment leg with the required accuracy. Without a further testing campaign, the performance of each component cannot further be verified. Therefore, for now, the performance of these components as provided by the manufacturers has to suffice. That being said, the components can be checked for whether they can survive the harsh conditions of space. M2-MEC-25 specifies the loads that each component has to withstand. These loads are calculated in chapter 6, and all components were shown to be able to withstand these loads.

Besides the experienced loads, the components also have to withstand the extreme temperatures experienced. In qualifying each component, temperature margins have to be taken into account, such as shown in figure 7.1. For the DST preliminary design, a qualification margin of 5 K is accepted. The minimum and maximum temperatures of each component during normal operation were found from the ESATAN model. For the temperatures during LEOP, a new model was made. As addressed in figure 3.1, the exact configuration of the booms and baffle in stowed configuration is, as of September 2020, not known. The used ESATAN model therefore consists of a simplified version of the DST in

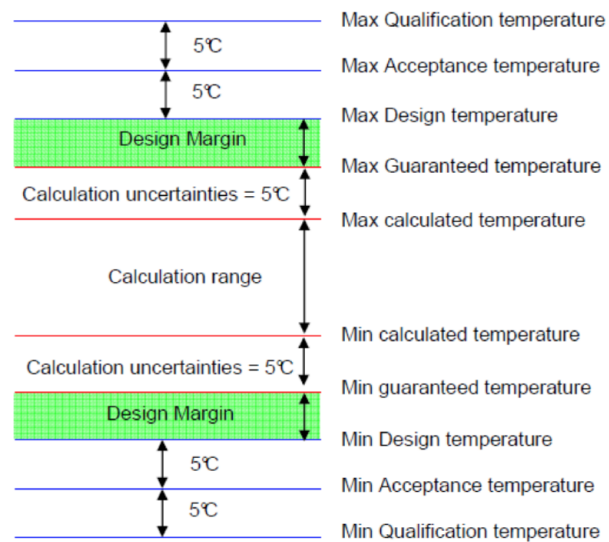


Figure 7.1: Temperature design margins. Retrieved from Arink (2019) as cited from NASA (2009).

stowed configuration, as shown in figure 7.2. In stowed configuration, the baffle is folded to become three times smaller. However, the way in which it is folded is not known. In the stowed ESATAN model, the baffle length and width were therefore simply made three times smaller with a thickness that is three times higher. This real configuration is thus assumed to approach a baffle which is three times smaller, three times thicker, and with a through conductance three times lower than the deployed baffle. The same was done for the booms. The length of the booms was decreased threefold, and the thickness was tripled. Of course, this is not a perfect representation, but the main system parameters, such as the total mass, stay the same. Furthermore, the purpose of this representation is to find the temperature of the components designed in this thesis. Therefore, if their location and coupling with other components are correct, as is the case here, the model should approach the correct temperature results.

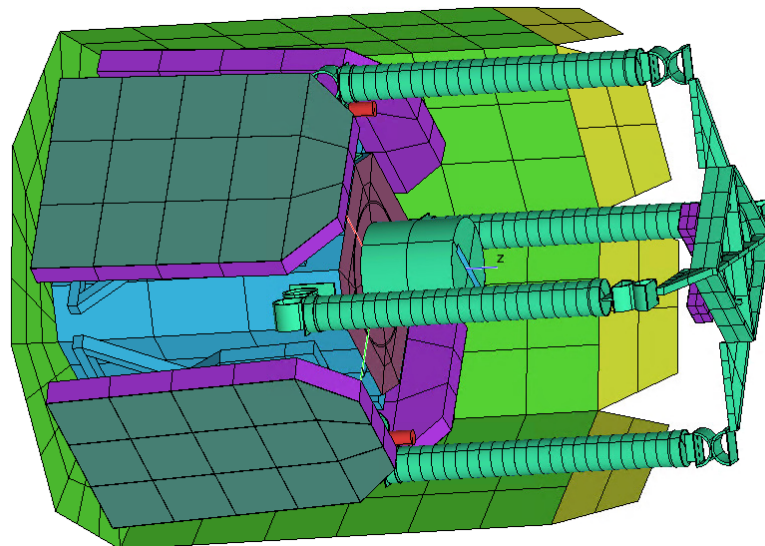


Figure 7.2: Simplified version of DST in stowed configuration, as made in ESATAN TMS.

The hottest and coldest temperature profiles experienced during LEOP of respectively the piezo actuators and the IDS laser head are shown in figures 7.3a and 7.3b. As opposed to earlier results[2, 4], the temperature of these parts does not reach extreme values. This is because, in earlier analyses, the baffle was omitted entirely during the LEOP. In reality, it provides even more protection from the

environment because it is effectively thicker. Cedrat's piezo actuators can typically survive temperatures between $-40\text{ }^{\circ}\text{C}$ to $+80\text{ }^{\circ}\text{C}$, but can also be made to withstand temperature down to cryogenic levels[76]. With a maximum temperature of $20\text{ }^{\circ}\text{C}$ and a minimum temperature of $-28\text{ }^{\circ}\text{C}$, the temperature of the piezo actuators falls within the qualification margin. Attocube's optical heads typically survive temperatures from $-100\text{ }^{\circ}\text{C}$ to $+50\text{ }^{\circ}\text{C}$, so with a minimum and maximum temperature of $-1\text{ }^{\circ}\text{C}$ and $+10\text{ }^{\circ}\text{C}$, this does not pose any problems. The last components of concern are the bonds between the mirror and spider. Because the secondary mirror can reach relatively high temperatures, the bonds also typically have high temperatures. During LEOP, the minimum and maximum temperatures range from $+31\text{ }^{\circ}\text{C}$ to $+69\text{ }^{\circ}\text{C}$. The Epoxy 2216B/A bonds can survive temperatures from $-55\text{ }^{\circ}\text{C}$ to $+150\text{ }^{\circ}\text{C}$, so these can also survive the LEOP. All designed components can, with wide margins, survive the experienced temperatures. All three components can also be made radiation-hardened and operate within a vacuum environment, and can thus withstand the set of environmental conditions experienced during LEOP and nominal operation. The piezo actuators and the bonds are furthermore designed to operate for at least the lifetime of the telescope. With the DMI not yet being developed for space use, this part cannot fully be verified. Such verification activities will be part of future work. With the individual components being designed to withstand the quasi-static launch loads, all components except for the DMI can be said to meet M2-MEC-25 and M2-SYS-08.

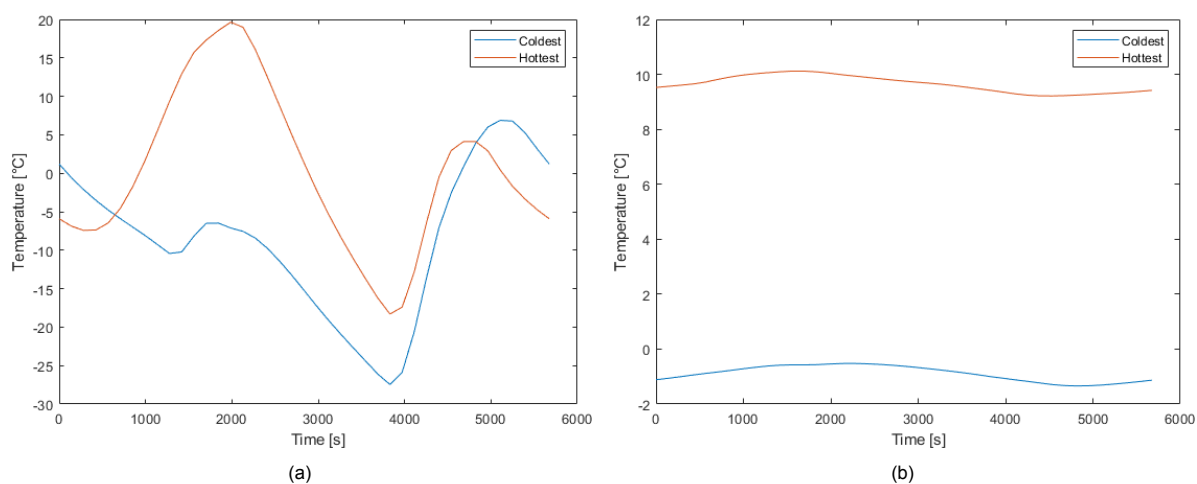


Figure 7.3: Hottest and coldest temperature profiles during LEOP of a) the piezo actuators and b) the IDS laser heads.

7.2. System verification and validation

With the component-level verification finished, the adherence to all (sub) system-level requirements is checked. Some of the main SMSS parameters are its mass and volume. M2-SYS-01 specifies that the M2 mechanism shall be lower than 14 kg. Currently, the combined mass of all components of the SMSS is estimated to be 9.53 kg. In taking a mass margin of 20% to account for uncertainties in the design, as previously used in this project[109], the system mass is 11.44 kg, meaning the mass requirement is met. The volume of the SMSS cannot be seen on its own, as it is only part of the volume of the entire telescope. M2-SYS-04 can, therefore, only be verified when the redesign of the baffle is finished. Besides these main system parameters, the requirements regarding the translation and rotation of the secondary mirror, as outlined in M2-MEC-10 to M2-MEC-15, are checked in section 7.2.1. This check is followed by a discussion on the mechanical performance of the entire SMSS in section 7.2.2.

7.2.1. Verification of the translation and rotation budgets

In changing some components of the SMSS, the temperature variation of the entire structure and that of individual components changes. This, in turn, means that the longitudinal translation of the secondary mirror changes. To verify that the translation stays within budget, the temperature of the SMSS is again simulated in ESATAN. This results in the longitudinal translation of each deployment leg shown in figure 7.4. The maximum expansion of each leg has gone down from a value of about $85\text{ }\mu\text{m}$ to about $80\text{ }\mu\text{m}$. This can be explained by the fact that the booms were made shorter because the hexapod

mount was removed. With a total stroke capability of $126 \mu\text{m}$, the APA100M linear piezo actuators are capable of providing the required stroke. Besides the total stroke, the accuracy of the actuation is critical to keep the secondary mirror within the necessary budgets. The accuracy of the secondary mirror positioning is largely determined by the accuracy of the translation prediction and the accuracy of the actuators. The accuracy in predicting the translation of the secondary mirror is, as discussed in section 6.2, equal to $0.5 \mu\text{m}$. With a good closed-loop positioning control algorithm the accuracy goes down to the resolution of the actuator, as shown in figure 6.4. The achievable resolution of the APA100M is, so the accuracy is also 7 nm .

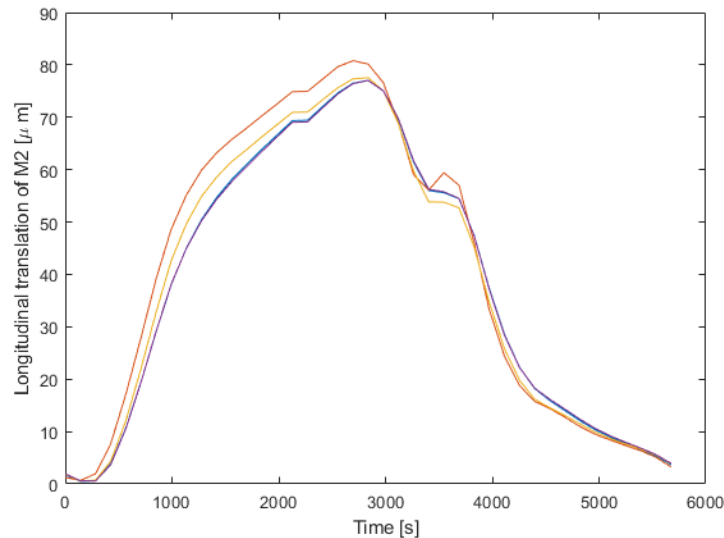


Figure 7.4: Verified longitudinal translation of each deployment leg.

There is, however, one additional source of uncertainty which was not discussed before, which is the temperature of the secondary mirror. The secondary mirror consists of a cylindrical part with thickness t_{SM} and a circular part with a radius of curvature R_C , as visualised in figure 2.20. Even though the thickness (40 mm), in-orbit main-body temperature variation (1.06 K) and CTE ($2.2 \mu\text{m}/\text{m}\cdot\text{K}$) are relatively low, the thickness still varies due to thermal expansion of the material. This thickness variation is largely homogeneous and is shown in figure 7.5. The total in-orbit thickness variation of the secondary mirror is shown by the blue line, and reaches a maximum of $0.076 \mu\text{m}$. This variation can be predicted by placing temperature sensors at the backside of the mirror. Taking in account random sensor errors of 0.1 K , common for high accuracy thermistors[86, 110], the error in the secondary mirror thickness variation prediction goes down to the yellow line in figure 7.5, with a maximum of $0.009 \mu\text{m}$. However, because the maximum in-orbit thickness variation of the secondary mirror is only $0.076 \mu\text{m}$, which should not pose any problems, and because adding temperature sensors at the backside of the mirror would significantly increase the complexity of the system, the error induced by the thickness variation of the secondary mirror is accepted as is. If, in the future, the uncertainty in the positioning of the secondary mirror turns out to be too large, this can still be changed. The total secondary mirror longitudinal placement uncertainty is then equal to the accuracy in measuring the leg expansion, the actuator accuracy and the secondary mirror thickness variation uncertainty and equals $0.5826 \mu\text{m}$. This is well below the budget of $2 \mu\text{m}$, meaning requirement M2-MEC-12 is met. This, however, does not yet consider the change in radius of curvature of the circular part of the mirror, which shall change at most 0.0001% in-orbit, as specified in M2-MEC-16. The maximum in-orbit temperature variation of the circular bottom-part of the secondary mirror, as found from ESATAN, is about 1.01 K . This temperature change induces a change in radius of curvature according to equation (2.5) of 0.00022% , meaning that M2-MEC-16 is not met. A low-level attempt to solve this issue was made, namely by looking into the conduction through the bonding agents between the secondary mirror and spider. However, neither increasing nor decreasing the conduction significantly decreases the temperature variation, the temperature curve is only shifted up or down. Recommendations regarding this issue are presented in chapter 9.

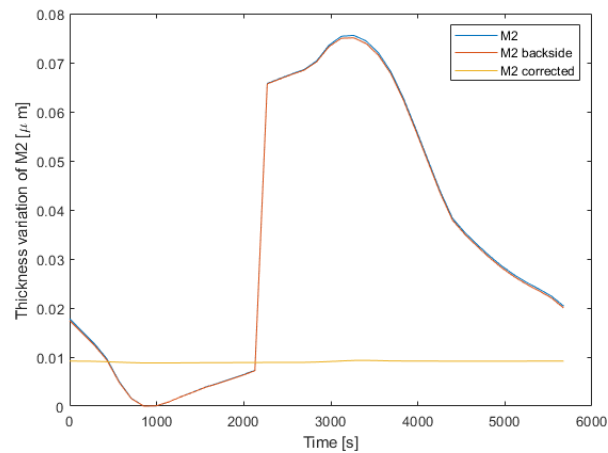


Figure 7.5: Verified thickness variation of secondary mirror.

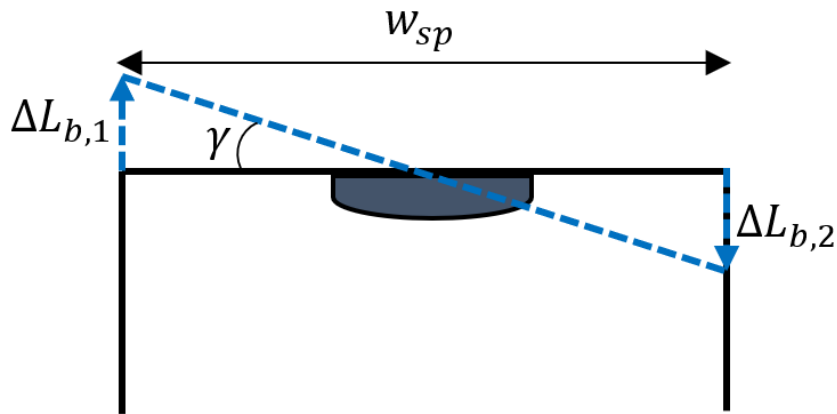


Figure 7.6: Rotation of secondary mirror caused by differences in temperature between deployment legs.

7.2.2. Structure mechanical verification

With the analytic calculations showing that the piezo actuators and bonds can withstand the quasi-static launch forces, a system-wide mechanical analysis is required to show that the entire structure can withstand these loads. The system should furthermore adhere to M2-MEC-25-04, specifying that the natural frequency of the stowed mechanism shall be higher than 100 Hz. However, earlier analysis has already shown that the structure, as of the design of Krikken[3], does not meet the vibrational requirements. Furthermore, with the baffle and SMSS overlapping in the stowed configuration, as shown in figure 3.1, these designs need to be updated. Because these issues still need to be addressed in future theses, a full-scale mechanical analysis is futile at this point of the design procedure. The mechanical system verification is therefore left to the attention of future team members.

7.2.3. System validation

With each component and the SMSS verified as far as possible, the entire system is checked on its functionality. This last check should be seen as a sanity check on the design. The required functionality of the SMSS is described in section 3.1.1 as follows:

The function of the SMSS is to deploy the secondary mirror to its desired position and keep it there within the specified budgets.

The former part of this functionality is achieved by means of the CORE hinges and the deployment booms, which are not part of this thesis. The latter part is. By measuring the displacement of the

secondary mirror and longitudinally actuating each spider leg, the secondary mirror stays in its desired position within the specified budgets. The performance as required from this thesis is therefore verified and validated within the analytical domain.

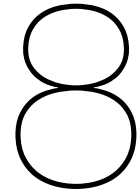
7.2.4. Sensitivity analysis

As described in section 3.1.2 and specified in MIS-REQ-14, the telescope might in the future be changed to a thermal infra-red sensing telescope instead of a telescope operating in the visible spectrum. MIS-REQ-14 specifies that all technologies used shall also be usable in a thermal infra-red telescope. This requirement is met, because the technologies used do not interfere with the functionality of an infra-red telescope. However, a change to an IR telescope also entails changes in the scope of the design. Furthermore, the iterative nature of the project might mean that a change in SMSS is required due to other design decisions. For both these reasons, it is important that the SMSS design is not sensitive to system design changes. Such system changes might lead to changes in the thermal environment and the translation and rotation budgets.

In principle, the system designed in this thesis is very insensitive to such changes. A change in thermal environment might lead to different minimum and maximum temperatures of the components or a change in total translation of the secondary mirror. The components used all easily fall within the thermal qualification margins. If the temperature profile of one of the components does change too much, thermal control can be applied to the component in question, or a different component with better temperature qualifications can be chosen. A change in total translation of the secondary mirror leads to change in required actuator stroke. The APA100M was chosen in this thesis because of its good fit with the required stroke. However, many other linear piezo actuators, or indeed also other types of actuators, with different strokes are commercially available. A change in design due to a change in required stroke therefore simply entails choosing a different actuator.

If the telescope is changed to an infra-red sensing telescope, the in-orbit drift budgets can probably be relaxed (personal communication, D. Dolkens & H. Kuiper, 29 July 2020). This means that the design is not sensitive to such a change. Furthermore, the current design keeps all translations within $0.5826 \mu\text{m}$ of the desired translation. Some small design changes can decrease this accuracy to $0.5 \mu\text{m}$. This means that the design even allows for the in-orbit budgets to change down to $0.5 \mu\text{m}$. This value of $0.5 \mu\text{m}$ is mostly based on the uncertainty of the DMI at a distance of 1.6 m.

Concluding, the designed system is easily adaptable to changing telescope requirements. If a change is required, the thermal models and frameworks developed in this thesis can be adapted to find a new design. Such a new design might slightly differ in its mass and power consumption, but because the current design leaves some room to play in these regards, this should not pose a problem.



Results & Conclusion

In the previous chapter, all steps to come to the final verified design were discussed. Here, the results and main conclusions are presented. The main goal of this chapter is to answer the research questions presented in section 2.5.2, starting with the main research question in section 8.1. This is followed by answering the sub-questions in section 8.2.

8.1. Main design

This goal of this section is to answer the main research question, which was posed as follows:

What is the best feasible design of the secondary mirror support structure that adheres to all requirements?

The best feasible design, as defined in this thesis, consists of three parts; The secondary mirror actuation, displacement measurement and mirror mount. An overview of the SMSS is shown in figure 8.1. Here, A shows the location of the piezo actuators, B the location of the DMI laser heads and C the location of the DMI reflector. The entire SMSS plus the secondary mirror has a mass of 9.53 kg and a power consumption of 9 W. The design itself is described in this section, with the reasoning behind the design choices presented in the following sections.

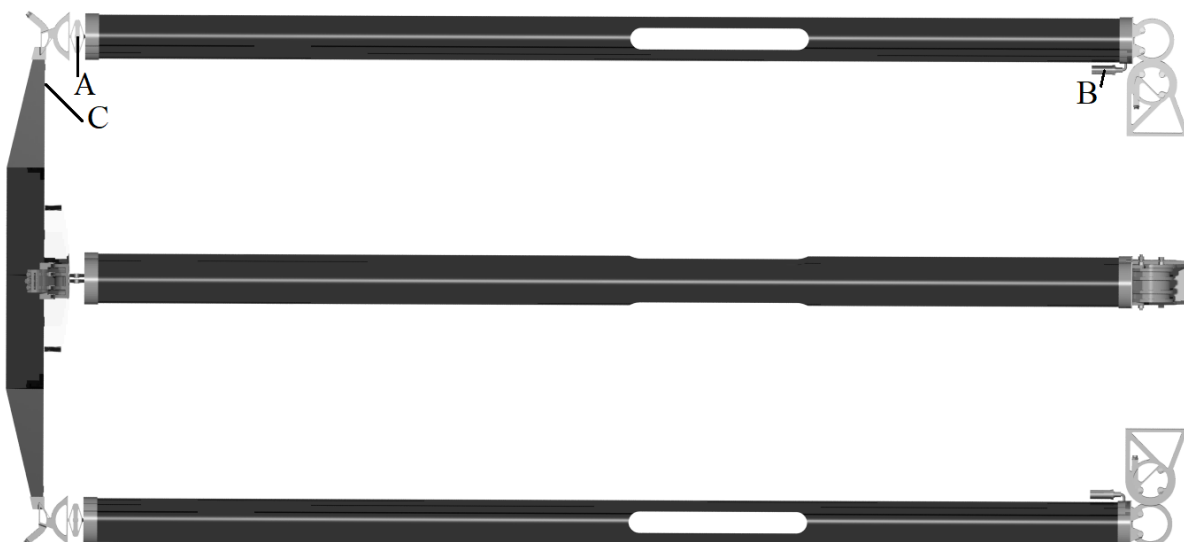


Figure 8.1: Design render of the secondary mirror support structure. The piezo actuators are located at A, the DMI laser heads at B and the laser reflector at C.

8.1.1. Secondary mirror actuation

The secondary mirror is actuated by means of four linear piezo actuators placed in between the booms and the CORE hinges, as shown in figure 8.1. The actuators in question are the APA100M, shown in figure 8.2, as provided by Cedrat Technologies.[71] Combined with integrated strain gauges, the APA100M can provide a stroke of up to $130\ \mu\text{m}$ with a repeatability better than $0.1\ \mu\text{m}$. The actuators are controlled by two CCBu20 control units. These controllers provide the high-voltage power required by the actuators. The total system has a mass of 220.6 g and a nominal power draw of 1 W.

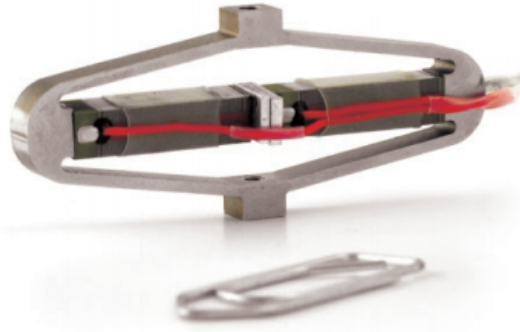


Figure 8.2: The APA100M amplified piezo actuator. Retrieved from Cedrat Technologies (2019).

8.1.2. Displacement measurement

To be able to provide the required actuation, precise displacement information is required. This information is provided by a DMI, a displacement measuring interferometer. The design is based on the nominal parameters of the IDS as provided by Attocube.[98] However, because this apparatus is not space-qualified, this design may vary in the future. The concept consists of four sensors heads, located at the base of each boom, as denoted by B in figure 8.1. The manner by which they are attached to telescope may vary because the exact configuration of the telescope is not yet known. They can either be attached directly to the instrument housing or to the end cap of the booms, where the latter is currently shown in the design render. The sensor heads produce a laser which is reflected back into the laser heads by four reflectors placed on each spider leg, as denoted by C in figure 8.1 and figure 8.3. The collected information is then sent to the main body. Here, it is analysed, and the displacement of each spider leg is calculated with an uncertainty of at most $0.5\ \mu\text{m}$. The total displacement measuring system has a preliminary mass of 1014 g and a power consumption of 8 W.

8.1.3. Secondary mirror mount

The secondary mirror is mounted onto the spider bottom plate by means of epoxy 2216B/A applied on four locations along the 0.7-zone of the mirror, so at 0.7 times the radius, as shown by the orange circles denoted by D in figure 8.3. The spider bottom plate is supported by a circular structure within the spider with the same radius as the 0.7-zone. This type of mount removes thermal translation uncertainties introduced by the previously used hexapod structure. Furthermore, because of the similar CTE of the spider and secondary mirror, the stresses in both the bondings and the mirror stay well below the stress limits. In total, the added mass of this mount is 68 g. Taking into account the lower mass of the booms because of their decrease in length, this means a decrease in mass of about 50 g.

8.2. Rationale behind design

With the main research question answered in section 8.1, the sub-questions are answered here. The main purpose of this section is to provide the reasoning behind the design choices made throughout this thesis. This section is logically structured along the research questions, as presented in table 8.1.

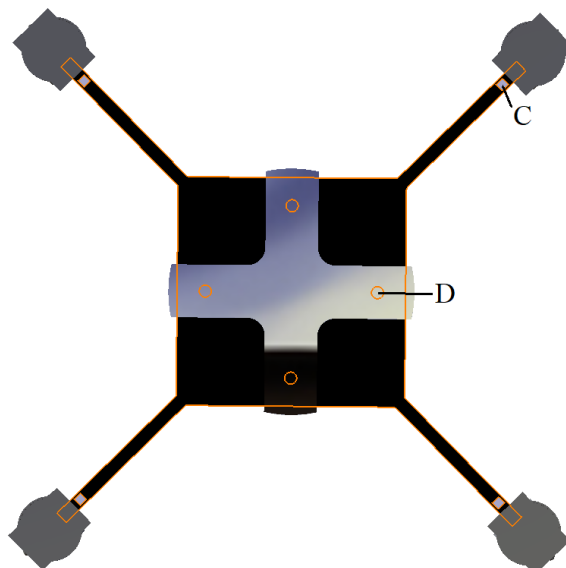


Figure 8.3: Design render of the spider. C Denotes the DMI reflector and D denotes the location of the bonds between the secondary mirror and spider.

Table 8.1: DST research questions.

ID	Research question
SUB-1	What requirements should the SMSS adhere to?
SUB-1.1	What functionality should the SMSS have?
SUB-1.2	What defines the feasibility of the design?
SUB-1.3	What requirements follow from the functionality and feasibility?
SUB-2	What concept should the design of the SMSS be based on?
SUB-2.1	What are the main input parameters on which the design is based?
SUB-2.2	What concepts can potentially meet the requirements?
SUB-2.3	What do these concepts look like?
SUB-2.4	Which concept has the best performance?
SUB-3	Can the design of the SMSS feasibly be implemented within the DST ?
SUB-3.1	What are the main system parameters?
SUB-3.2	Does the design meet all requirements?
SUB-3.3	Does the design have the desired functionality?

8.2.1. What requirements should the SMSS adhere to?

The requirements posed on the SMSS flow down from its main functionalities. These main functionalities consist of first deploying the secondary mirror to its desired location and then keeping it there. The secondary mirror has to be deployed at a distance of 1.6 m in front of the primary mirror along the optical axis of the telescope. Then, during operation, the maximum deviation from this position and orientation is defined by the in-orbit drift budgets, as given in table 2.4. The SMSS should achieve these feats with a maximum mass of 14 kg. Furthermore, all components have to survive all conceivable environments until the end of the life of the telescope, so after 5 years of operation. The full list of requirements is found in table 2.3.

8.2.2. What concept should the design of the SMSS be based on?

To find the concepts that can potentially meet all requirements, the environments which they first have to survive and then operate in are first defined. The main steps of the mission are the launch, the LEOP and then the operational phase. During launch, the SMSS is exposed to high loads due to launch-induced vibrations. The structure as a whole, and each component individually have to bear

these loads. Then, during LEOP, the SMSS experiences the high vacuum of space and high temperature swings because the baffle is not yet fully deployed. Each component, therefore, has to survive and operate in a vacuum, survive the temperatures during LEOP and operate in the temperatures experienced during the operational phase. The temperatures found during operation, and how these are calculated, are found in chapter 4.

The variation in length of the deployment booms and CORE hinges due to the temperature variations of these components, as found from the thermal analysis, acted as the main input parameters of the design. Multiple design options were considered, of which a passive athermalisation approach was used as the starting point. If such a passive approach could be shown to keep the secondary mirror position variation within all budgets, this would surely be the optimal solution. It, however, turned out that the thermal expansion of the deployment legs was far too large to be compensated passively, so other concepts were considered in chapter 5. Of all concepts, three were selected to be potentially viable. The first of these three concepts consists of thermo-mechanically actuating the hexapods as designed in Krikken (2018). The second and third concept both provide the actuation of the secondary mirror mechanically, the former by directly actuating the secondary mirror and the latter by actuating the entire spider. The first concept was decided to be unacceptable, because of its inability to provide quick response to temperature changes. Finally, the last concept was chosen. It outperformed the other concept mainly on its mass, volume and stiffness. Furthermore, because each spider leg is essentially kept level, no additional stresses are introduced in the spider.

8.2.3. Can the design of the SMSS feasibly be implemented within the DST ?

To answer this question, the chosen concept was designed in detail in chapter 6. The main results of this design are presented in section 8.1. The compliance with each requirement relevant for this thesis is presented in table A.3 in appendix A. From this table, it is clear that currently, not all requirements are met. However, most requirements that are not met regard the design of the entire SMSS, which was not part of this work. Recommendations regarding these requirements are presented in chapter 9. As for the requirements posed on the components designed as part of this work, a few key conclusions can be drawn. Firstly, the designs of the actuation mechanism and the secondary mirror mount are fully verified in the analytic domain. Furthermore, because the parts on which they are based already have flight heritage, it can confidently be said that their further verification will not pose problems. This is not the case for the displacement measuring interferometer. The working principles behind this apparatus are clear, and there are no reasons to suspect that it will not function in a space-based telescope. However, the parts still need to be designed specifically for this purpose and still require an extensive verification campaign. The question whether the design of the SMSS can feasibly be implemented within the DST is therefore not yet answered and requires further research.

8.3. Main conclusions

With all the research questions answered, it is time to evaluate whether the thesis need and goal are also met. They were presented in section 2.5.2 to be as follows:

Thesis Need

To ensure the optical performance requirements of the Deployable Space Telescope are met, the in-orbit drift budgets may not be exceeded. For this end, there is a need to make sure the relative distance between the primary and secondary mirror is stable over the satellite's orbit.

Thesis Goal

To improve the design of the secondary mirror support structure such that the translations and rotations of the secondary mirror are as low as possible and at least do not exceed the set drift budgets. The design should furthermore adhere to all requirements imposed on the telescope and be feasibly implemented within the scope of the Deployable Space Telescope.

By making use of DMIs to measure the displacement of the secondary mirror and using linear piezo actuators, the main translations and rotations of the secondary mirror are kept within the set budgets. The first part of the thesis goal is therefore met. The second part dictates that the design should adhere

to all requirements and that it can feasibly be implemented. For now, this part is not yet met, because there are, as of now, no DMIs with the capability of operating within a space environment. Under the condition that the DMIs are successfully verified in the future, the design presented in this thesis can feasibly be implemented within the Deployable Space Telescope to make sure the in-orbit drift budgets are met, which means that the thesis need and goals are met. Recommendations regarding these conclusions are presented in chapter 9.

9

Recommendations

Here, some recommendations regarding future work are given. Most directly flow from the conclusions made in chapter 8, some from requirements that are not yet met, as shown in table A.3 and some are based on conclusions made elsewhere in this thesis.

Displacement Measuring Interferometer

A large part of the design presented in this thesis is based on the assumption that DMIs can be applied in space applications and that such components will be ready to use at the time of launch. Additional research on this topic is required. Manufacturers of DMIs should be contacted and queried about their willingness to design and manufacture such components, or, alternately, a working prototype can be designed in-house. If it turns out that the assumptions about the availability of such DMIs were erroneous, the design has to be altered. This can be done by either using one of the concepts proposed in section 6.2 or by for instance applying a stochastic descent algorithm, as is used for the deformable mirror, to position the secondary mirror. Either way, more research, development and hardware testing is required.

Mechanical analysis of SMSS

Each component, as designed in this thesis, is analytically verified to withstand all foreseen launch loads. However, the design of the entire SMSS does not yet meet the requirements regarding in-orbit vibrations. Firstly, an additional design effort has to be made to ensure that the vibrations during imaging stay beneath the vibration budgets. Here, the use of the APA100M linear piezo actuators, or possibly other linear piezo actuators, to stabilise these vibrations should be investigated. When such arrangements are made, and the entire SMSS design is known, the capability of the SMSS structure to withstand all launch loads has to be verified.

Overlapping baffle and SMSS

As identified in this thesis, the current designs of the baffle and SMSS touch each other in stowed position. With the redesign of the baffle by Nagy underway, this might be fixed. However, if not, an additional design effort is required to change the way by which the booms deploy. If this is not possible, an entire redesign of the SMSS is required. In that case, the system work performed in this thesis remains valid; however, with an entirely different deployment system, the exact components used in this thesis might be subject to change.

Component interfaces and cabling

The work in this thesis was focussed on the design of the system as a whole. In doing so, some details were left untouched, like the exact interface between components and the cabling required for the piezo actuators. This design methodology is justified because of uncertainties in other parts of the design, meaning design changes in the future would make designed interfaces dispensable. If these uncertainties, like the touching baffle and SMSS, are cleared out, these interfaces should be designed. These to be designed parts are mainly the interfaces between the piezo actuators, booms and top CORE

hinges, which, by design, can be very simple. The cabling going from the instrument housing to the piezo actuators is another issue. Firstly, provisions should be made to run these cables from the instrument housing to the booms. Furthermore, some research is required to see if, and in what way, these cables can run through the mid-hinge of the booms without interfering with its functionality, so without changing the elastic properties of these hinges. If the cables are deemed to interfere significantly with the functionality of the mid-hinge, the piezo actuators can be relocated to the bottom of the booms. In such an event, the launch loads on the

Curvature change of secondary mirror

Due to temperature variations, the curvature of the secondary mirror is expected to change by 0.00022 %, more than the 0.0001 % allowed by requirement M2-MEC-16. Initial analysis shows that changing the temperature profile of the secondary mirror cannot merely be done by changing the amount of conduction from the mirror to the spider. Furthermore, only homogeneous expansion was considered in the analysis. Local temperature variations might be present, causing local mirror deformations, which further increases the problem. A solution ought to be found either in changing the temperature profile, for instance by looking into the coating of the sides of the mirror, or by changes in the baffle design. Both introduce their own problems and require further analysis. Another solution might lie in increasing the allowed curvature change, either by compensating the curvature change in the instrument housing or possibly by relaxing the requirement.

Verify performance of baffle

The heat flow going through the baffle was calculated using the Doenecke method. This method serves as a reasonable initial estimate, but it does typically have an uncertainty of around 25%. Because of this uncertainty, a 25% higher than calculated conductance is used in the thermal simulations throughout this thesis. If the conductance turns out to be closer to the calculated values, or even lower, the temperature range of the components will decrease. With a decrease in temperature range, the design can possibly be optimised. The baffle performance should therefore be verified by tests, first of the MLI itself and then of the baffle as a whole.

Verify performance of M2 deployment

The SMSS, as designed in Krikken (2018), is a one-of design that should theoretically work. However, none of the main components of the system is individually verified. Full-scale models of each component should be made to do so. If all components individually are tested, the deployment mechanism has to be tested in its entirety to check whether it can reliably deploy and to find the deployment errors.

Verify performance of stabilising system

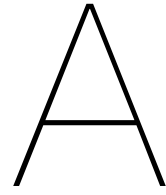
The stabilising system, so the displacement measuring system and the piezo actuators, should undergo full-scale testing to verify their performance in accuracy over the full translation range of the secondary mirror.

Thermal vacuum testing

If all parts of the telescope are individually tested and verified, a full-scale thermal test should be done to verify the performance of the baffle and to check if the estimated component temperatures are in line with actual temperatures.

Satellite parameters & launcher

For now, the design of the DST has been focussed only on the telescope. With some of the main parts of the telescope design nearing completion, the overall system parameters of the telescope should be defined. A suitable satellite has to be designed around this, and a launcher has to be selected.



DST mission & Secondary Mirror Support Structure requirements

Table A.1: DST mission requirements.

ID	Description
MIS-REQ-01	The GSD of the instrument shall be equal to 25 cm in the panchromatic band from an orbital altitude of 500 km.
MIS-REQ-02	The swath width of the instrument shall be wider than 1 km (threshold) / 5 km (goal).
MIS-REQ-03	The system shall have one panchromatic channel from 450 to 650 nm with a 25 cm GSD at an altitude of 500 km.
MIS-REQ-04	<p>The system shall have four multispectral bands with the wavelength ranges and GSD indicated at an altitude of 500 km:</p> <ul style="list-style-type: none"> • Blue (450 - 510 nm) - 100 cm • Green (518 - 586 nm) - 100 cm • Yellow (590 - 630 nm) - 100 cm • Red (632 - 692 nm) - 100 cm
MIS-REQ-05	The SNR of the instrument shall be higher than 100 for a reflectance of 0.30 and a sun Zenith angle of 60°.
MIS-REQ-06	The nominal MTF at both the Nyquist frequency and half the Nyquist frequency shall be higher than 5% (threshold) / 15% (goal).
MIS-REQ-07	After calibration, the residual Strehl ratio of the system shall be higher than 0.80.
MIS-REQ-08	The mass of the instrument shall be lower than 100 kg (threshold) / 50 kg (goal).
MIS-REQ-09	In the stowed configuration, the volume of the instrument shall not exceed 1.5 m ³ (threshold) / 0.75 m ³ (goal).
MIS-REQ-10	The DST shall not use any ITAR controlled components or technology.
MIS-REQ-11	The DST shall be designed for compatibility with the TBD launcher.
MIS-REQ-12	The DST shall comply with national (NL) and international regulations during AIT activities, launch, operations and end of life.
MIS-REQ-13	The DST shall have a lifetime of at least 5 years.
MIS-REQ-14	All technology used in the DST shall be usable both when a visible as well as a thermal infra-red telescope concept is chosen.
MIS-REQ-15	The system shall not include parts that require new production methods.
MIS-REQ-16	The system shall use simple reproducible parts.

Table A.2: SMSS requirements.

ID	Description
M2-SYS-01	The total mass of the M2 mechanism shall be lower than 14 kg.
M2-SYS-02	The mechanism shall provide structural support for M2.
M2-SYS-03	The SMSS in stowed configuration shall stay within the boundary box of the stowed baffle.
M2-SYS-04	The stowed SMSS and baffle shall combined not have a volume higher than 0.75 m ³ (goal)/ 1.5 m ³ (threshold).
M2-SYS-05	The development, production, assembly, integration, and test cost of the M2 mechanism shall be equal to or lower than TBD.
M2-SYS-06	The M2 mechanism shall not contain ITAR related components.
M2-SYS-07	The mechanism shall comply with the Guiana Space Centre safety regulations.
M2-SYS-08	The lifetime of the SMSS shall be at least 5 years.
M2-MEC-01	The M2 mechanism shall deploy the M2 along the optical axis (Z axis) to obtain a distance of 1.6 m between M1 and M2, measured between the vertex of both mirrors.
M2-MEC-02	The M2 mechanism deployment accuracy shall be equal to or less than 15µm measured along the X-axis of the telescope coordinate frame.
M2-MEC-03	The M2 mechanism deployment accuracy shall be equal to or less than 15 µm measured along the Y-axis of the telescope coordinate frame.
M2-MEC-04	The M2 mechanism deployment accuracy shall be equal to or less than 10 µm measured along the optical axis (Z-axis) of the telescope coordinate frame.
M2-MEC-05	The M2 mechanism deployment accuracy shall be equal to or less than 100 µrad measured around the X-axis of the telescope coordinate frame.
M2-MEC-06	The M2 mechanism deployment accuracy shall be equal to or less than 100 µrad measured around the Y-axis of the telescope coordinate frame of the telescope coordinate frame.
M2-MEC-07	The M2 mechanism deployment accuracy shall be equal to or less than 100 µrad measured around the optical axis (Z-axis of the telescope coordinate frame).
M2-MEC-08	The radius of curvature of the M2 mirror shall change less than 0.01 % due to the deployment of the mechanism.
M2-MEC-09	The shape error of the M2 shall be less than 25 nm due to the deployment of the mechanism.
M2-MEC-10	The M2 mechanism in-orbit drift shall be equal or less than 4 µm measured along the X-axis of the telescope coordinate frame.
M2-MEC-11	The M2 mechanism in-orbit drift shall be equal or less than 4 µm measured along the Y-axis of the telescope coordinate frame.
M2-MEC-12	The M2 mechanism in-orbit drift shall be equal or less than 2 µm measured along the optical axis (Z-axis of the telescope coordinate frame).
M2-MEC-13	The M2 mechanism in-orbit drift shall be equal or less than 6 µrad measured around the X-axis of the telescope coordinate frame.
M2-MEC-14	The M2 mechanism in-orbit drift shall be equal or less than 6 µrad measured around the Y-axis of the telescope coordinate frame.

Table continues on next page...

... table continues on this page.

M2-MEC-15	The M2 mechanism in-orbit drift shall be equal or less than 12 μ rad measured around the Z-axis of the telescope coordinate frame.
M2-MEC-16	The radius of curvature of the M2 mirror shall change less than 0.0001 % due to in-orbit drift.
M2-MEC-17	The shape error of the M2 shall be less than 5 nm due to in-orbit drifts.
M2-MEC-18	The M2 mechanism stability shall be equal to or less than 1 μ m along the X-axis of the telescope reference frame.
M2-MEC-19	The M2 mechanism stability shall be equal to or less than 1 μ m along the Y-axis of the telescope reference frame.
M2-MEC-20	The M2 mechanism stability shall be equal to or less than 0.5 μ m along the Z-axis of the telescope reference frame.
M2-MEC-21	The M2 mechanism stability shall be equal to or less than 1.5 μ rad around the X-axis of the telescope reference frame.
M2-MEC-22	The M2 mechanism stability shall be equal to or less than 1.5 μ rad around the Y-axis of the telescope reference frame.
M2-MEC-23	The M2 mechanism stability shall be equal to or less than 3 μ rad around the Z-axis of the telescope reference frame.
M2-MEC-24	The deployed mechanism shall have a minimum natural frequency of 5 Hz.
M2-MEC-25	The M2 mechanism shall be able to survive launch in the stowed configuration. Survival is defined as no impairment to the nominal functional capabilities of the system resulting from exposure to a given set of environmental conditions.
M2-MEC-25-01	The M2 mechanism shall be able to survive a quasi static acceleration of 30 G simultaneously applied in the X- and Y-direction in the telescope coordinate frame.
M2-MEC-25-02	The M2 mechanism shall be able to survive a quasi static acceleration of 30 G simultaneously applied in the Y- and Z-direction in the telescope coordinate frame.
M2-MEC-25-03	The M2 mechanism shall be able to survive a quasi static acceleration of 30 G simultaneously applied in the X- and Z-direction in the telescope coordinate frame.
M2-MEC-25-04	The stowed mechanism shall have a minimum natural frequency of 100 Hz.
M2-MEC-26	The M2 system shall not come in contact or interfere with other subsystems during any mission phase.
M2-MEC-26-01	The M2 mechanism in stowed configuration shall not interfere with the interface between the launcher and the spacecraft.
M2-MEC-26-02	The M2 mechanism, with the exception of the spider, shall not block the light path of the M1 or M2 mirrors.
M2-MEC-26-03	The width of the spider of the M2 mechanism shall be 15 mm or less, covering no more than 3 mm of mirror of each segment.
M2-MEC-26-04	The M2 mechanism shall be connected to the outside of the instrument bus.
M2-MEC-26-05	The parts of the M2 mechanism covering part of the light path of the mirrors shall have a regular, predictable shape that minimises scattering.
M2-MEC-26-06	The M2 system shall not interfere with the field stop, extending 120 mm from the M1 vertex.
M2-MEC-27	The components shall be able to be assembled without interfering with other systems.
M2-MEC-28	The system shall be able to be tested on ground multiple times without the need to change permanently locked components.

Table A.3: Compliance to requirements.

Requirement ID	Compliance	Comment
M2-SYS-01	Compliant	The mass of the SMSS is, with margin, 11.44, so below the 14 kg requirement.
M2-SYS-02	Compliant	The secondary mirror is indeed supported structurally.
M2-SYS-03	Not compliant	For now, the SMSS does not fit within the baffle. The upcoming redesign of the baffle by Nagy might fix this.
M2-SYS-04	TBD	The volume is determined by the combination of the baffle and the SMSS. The redesign of the baffle by Nagy will determine whether this requirement is fulfilled.
M2-SYS-05	TBD	The cost of the SMSS as a whole and each component individually is not yet determined, nor is the cost requirement itself determined.
M2-SYS-06	Compliant	In selecting each component only European manufacturers were used as to avoid ITAR regulations.
M2-SYS-07	TBD	Not yet determined.
M2-SYS-08	TBD	Each component was chosen to last for at least 5 years. The DMI still has to be designed and its performance verified to check this requirement.
M2-MEC-12, -13, -14	Compliant	The combination of longitudinal actuation and displacement measurement keeps these values within budget.
M2-MEC-10, -11, -15	TBD	A further mechanical analysis is required to check this requirement.
M2-MEC-16	Not compliant	The radius of curvature changes by 0.00022 %, more than the allowed 0.0001 %.
M2-MEC-18 to -23	Not compliant	The current SMSS design, as proposed by Krikken, does not meet these requirements.
M2-MEC-24	TBD	A further mechanical analysis is required to check this requirement.
M2-MEC-25	TBD	Each component was selected to meet this requirement. To verify that the whole SMSS meets this requirement, a further mechanical analysis is required.
M2-MEC-26	Not compliant	For now, the SMSS does not fit within the baffle. The upcoming redesign of the baffle by Nagy might fix this.
M2-MEC-26-01	TBD	The launch interface is not yet determined.
M2-MEC-26-02	Compliant	Each component and the entire SMSS was designed such that the light-path is not blocked.
M2-MEC-27	TBD	The way in which the components are assembled is not yet determined.
M2-MEC-28	TBD	No permanently locked components are used. To verify this requirement the SMSS design must first be completed.

B

ESATAN inputs

Table B.1: Input for ESATAN-TMS. Adapted from Arink (2019).

Parameter	Value	Unit
Environment		
Sun-Planet System		
Planet Radius	6371000	m
Gravitational Acceleration	9.798	m/s ²
Sun Planet Distance	147 · 10 ⁶ - 152 · 10 ⁶	km
Solar Declination	± 23.45	degree
Sun's Right Ascension	0	degree
Orbital Precession	0	degree/s
Sun Radius	695800 · 10 ³	m
Celestial Body Image	Earth	-
Sun Specific		
Sun Temperature	5778	K
Solar Constant Override	0	W/m ²
Sun Rays	Parallel Rays	-
Sun Distance Override	0	m
Planet Albedo		
Method	Uniform	-
Albedo	Longitudinally varied per month	-
Planet Temperature		
Method	Uniform	-
Temperature	Longitudinally varied per month	K
Infra-Red Emissivity	1	-
Orbit		
Ellipse		
Eccentricity	0	-
Semi-Major Axis	6871000	m
Altitude of Apogee	500000	m
Altitude of Perigee	500000	m
Inclination	97.4	degrees
Right Ascension	-22.5	degree
Argument of Periapsis	0	degree
Arc		
Initial True Anomaly	0	degree
Final True Anomaly 360 degree		
Positions		
Angle Gap	20	degree
Number of Positions	18	-
True Anomalies Vector	-	degree
Eclipse Entry Exit Points	Off	-
Pointing		
Primary Pointing		
Pointing Vector	[0.0, 0.0, 1.0]	-
Pointing Direction	NADIR	-
Secondary Pointing		
Pointing Vector	[0.0, 1.0, 0.0]	-
Pointing Direction	NORMAL TO ORBIT	-
User Defined Movement		
Phi/Psi/Omega	0.0	degree
Phi/Psi/Omega Rotation Rate	0	degree/s
Spacecraft Movement		
Type	None	-

Table B.2: Conduction between different components as used in the ESATAN TMS models.

Component 1	Component 2	Conductance [W/K]
Boom	Boom endcaps	2.77
Spider	Spider endcaps	0.89
Spider	Rod	0.94
Rod	Secondary mirror	$2.4 \cdot 10^{-3}$
Core hinge top cam	Core hinge bottom cam	0.20
Primary mirror support structure	Instrument housing	$1.4 \cdot 10^{-2}$
Primary mirror support structure	Primary mirror	$4.8 \cdot 10^{-3}$
Root core	Root core baseplate	$1.6 \cdot 10^{-2}$
Root core	Boom endplate	0.34
Instrument housing bottom	Instrument housing side	1.3

Bibliography

- [1] D. Dolkens. A deployable telescope for sub-meter resolutions from micro satellite platforms. Master's thesis, Delft University of Technology, 2015.
- [2] S. Pepper. Primary mirror fine positioning mechanism. Master's thesis, Delft University of Technology, 2018.
- [3] A. Krikken. Design of the secondary mirror support structure. Master's thesis, Delft University of Technology, 2018.
- [4] J. W. Arink. Thermal-mechanical design of a baffle. Master's thesis, Delft University of Technology, 2019.
- [5] DigitalGlobe. WorldView-4. URL <https://content.satimagingcorp.com.s3.amazonaws.com/static/satellite-sensor-specification/WorldView-4-Satellite-Specifications>. Last accessed 27 August 2020.
- [6] Marcia Smith. ENHANCED VIEW NEWS NOT SO ROSY FOR GEOEYE, june 2012. URL <http://spacepolicyonline.com/news/enhancedview-news-not-so-rosey-for-geoeye/>. Last accessed 27 August 2020.
- [7] Mordor Intelligence. Sattelite-based earth observation market - growth, trends and forecast (2019 2024). Technical report, 2018. URL <https://www.mordorintelligence.com/industry-reports/global-satellite-based-earth-observation-market-industry>. Last accessed 20 January 2020.
- [8] Euroconsult. Satellite-based earth observation, market prospects to 2027. Technical report, 2018. URL http://www.euroconsult-ec.com/17_October_2018. Last accessed 20 January 2020.
- [9] SpaceTec Partners. European earth observation and copernicus midstream market study. Technical report, 2013. URL https://www.copernicus.eu/sites/default/files/2018-10/Copernicus_Impact_on_Midstream_Sector.pdf. Last accessed 20 January 2020.
- [10] Satellite Imaging Corporation. Characterization of satellite remote sensing systems. Technical report, 2017. URL <https://www.satimagingcorp.com/services/resources/characterization-of-satellite-remote-sensing-systems/>. Last accessed 31 October 2019.
- [11] S. Pepper. Literature review for the primary mirror active optics. Delft University of Technology, 2018.
- [12] G. Denis, A. Claverie, X. Pasco, J. Darnis, B. de Maupeou, M. Lafaye, and E. Morel. Towards disruptions in Earth observation? New Earth Observation systems and markets evolution: Possible scenarios and impacts. *Acta Astronautica*, 137(May):415–433, 2017.
- [13] M. Born and E. Wolf. *Principles of Optics Electromagnetic Theory of Propagation, Interference and diffraction of Light*. Cambridge University Press, Cambridge, England, sixth edition, 1997.
- [14] G. P. van Marrewijk. Aberration correction system for a deployable space telescope. Master's thesis, Delft University of Technology, 2018.
- [15] D. Dolkens and H. Kuiper. Design and end-to-end modelling of a deployable telescope. In B. Cugny, N. Karafolas, and Z. Sodnik, editors, *International Conference on Space Optics — ICISO 2016*, volume 10562, pages 630 – 638, Biarritz, France, 2017. International Society for Optics and Photonics, SPIE.

- [16] D. Korsch. Anastigmatic three-mirror telescope. *Applied Optics*, 16(8):2074–2077, Aug 1977.
- [17] M. Corvers. Design of a primary mirror deployment mechanism for a deployable space telescope. Master's thesis, Delft University of Technology, 2018.
- [18] M. Voorn. Initiating the testing phase of a deployable space telescope: An experimental characterisation of hysteresis in core hinges. Master's thesis, Delft University of Technology, 2019.
- [19] H. Mallikarachchi and S. Pellegrino. Optimized designs of composite booms with integral tape-spring hinges. In *51st AIAA/ASME/ASCE/AHS/ASC Structures, Structural Dynamics, and Materials Conference*, pages 1 – 16. International Society for Optics and Photonics, ARC, 2010.
- [20] P. Halverson. Multi-stable compliant rolling-contact elements. Master's thesis, Brigham Young University, 2007.
- [21] V. Vasiliev and E. Morozov. *Mechanics and Analysis of Composite Materials*. Elsevier Science, 2001.
- [22] P. R. Yoder and D. Vukobratovich. *Opto-Mechanical Systems Design*. CRC Press, fourth edition, 2015.
- [23] M. Bougoin and J. Lavenac. From herschel to gaia: 3-meter class sic space optics. In J. H. Burge, O. W. Föhnle, and R. Williamson, editors, *Optical Manufacturing and Testing IX*, volume 8126, pages 248 – 257. International Society for Optics and Photonics, SPIE, 2011.
- [24] P. Y. Bely. *The Design and Construction of Large Optical Telescopes*. Springer, New York, New York, 2003.
- [25] J. A. Estefan. Survey of model-based systems engineering (MBSE) methodologies. Technical report, Space Systems/Loral, 2008. Revision: B.
- [26] I. Akkerhuis. Deployable space telescope: A literature review for the athermalisation of the secondary mirror. Delft University of Technology, 2019.
- [27] T. T. D. van Wees. Thermal modelling & analysis of the deployable space telescope. Master's thesis, Delft University of Technology, 2019.
- [28] D. Pidgeon and A. Tsao. Mass and power modeling of communication satellites. Technical report, INCOSE MBSE Focus Group, 1991. Prepared for NASA, Lewis Research Center.
- [29] J. Doenecke. Survey and evaluation of multilayer insulation heat transfer measurements. In *SAE Technical Paper*. SAE International, 07 1993.
- [30] J.-M. Ting, C. Tang, and P. Lake. Vapor grown carbon fiber reinforced aluminum matrix composites for enhanced thermal conductivity. In *SAE Technical Paper*, volume 551, page 281. Cambridge University Press, 1998.
- [31] D. Gilmore. *Spacecraft Thermal Control Handbook: Volume 1*. The Aerospace Press, E1 Segundo, California, second edition, 2002.
- [32] R. Karam. *Satellite thermal control for systems engineers*. American Institute of Aeronautics and Astronautics, Inc., Reston, Virginia, 1998.
- [33] M. Coesel and N. Pennings. Background for thermal modeling of multi layer insulation blankets. 1993.
- [34] S. R. Mirmira, M. C. Jackson, and L. S. Fletcher. Effective thermal conductivity and thermal contact conductance of graphite fiber composites. *Journal of Thermophysics and Heat Transfer*, 15(1):18–26, 2001.
- [35] M. A. Lambert, S. R. Mirmira, and L. S. Fletcher. Design graphs for thermal contact conductance of similar and dissimilar light alloys. *Journal of Thermophysics and Heat Transfer*, 20(4):809–816, 2006.

- [36] J. Kannel and K. Dufrane. Rolling element bearings in space. Technical report, NASA, 1986. Prepared for NASA by Battelle Columbus Labs.
- [37] R. Joven. Thermal properties of carbon fiber/epoxy composites with different fabric weaves. In *SAMPE International Symposium Proceedings*, 01 2012.
- [38] W. Adamczyk, S. Pawlak, and Z. Ostrowski. Determination of thermal conductivity of cfrp composite materials using unconventional laser flash technique. *Measurement*, 124:147 – 155, 2018.
- [39] Y. Gowayed and J.-C. Hwang. Thermal conductivity of composite materials made from plain weaves and 3-d weaves. *Composites Engineering*, 5(9):1177 – 1186, 1995.
- [40] M. W. Pilling, B. Yates, M. A. Black, and P. Tattersall. The thermal conductivity of carbon fibre-reinforced composites. *Journal of Materials Science*, 14:1326–1338, 1959.
- [41] R. Peyrou-Lauga. Optimized designs of composite booms with integral tape-spring hinges. In *47th International Conference on Environmental Systems*, 2017.
- [42] NASA. Ceres syn1deg product information, 2020. URL <https://ceres.larc.nasa.gov/products.php?product=SYN1deg>. Last accessed 13 April 2020.
- [43] K. Takenaka. Negative thermal expansion materials: technological key for control of thermal expansion. *Science and Technology of Advanced Materials*, 13(1):013001–013005, 2012.
- [44] J. Monroe, D. Gehring, I. Karaman, R. Arroyave, D. Brown, and B. Clausen. Tailored thermal expansion alloys. *Acta Materialia*, 102:333 – 341, 2016. ISSN 1359-6454.
- [45] Q. Wang, J. A. Jackson, Q. Ge, J. B. Hopkins, C. M. Spadaccini, and N. X. Fang. Lightweight mechanical metamaterials with tunable negative thermal expansion. *Phys. Rev. Lett.*, 117:175901, Oct 2016.
- [46] M. Bass, V. Mahajan, and E. Van Stryland. *Handbook of optics*. Number Volume 2 in Handbook of Optics. McGraw-Hill, third edition, 2001.
- [47] O. Selimoglu, M. Ekinici, and O. Karci. Thermal refocusing method for spaceborne high-resolution optical imagers. *Appl. Opt.*, 55(15):4109–4112, May 2016.
- [48] C. Miravet, D. Zorita, J. I. Bueno, L. Pascual, A. G. Marín, G. Taubmann, J. Azcona, J. M. Arroyo, I. Monasterio, U. García, J. Martín, C. Mas, J. Muñoz, A. Lopez, J. Eguía, S. Jarabo, R. García, R. Navarro, T. Belenguer, L. M. González, C. Pastor, D. Arrazola, C. G. Alvarado, I. Cabeza, A. Borges, A. Marini, and G. Crippa. Development status of the telescope for the Ingenio/SEOSAT mission primary payload. In *Optical Design and Engineering IV*, volume 8167, pages 311 – 319. International Society for Optics and Photonics, SPIE, 2011.
- [49] H. Demiryont, K. C. Shannon III, and J. Sheets. Emissivity modulating electrochromic device. In W. Fink, editor, *Space Exploration Technologies II*, volume 7331, pages 80 – 86. International Society for Optics and Photonics, SPIE, 2009.
- [50] H. Demiryont and D. Moorehead. Electrochromic emissivity modulator for spacecraft thermal management. *Solar Energy Materials and Solar Cells*, 93(12):2075 – 2078, 2009. IME-8.
- [51] P. Chandrasekhar, B. J. Zay, D. Lawrence, E. Caldwell, R. Sheth, R. Stephan, and J. Cornwell. Variable-emittance infrared electrochromic skins combining unique conducting polymers, ionic liquid electrolytes, microporous polymer membranes, and semiconductor/polymer coatings, for spacecraft thermal control. *Journal of Applied Polymer Science*, 131(19):1–15, 2014.
- [52] L. D. Grey. Control and alignment of the hubble space telescope. In L. D. Barr, editor, *Advanced Technology Optical Telescopes III*, volume 0628, pages 443 – 450. International Society for Optics and Photonics, SPIE, 1986.
- [53] J. Meseguer, I. Perez-Grande, and A. Sanz-Andres. *Spacecraft Thermal Control*. Woodhead Publishing, Cambridge, England, 2012.

- [54] W. J. Larson and J. R. Wertz. *Space Mission Analysis and Design*. Microcosm Press and Kluwer Academic Publishers, El Segundo, California, third edition edition, 2005.
- [55] Minco Products, Inc. Flexible heaters design guide, 2016. URL <https://www.minco.com/~media/files/minco/instructions/heaters/heater%20design%20guide.ashx>. Last accessed 28 May 2020.
- [56] N. Fatemi, H. Pollard, H. Hou, and P. Sharps. Solar array trades between very high-efficiency multi-junction and si space solar cells. In *Conference Record of the Twenty-Eighth IEEE Photovoltaic Specialists Conference - 2000 (Cat. No.00CH37036)*, pages 1083–1086, 2000.
- [57] Symétrie. Piezo hexapod with nanometer resolution. URL <https://symetrie.fr/en/hexapods/nanopos/>. Last accessed 01 June 2020.
- [58] Physik Instrumente (PI) GmbH & Co. KG. Parallel kinematics: Hexapod systems with 6 dof and nanometer resolution, 2018. URL https://4i4su48yalp4atxdbh9nq0of-wpengine.netdna-ssl.com/wp-content/uploads/2018/01/pi_hexapods_bro14e_r7.pdf. Last accessed 01 June 2020.
- [59] Physik Instrumente (PI) GmbH & Co. KG. P-841 preloaded piezo actuators, 2020. URL https://static.physikinstrumente.com/fileadmin/user_upload/physik_instrumente/files/datasheets/P-841-Datasheet.pdf. Last accessed 11 August 2020.
- [60] Physik Instrumente (PI) GmbH & Co. KG. High-resolution linear actuator suitable for vacuum, 2020. URL https://static.physikinstrumente.com/fileadmin/user_upload/physik_instrumente/files/datasheets/L-220-V-Datasheet.pdf. Last accessed 08 June 2020.
- [61] Micromotion GmbH. KeevoDrive® HighVac 10mm - Type 2, 2016. URL https://php.micromotion.de/produkt Datenbank/pdfcontainer/product_id25_englisch.pdf. Last accessed 08 June 2020.
- [62] Physik Instrumente (PI) GmbH & Co. KG. NEXLINE® OEM Linear Actuator. URL https://static.physikinstrumente.com/fileadmin/user_upload/physik_instrumente/files/datasheets/N-111-Datasheet.pdf. Last accessed 12 August 2020.
- [63] X. Zeshui and W. Cuiping. A consistency improving method in the analytic hierarchy process1research supported by nsf of china and shandong.1. *European Journal of Operational Research*, 116(2):443 – 449, 1999.
- [64] T. L. Saaty. How to make a decision: The analytic hierarchy process. *European Journal of Operational Research*, 48(1):9 – 26, 1990.
- [65] E. Favre, N. Wavre, P. Gay-Crosier, and M. Verain. European electric space rated motors handbook. In D. Danesy, editor, *8th European Space Mechanisms and Tribology Symposium*, volume 438 of *ESA Special Publication*, page 159, September 1999.
- [66] S. Murugesan. An overview of electric motors for space applications. *IEEE Transactions on Industrial Electronics and Control Instrumentation*, IECI-28(4):260–265, Nov 1981.
- [67] Phytron GmbH . LA linear actuator. for applications in ultra-high-vacuum and cryogenic environment, November 2018. URL https://www.phytron.eu/fileadmin/user_upload/produkte/motoren_aktuatoren/pdf/ds-la-en.pdf. Last accessed 10 August 2020.
- [68] Phytron GmbH . phySPACE™. stepper motor series for SPACE applications, standard and customised solutions, September 2019. URL https://www.phytron.eu/fileadmin/user_upload/produkte/motoren_aktuatoren/pdf/ds-physpace-en.pdf. Last accessed 10 August 2020.
- [69] Phytron GmbH . APS Technology, July 2017. URL https://www.phytron.eu/fileadmin/user_upload/produkte/endstufen_controller/pdf/ds-aps-en.pdf. Last accessed 12 August 2020.

- [70] M. Yoichi. Applications of piezoelectric actuator. pages 82–86. *Piezoelectric Devices*, December 2006.
- [71] Cedrat Technologies. Apa100m, March 2014. URL <https://www.cedrat-technologies.com/fileadmin/datasheets/APA100M.pdf>. Last accessed 12 August 2020.
- [72] Physik Instrumente (PI) GmbH & Co. KG. Electrical operation of piezo actuators, 2020. URL <https://www.piceramic.com/en/piezotechnology/propertiespiezoactuators/electricaloperation/>. Last accessed 11 August 2020.
- [73] Cedrat Technologies. Ccbu20, September 2018. URL <https://www.cedrat-technologies.com/fileadmin/datasheets/CCBu20.pdf>. Last accessed 12 August 2020.
- [74] A. Defendini, L. Vaillon, F. Trouve, T. Rouze, B. Sanctorum, G. Griseri, P. Spanoudakis, and M. von Alberti. Technology predevelopment for active control of vibration and very high accuracy pointing systems. In B. Schürmann, editor, *Spacecraft Guidance, Navigation and Control Systems*, volume 425 of *ESA Special Publication*, page 385, Feb 2000.
- [75] L. Vaillon, B. Sanctorum, J. Sperandei, A. Defendini, G. Griseri, M. Von Alberti, and P. Spanoudakis.
- [76] Cedrat Technologies. MECHATRONIC SOLUTIONS, February 2019. URL <https://cedrat-technologies.com/download/catalogue-02-2019.pdf>. Last accessed 26 August 2020.
- [77] Physik Instrumente. PiezoWalk Piezo Motors, 2020. URL <https://www.physikinstrumente.com/en/technology/piezoelectric-drives/piezowalk-piezo-motors/>. Last accessed 10 August 2020.
- [78] Physik Instrumente (PI) GmbH & Co. KG. NEXACT® linear actuator, manipulator, piezo stepper n-381, 2020. URL https://static.physikinstrumente.com/fileadmin/user_upload/physik_instrumente/files/datasheets/N-381-Datasheet.pdf. Last accessed 11 August 2020.
- [79] F. Claeysen, R. L. Letty, F. Barillot, and O. Sosnicki. Amplified piezoelectric actuators: Static & dynamic applications. *Ferroelectrics*, 351(1):3–14, 2007.
- [80] Texas Instruments. The engineer’s guide to temperature sensing, 2020. URL https://www.ti.com/lit/wp/slyy161/slyy161.pdf?ts=1596188793770&ref_url=https%253A%252F%252Fwww.google.com%252F. Last accessed 08 August 2020.
- [81] Kistler. Piezo vs. strain gauge, 2020. URL https://www.kistler.com/en/glossary/term/piezo-vs-strain-gauge/?gclid=CjwKCAjw1K75BRAEEiwAd41h1E-mFJyrYxUVtGyBoZhW-yrgqE2kMTWZql-JJ7_JKqkg4581joTi6xoCsW0QAvD_BwE. Last accessed 08 August 2020.
- [82] M. H. Song, Y. Zhang, Y. C. Li, G. Q. Chen, and Z. Y. Xiu. Analyzing hysteresis and thermal expansion coefficient of m40/az91d during thermal cycling. *Materials Science Forum*, 898:890–897, 2017.
- [83] H. C. Kim and F. L. Matthews. Hysteresis behaviour in CFRP. *Journal of Physics D: Applied Physics*, 6(15):1755–1761, oct 1973.
- [84] Micro Measurements . Strain gage selection: Criteria, procedures, recommendations, May 2018. URL <http://www.vishaypg.com/docs/11055/tn505.pdf>. Last accessed 06 August 2020.
- [85] B. Liptak. *Instrument Engineers’ Handbook, Volume One: Process Measurement and Analysis*. Instrument Engineers’ Handbook. CRC Press, fourth edition, 2003.
- [86] IST AG. Innovative sensor technology temperature sensors in deep space, September 2015. URL <https://www.ist-ag.com/en/news-events/news/innovative-sensor-technology-temperature-sensors-deep-space>. Last accessed 03 August 2020.

- [87] Draka Fileca S.A.S. . Wires & cables for space applications, 2020. URL <https://www.prysmiangroup.com/sites/default/files/atoms/files/Catalogue%20SPATIAL.pdf>. Last accessed 04 August 2020.
- [88] National Instruments Corporation. Strain gauge measurement – a tutorial, August 1998. URL http://elektron.pol.lublin.pl/elekp/ap_notes/NI_AN078_Strain_Gauge_Meas.pdf. Last accessed 07 August 2020.
- [89] OPTROMIX. FBG Sensors, 2020. URL <https://fibergratings.com/sensors.html>. Last accessed 08 August 2020.
- [90] M. Kreuzer. Strain measurement with fiber bragg grating sensors, for HBM, 2020. URL http://micronoptics.ru/uploads/library/documents/FBGS_StrainMeasurement_mo.pdf. Last accessed 08 August 2020.
- [91] E. Haddad, R. V. Kruzelecky, M. Mena, K. Tagziria, F. Ricci, I. McKenzie, N. Karafolas, and F. Hannoteau. Optical fiber sensors system on Proba-2 after 7 years. In B. Cugny, N. Karafolas, and Z. Sodnik, editors, *International Conference on Space Optics — ICSO 2016*, volume 10562, pages 1676 – 1684. International Society for Optics and Photonics, SPIE, 2017.
- [92] FBGS. FBG-Scan 80X, 2020. URL <https://fbgs.com/components/fbg-scan-80x/>. Last accessed 08 August 2020.
- [93] FBGS. All Grating Fibers (AGF[®]), 2020. URL <https://fbgs.com/components/all-grating-fibers-agf/>. Last accessed 08 August 2020.
- [94] OPTROMIX. FBG Sensors Strain, 2020. URL http://fibergratings.com/sensors_strain.html. Last accessed 08 August 2020.
- [95] E. Haddad, M. Mena, R. Kruzelecky, K. Tagziria, I. Mckenzie, and N. Karafolas. Monitoring the Propulsion System of PROBA-2 with Optical Fiber Sensors during 9 Years, March 2020.
- [96] R. Kruzelecky, J. Zou, N. Mohammed, E. Haddad, W. Jamroz, F. Ricci, J. Lamorie, E. Edwards, I. McKenzie, and P. Vuilleumier. Fiber-optic sensor demonstrator (fsd) for the monitoring of spacecraft subsystems on esa’s proba-2. In *ESA Special Publication*, volume 621 of *ESA Special Publication*, page 96, jun 2006.
- [97] Motion X Corporation. Distance measuring laser interferometer system components, 2019. URL <http://www.motionxcorp.com/pdf/MX-Laser-Interferometer-Manual.pdf>. Last accessed 21 August 2020.
- [98] attocube systems AG. Ids sensors, January 2018. Brochure.
- [99] B. Shortt, L. Mondin, P. McNamara, K. Dahl, S. Lecomte, and P. Duque. LISA laser system and European development strategy. In Z. Sodnik, N. Karafolas, and B. Cugny, editors, *International Conference on Space Optics — ICSO 2018*, volume 11180, pages 138 – 151. International Society for Optics and Photonics, SPIE, 2019.
- [100] P. Yoder. *Mounting Optics in Optical Instruments*. SPIE Press monograph. SPIE, 2008.
- [101] B. E. Catanzaro, D. Keane, S. J. Connell, D. Baiocchi, J. H. Burge, A. K. Maji, and M. K. Powers. UltraLITE glass/composite hybrid mirror. In J. B. Breckinridge and P. Jakobsen, editors, *UV, Optical, and IR Space Telescopes and Instruments*, volume 4013, pages 663 – 671. International Society for Optics and Photonics, SPIE, 2000.
- [102] W. T. Chen and C. W. Nelson. Thermal stress in bonded joints. *IBM Journal of Research and Development*, 23(2):179–188, 1979.
- [103] 3M. 3M[™] Scotch-Weld[™] Epoxy Adhesive EC-2216 B/A, June 2009. URL <https://multimedia.3m.com/mws/media/5941180/3m-scotch-weld-epoxy-adhesive-ec-2216-b-a.pdf>. Last accessed 15 August 2020.

- [104] L. C. Hale. *Principles and Techniques for Designing Precision Machines*. PhD thesis, Massachusetts Institute of Technology, 2013.
- [105] K. Qi, Y. Ding, Y. Xiang, C. Fang, and Y. Zhang. A novel 2-dof compound compliant parallel guiding mechanism. *Mechanism and Machine Theory*, 117:21 – 34, 2017.
- [106] P. Samara-Ratna, J. Sykes, C. Bicknell, J. Pye, N. C. Jessen, and H. U. Nøgaard-Nielsen. Space-compatible strain gauges as an integration aid for the james webb space telescope mid-infrared instrument. *The Journal of Strain Analysis for Engineering Design*, 50(2):92–102, 2015.
- [107] W. Callister. *Materials Science and Engineering: An Introduction*. Wiley, 1997.
- [108] NASA. Systems engineering technical reviews. Technical report, April 2009. URL https://nodis3.gsfc.nasa.gov/displayCA.cfm?Internal_ID=N_PR_7123_001A_&page_name=Chapter5#_Toc159347530. Last accessed 28 August 2020.
- [109] J. Kuiper, D. D. V. Villalba, E. Korhonen, S. P. S. Leegwater, J. A. M. Voorn, and D. Risselada. Dst engineering budgets document. Technical report, December 2018. Internal DST Document.
- [110] TE Connectivity. Sensors in space, June 2017. URL <https://www.te.com/content/dam/te-com/documents/sensors/global/sensors-in-space.pdf>. Last accessed 03 August 2020.